

UC Irvine

UC Irvine Electronic Theses and Dissertations

Title

Mid-Infrared Imaging through Nondegenerate Two-Photon Absorption

Permalink

<https://escholarship.org/uc/item/8j36w567>

Author

Knez, David

Publication Date

2024

Peer reviewed|Thesis/dissertation

UNIVERSITY OF CALIFORNIA,
IRVINE

Mid-Infrared Imaging through Nondegenerate Two-Photon Absorption

DISSERTATION

submitted in partial satisfaction of the requirements
for the degree of

DOCTOR OF PHILOSOPHY

in Chemistry

by

David Knez

Dissertation Committee:
Professor Eric O. Potma, Chair
Distinguished Professor V. Ara Apkarian
Adjunct Professor Dmitry A. Fishman

2024

Chapter 4© 2020 Nature Publishing Group
Chapter 5© 2021 Optica Publishing Group
Portions of Chapters 4 and 5 © 2021 American Institute of Physics
Chapter 6 © 2022 American Association for the Advancement of Science
All other materials © 2024 David Knez

DEDICATION

Dedicated to my family. Deborah, Linus, Stuart, Gabriella, Ethan, Laura, Audrey and Lance. Without them, this work means nothing.

TABLE OF CONTENTS

| | Page |
|---------------------------------------------------------------------------|-------------|
| LIST OF FIGURES | v |
| LIST OF TABLES | xi |
| ACKNOWLEDGMENTS | xii |
| VITA | xiii |
| ABSTRACT OF THE DISSERTATION | xvi |
| 1 Introduction | 1 |
| 1.1 Current state of mid-infrared imaging | 1 |
| 1.2 Nonlinear optical methods to improve mid-infrared imaging | 3 |
| 1.3 Scope of this dissertation | 6 |
| 2 Basic Principles of One- and Two- Photon Absorption | 8 |
| 2.1 Linear absorption | 9 |
| 2.1.1 Fermi's Golden Rule and molecular transitions | 9 |
| 2.1.2 Linear absorption coefficient | 12 |
| 2.1.3 Linear absorption in semiconductors | 13 |
| 2.2 Nonlinear absorption | 20 |
| 2.2.1 Quantum description of two-photon absorption | 20 |
| 2.2.2 Degenerate two-photon absorption coefficient | 23 |
| 2.2.3 Non-degenerate two-photon absorption | 24 |
| 2.2.4 Two-photon absorption in semiconductors | 26 |
| 2.2.5 Scaling rules for two-photon absorption in semiconductors | 28 |
| 3 Dispersion of the Two-Photon Absorption Coefficient in Silicon | 34 |
| 3.1 Introduction | 34 |
| 3.2 Theory | 36 |
| 3.2.1 Real density matrix approach | 36 |
| 3.2.2 Discrete states | 39 |
| 3.2.3 Continuum states | 46 |
| 3.2.4 Nonlinear absorption coefficients | 49 |
| 3.3 Experimental | 52 |

| | | |
|----------|-------------------------------------------------------------------------------------------|------------|
| 3.4 | Results and discussion | 58 |
| 4 | Mid-Infrared Imaging Through Nondegenerate Two-Photon Absorption | 68 |
| 4.1 | Introduction | 68 |
| 4.2 | Results | 70 |
| 4.2.1 | MIR detection with a Si photodiode | 70 |
| 4.2.2 | MIR spectroscopy with a single pixel Si detector | 72 |
| 4.2.3 | MIR imaging through on-chip NTA in a CCD camera | 73 |
| 4.2.4 | MIR videography of sample dynamics | 78 |
| 4.3 | NTA imaging with InGaAs | 80 |
| 4.3.1 | Two-Photon absorption coefficient of Si and InGaAs | 80 |
| 4.3.2 | Faster MIR imaging with InGaAs | 82 |
| 4.4 | Discussion | 86 |
| 4.5 | Materials and methods | 87 |
| 4.5.1 | FTIR experiments | 87 |
| 4.5.2 | Sample handling | 88 |
| 4.5.3 | Non-degenerate two-photon absorption with a Si photodiode | 88 |
| 4.5.4 | Imaging using a Si CCD camera | 89 |
| 4.5.5 | Imaging using an InGaAs camera | 90 |
| 5 | Three-Dimensional Mid-Infrared Imaging through Nondegenerate Two-Photon Absorption | 91 |
| 5.1 | Introduction | 91 |
| 5.2 | Concept and design | 93 |
| 5.3 | Results | 101 |
| 5.3.1 | 3D imaging through transparent and highly absorbing media | 103 |
| 5.3.2 | Chemically-sensitive tomographic imaging | 104 |
| 5.3.3 | Faster 3D imaging with InGaAs | 108 |
| 5.4 | Discussion | 109 |
| 5.5 | Methods | 111 |
| 5.5.1 | Fourier Transform Infrared Spectroscopy | 111 |
| 5.5.2 | MIR femtosecond NTA imaging system | 111 |
| 5.5.3 | Polymer structure fabrication | 112 |
| 5.5.4 | Confocal imaging of coin structure | 113 |
| 5.5.5 | Lysozyme crystals growing and handling | 113 |
| 6 | Spectral Imaging using Chirped Pulse Nondegenerate Two-Photon Absorption | 114 |
| 6.1 | Introduction | 114 |
| 6.2 | Concept and design | 115 |
| 6.3 | Results | 123 |
| 6.4 | Discussion | 133 |
| 6.5 | Materials and methods | 135 |
| | BIBLIOGRAPHY | 138 |

LIST OF FIGURES

| | Page | |
|-----|---------------------------------------------------------------------------------------------------------------------------------------------------------------------------------------------------------------------------------------------------------------------------------------------------------------------------------------------------------------------------------------------------------------------------------------------------------------------------------------------------------------------------------------------------------------------------|----|
| 2.1 | Dispersion diagram of parabolic valence and conduction bands in semiconductors. The linear absorption process is indicated by the orange arrows for a given point in \mathbf{k} -space, symbolizing a vertical transition. | 15 |
| 2.2 | Intensity loss as a function of propagation distance due to absorption. Linear absorption (1PA, yellow line) was calculated for $\alpha = 0.05 \mu\text{m}^{-1}$ and two-photon absorption (TPA, red line) was calculated with an α_2 -coefficient that was scaled such that the two curves intersect at the 50% loss point. Because the TPA process depends nonlinearly on the incident intensity, it shows a steeper depth-dependence at shorter distances and a shallower depth-dependence at longer distances relative to the linear absorption curve. | 24 |
| 2.3 | Two Jablonski diagrams depicting the two permutations of the NTA process for system with two (real) states a and b , denoted by the solid black lines. The virtual intermediate state n is indicated by the dotted line. In this example, $\omega_1 > \omega_2$. In the case of extreme NTA, ω_1 approaches ω_{ba} and ω_2 approaches zero, giving rise to an increase of the NTA coefficient. | 26 |
| 2.4 | Two-photon absorption in the two-band model, described in terms of a fundamental interband transition (orange arrow), mediated by \mathbf{p}_{cv} , and an intraband transition (red arrow), mediated by \mathbf{p}_{cc} or \mathbf{p}_{vv} . Both frequency permutations are shown. | 30 |
| 2.5 | Scaling of the linear absorption coefficient (blue) with the normalized photon energy and the derived degenerate two-photon absorption coefficient (orange). 31 | 31 |
| 2.6 | Plot of scaling function $F_{\text{NTA}}^{\text{tot}}$ defined through photoelectron generation in Eq. 2.63. | 33 |
| 3.1 | Schematic of non-collinear pump probe experiment. | 53 |
| 3.2 | Exemplary pump probe data and corresponding nonlinear transmittance fit. The photon energies used here are 0.91 eV and 0.376 eV. | 57 |
| 3.3 | Scaling behavior of the two photon absorption coefficient α_2 as a function of normalized photon energy while both photons are below the gap. | 59 |
| 3.4 | Scaling of the degenerate two-photon absorption coefficient α_2 as a function of $x = \hbar\omega/E_g$. Squares are obtained from Ref [77] and thick solid line results from the RDMA analysis of two-photon absorption. | 61 |

| | | |
|-----|---------------------------------------------------------------------------------------------------------------------------------------------------------------------------------------------------------------------------------------------------------------------------------------------------------------------------------------------------------------------------------------------------------------------------------------------------------------------------------------------------------------------------------------------------|----|
| 3.5 | Scaling of the non-degenerate two-photon absorption coefficient α_2 as a function of the normalized equivalent energy. Experimental data points are obtained from Ref [67] and thick solid lines represent the results from the RDMA analysis. Different colors correspond to different non-degeneracy energy ratios $\hbar\omega_a/\hbar\omega_b$ | 63 |
| 3.6 | Scaling of the non-degenerate two-photon absorption coefficient α_2 as a function of the normalized equivalent energy. Data points indicate experimental results and thick solid lines represent the results from the RDMA analysis. Different colors correspond to different non-degeneracy energy ratios $\hbar\omega_a/\hbar\omega_b$ | 65 |
| 4.1 | Linear absorption (blue) as a function of the pulse energy at 1030 nm, non-degenerate two-photon absorption (orange) as a function of the NIR gate pulse energy at 1480 nm and degenerate two-photon absorption (purple) as a function of the gate pulse energy at 1480 nm. For the non-degenerate curve, the MIR pulse energy at 3388 nm was set to 0.65 nJ. Inset: proposed scheme of photon absorption in Si. | 71 |
| 4.2 | Full dynamic range for MIR detection with a detection floor of 200 fJ picosecond pulse energy for given detector parameters. 1 V on the y-axis corresponds to $8.2 * 10^4$ photoelectrons generated per pulse. | 72 |
| 4.3 | Absorption spectrum of dimethyl sulfoxide (DMSO) using non-degenerate two photon detection for measuring the transmitted MIR radiation. Results are in excellent agreement with spectrum measured obtained with conventional ATR-FTIR of bulk DMSO. | 73 |
| 4.4 | Schematic of wide-field MIR imaging system based on non-degenerate two-photon absorption in a Si-based CCD camera. | 74 |
| 4.5 | (a) Image of MIR (3394 nm) beam profile using a 1478nm NIR gate pulse. (b) Image of razor blade covering half of MIR. The cross section is shown in the top of the panel. Error function analysis shows that the resolution is about 15 pixels ($\sim 100 \mu\text{m}$) under the current conditions. | 75 |
| 4.6 | Spectral imaging of a $150 \mu\text{m}$ thick cellulose acetate film. The printed letters serve as a mask that blocks broadband radiation. (a) FTIR transmission spectrum. MIR image taken at (b) an off-resonance energy, (c) the high energy side of the absorption maximum and (d) the absorption maximum. | 76 |
| 4.7 | MIR images of various materials accompanied with corresponding FTIR spectra. The left column shows non-resonant MIR images, whereas the middle column shows MIR images take at an energy that corresponds with a designated absorptive line. The right column displays the FTIR absorption spectra of the sample with on (orange) and off (grey) resonances indicated. (a) interface between D_2O and silicone lubricant. (b) APPPO polymer film. (c) Wing of a common bee. The exposure time for all images is 1 second. | 78 |
| 4.8 | Timelapse of printed cellulose acetate film. Each panel is a frame taken from a live recording at different time points. Top: MIR beam off resonance to C-H absorption (3078 cm^{-1}). Bottom: MIR beam on resonance with C-H stretch (2949 cm^{-1}). The printed characters running are no longer visible due to loss of MIR transmission. | 79 |

| | | |
|------|------------------------------------------------------------------------------------------------------------------------------------------------------------------------------------------------------------------------------------------------------------------------------------------------------------------------------------------------------------------------------------------------------------------------------------------------------------------------------------------------------------------------------------------------|-----|
| 4.9 | Timelapse of a live nematode (<i>C. elegans</i>) in D ₂ O buffer. Each panel is a frame taken from a live recording at different time points. MIR beam was tuned to 2950 cm ⁻¹ , on resonance with the C-H stretching vibrations of protein. | 80 |
| 4.10 | Scaling rule of the degenerate two-photon absorption coefficient as a function of semiconductor bandgap. Data for InSb from [86], InGaAs from [87], GaAs and ZnSe from [82], and CdTe, ZnO, ZnS from [56]. | 81 |
| 4.11 | (a) 4250 nm (~ 2350 cm ⁻¹) single shot detection by an InGaAs camera using 60 μ s exposure time. The MIR average power is 130 μ W. The inset shows the spatial cross section of the beam profile on the camera chip (orange curve) when both MIR and gate pulses are present. The light blue curve shows the DTA background when only the 1900 nm gate beam is present. (b) 3840 nm (~ 2600 cm ⁻¹) pulse train detection on a Si CCD camera using 100 ms exposure time. The average power is 1 mW. | 83 |
| 4.12 | Chemically selective 2D imaging of cellulose acetate film. A figure is printed on the film with black ink to generate contrast. If tuned to the C-H stretching mode, cellulose acetate becomes less transparent, decreasing the contrast between the clear and inked areas of the film. Exposure time: 1 ms. | 84 |
| 4.13 | Chemically selective 2D imaging of cellulose acetate film. A figure is printed on the film with black ink to generate contrast. If tuned to the C-H stretching mode, cellulose acetate becomes less transparent, decreasing the contrast between the clear and inked areas of the film. Exposure time: 1 ms. | 85 |
| 5.1 | (a) Schematic representation of experimental setup. (b) Beam image on CCD Si chip with MIR (2850 cm ⁻¹ , 3500 nm) and gate NIR pulse (8333 cm ⁻¹ , 1200 nm). The inset shows a gate pulse image through DTA. (c) Spatial cross section of the beam image on CCD Si chip with (NTA, orange) and without MIR pulse (DTA, blue line). Inset: temporal cross-correlation of MIR and gate pulse, indicating a 110 fs pulse width (gray line is Gaussian fit) | 98 |
| 5.2 | Spectral response of detection system to MIR pulse reflected off a gold mirror (orange dots represent average counts within the center of gaussian beam, blue dots represent constant DTA background of the NIR beam). Average power flux is 4 mW/cm ² prior to the camera and the exposure time is 100 ms for all measurements. Horizontal lines represent the estimated Fourier limited spectral bandwidth of the 110 fs MIR pulse. | 99 |
| 5.3 | 3D imaging of cellulose acetate transparency ladder at 2600 cm ⁻¹ shown at different perspective angles (a) and (b). Though reflected from the same surface 2, photons propagating through cellulose acetate sheet 1 are temporally delayed (2') with respect to photons that travel in air (2). (c) Spatial cross-section of MIR pulse propagation in layered cellulose acetate structure. (d) Gauss fit for response on 2' interface (propagation through cellulose acetate). FWHM indicates spatial resolution of 12.6 μ m. | 100 |

| | | |
|------|--------------------------------------------------------------------------------------------------------------------------------------------------------------------------------------------------------------------------------------------------------------------------------------------------------------------------------------------------------------------------------------------------------------------------------------------------------------------------------------------------------------------------------------------------------------------------------------------------------------------------------------------------------------------|-----|
| 5.4 | (a-c) Tomographic imaging of the structured metal surface of a one cent US Coin (Union Shield). (a) 3D reconstruction; (b) and (c) frames measured at height $h = 30 \mu\text{m}$ and $h = 0 \mu\text{m}$, respectively. (d)-(f) Tomographic imaging of stacked cellulose acetate sheets, a weakly reflection polymer structure. (d) 3D reconstruction; (e) and (f) 3D frames take at the top of each sheet ($\Delta h = 105 \mu\text{m}$). Total 3D scan time is 1 second. | 102 |
| 5.5 | (a, b, c) Tomographic imaging of the structured metal surface of a one cent US coin (Union Shield). (a) 3D reconstruction, (b) and (c) are frames measured at height $h = 30 \mu\text{m}$ and $h = 0 \mu\text{m}$, respectively. (d) 3D reconstruction of confocal reflection imaging of the coin. (e) and (f) are 2D confocal scans measured at height difference $30 \mu\text{m}$ | 102 |
| 5.6 | Sketch of penetration experiment arrangement through (a) 3 mm thick GaAs wafer and (d) 190 μm water layer. (b) 3D reconstruction of one cent US coin (Union Shield) through 3 mm GaAs wafer. (c) Tomographic imaging of stacked cellulose acetate sheets through 3 mm GaAs wafer. Imaging of one cent US coin (Union Shield) through 190 μm water layer (380 μm in double pass) at (e) 2850 cm^{-1} and (f) 2600 cm^{-1} | 103 |
| 5.7 | 3D imaging of stacked cellulose acetate sheets with printed letters. (a) 3D reconstruction of the structure. (b) FTIR transmission spectrum of cellulose acetate (blue line) and real part of the refractive index obtained through a Kramers-Kronig transformation (orange dotted line). Rectangles represent Gaussian pulse width of 150 cm^{-1} . (c) and (d) 3D imaging at 2875 cm^{-1} ; (e) and (f) 3D imaging at 2600 cm^{-1} . Total image acquisition time is 1 second. | 105 |
| 5.8 | 3D image of cellulose acetate structure imaged at 2600 cm^{-1} and 2850 cm^{-1} from a top view perspective. (c) Peak positions of reflections off the different interfaces. The difference between the peak positions found for propagation in air and polymer reveals that $n \sim 1.5$ for 2600 cm^{-1} and $n \sim 1.87$ for 2850 cm^{-1} | 106 |
| 5.9 | 3D imaging of a resin structure manufactured through projection-based photolithography. (a) 3D reconstruction of resin structure. (b) FTIR absorption spectrum of the resin (blue line) and real part of the refractive index obtained through a Kramers-Kronig transformation (orange dotted line). Rectangles represent Gaussian pulse width of 150 cm^{-1} . (c) and (d) 3D imaging at 2775 cm^{-1} ; (e) and (f) 3D imaging at 2450 cm^{-1} . Structure height is 50 μm . Images have been corrected for non-spectroscopic NTA efficiency variations (see Figure 5.2). Total image acquisition time is 1 second. | 107 |
| 5.10 | Imaging of different lysozyme crystals on mica glass. (a) 3D reconstruction of lysozyme crystal cluster at 2875 cm^{-1} , (d) 2600 cm^{-1} , and (f) 2450 cm^{-1} . Images have been corrected for non-spectroscopic NTA efficiency variations. FTIR absorption spectrum of lysozyme is shown on far right. | 108 |
| 5.11 | FIG. 5. Tomographic images of the US penny (a) and dime (b) scanned at 4250 nm (2350 cm^{-1}). The total acquisition time for each volumetric scan is 20 ms. | 109 |

| | | |
|-----|--------------------------------------------------------------------------------------------------------------------------------------------------------------------------------------------------------------------------------------------------------------------------------------------------------------------------------------------------------------------------------------------------------------------------------------------------------------------------------------------------------------------------------------------------|-----|
| 6.1 | Left: 40 fs MIR pulse before and after dispersion by 15 cm of Si. Right: 40 fs MIR pulse broadened using both GVD and TOD and its corresponding instantaneous frequency. Pulse broadened only by GVD is shown as a reference. | 119 |
| 6.2 | Visualized concept of chirped pulse–NTA (CP-NTA). The broad pulse spectrum is modified because of linear absorption of light by the sample (a and c). Inset shows a time-frequency plot of the MIR pulse in the absence or presence of linear chirp. (b and d) The resulting pulse shape in the time domain without (b) and with (d) introduction pulse chirp. Dark blue lines illustrate the convolution between the MIR and gate pulses. | 120 |
| 6.3 | Schematic of experimental setup. An ultrashort MIR pulse is chirped by propagation through a 15-cm Si rod and spatially overlapped with a temporally short gate pulse on the camera chip. Control of the MIR-gate pulse time delay permits a rapid spectral scan across the MIR pulse spectrum. | 122 |
| 6.4 | Average spectral irradiance and spectral energy per camera pixel of chirped MIR pulse. | 123 |
| 6.5 | Demonstration of MIR spectroscopy using CP-NTA. Side-by-side demonstration of spectroscopy on polymer standard (7 μm thick polystyrene) in the frequency domain (spectrometer, left, A and C) and time domain (CP-NTA, right, B and D). (E and F) Retrieved absorption spectra are in good agreement with the polystyrene absorption lines. OD, optical density. | 125 |
| 6.6 | Gaussian fit of measured CP-NTA spectrum of polystyrene. The absorption lines at 2923 cm^{-1} (original FWHM= 35 cm^{-1}) and at 3025 cm^{-1} (original FWHM= 15 cm^{-1}) convolved with a Gaussian resolution function with width of 8.4 cm^{-1} results in 38 cm^{-1} and 19 cm^{-1} , respectively. | 126 |
| 6.7 | Linear chirp study. Absorption spectrum of polystyrene measured through imaging CP-NTA using pulses of different central frequency. Line positions and separations of absorption features remain identical regardless of the features being at the center or at the wing of the pulse time profile. The resulting distribution indicates a linear distribution of frequency components across the full time profile of the pulse. | 128 |
| 6.8 | unprocessed spectral imaging of polymer samples. (a) Polymer absorption spectrum extracted from the hyperspectral data cube. (b to e) Raw transmission images at different positions in time/spectral domain, directly revealing spatially dependent chemical information in the field of view. Acquisition time is 16 ms per frame/spectral point. | 130 |
| 6.9 | False color visualization of spectral imaging. Spectral imaging fo PMMA/polystyrene films. (a and c) Spectra of polystyrene and PMMA components obtained by CP-NTA and FTIR. Red and green lines denote spectral position of color channel image. Dimensionality of the hyperspectral data stack is reduced through overlay of red and green color channels measured on and off the absorption resonance of a given polymer. (b and d) resulting false color spectral image. Effective image acquisition time is 32 ms (16 ms per frame. | 132 |

6.10 Spectral images of chemical matrices. Spectral imaging of various materials and material combinations: (a) polystyrene, (b and f) PMMA/polystyrene hybrids, (c) ethanol, (d) polyethylene, and (e) silicone lubricant (polydimethylsiloxane). Effective image acquisition time is 32 ms (16 ms per frame). . . . 133

LIST OF TABLES

| | Page |
|-----------------------------------------------------------------------------------|------|
| 3.1 Experimentally obtained values for α_2 in cm/GW | 57 |
| 3.2 Band parameter values for Si | 66 |
| 3.3 Anisotropy parameters for Si, excitonic energies calculated from Eq. (3.19) . | 67 |
| 3.4 Thermal electron and hole lengths for Si | 67 |
| 4.1 Parameters for comparison of Si and InGaAs in Fig. 4.11. | 82 |
| 4.2 Si photodiode experiment specifications. | 89 |
| 4.3 Si CCD experiment specifications. | 89 |

ACKNOWLEDGMENTS

I must acknowledge National Institutes of Health (Grant No. R01-GM132506), National Science Foundation (CMMI 1151191, GRFP, DMR-2002837), National Institutes of Health (Grant No. GM R21-GM141774), and the Air Force STTR AFX20C-TCS01/AFWERX Program (Contract No. F4FBEQ1019A0DP) for supporting this work. I'd like to thank them and the University of California, Irvine for supporting this research. I must also acknowledge previous publication of my work. Chapter 4 of this dissertation is a reprint of the material as it appears in [1], used with permission from Nature Publishing Group. The co-authors listed in this publication are Adam M. Hanninen, Richard C. Prince, Eric O. Potma, and Dmitry A Fishman. Portions of Chapter 4 and 5 of this dissertation are reprints of the material as it appears in [2], used with permission from American Institute of Physics. The co-authors listed in this publication are Martin H. Ettenberg, Hai Nguyen, Eric O. Potma, and Dmitry A Fishman. Chapter 5 of this dissertation is a reprint of the material as it appears in [3], used with permission from Optica Publishing Group. The co-authors listed in this publication are Eric O. Potma, Yong Chen, Yulia Davydova, Amanda Durkin, Mihaela Balu, Brenna Norton-Baker, Rachel W. Martin, Tommaso Baldacchini and Dmitry A Fishman. Chapter 6 of this dissertation is a reprint of the material as it appears in [4], used with permission from American Association for the Advancement of Science. The co-authors listed in this publication are Benjamin W. Toulson, Anabel Chen, Martin H. Ettenberg, Hai Nguyen, Eric O. Potma, and Dmitry A Fishman.

Fine print aside, I'd like to first truly thank my advisor, Professor Eric Potma. His countless hours of patience and counsel are how I was able to come as far as I have. I would also like to thank Adjunct Professor Dmitry Fishman, who came to me with the initial experiments that have since produced multiple high impact papers. His hands-on experience and mentoring were just as instrumental in my success.

Next on the list is everyone I've had the pleasure of working with over the years. From the Potma, Fishman, and Murray labs, thank you Dr. Shamsul Abedin, Dr. Sifat Abid, Zac Cornwell, Evan Garcia, Salile Khandani, Yong Li, Marcus Marracci, Jovany Merham and Johanna Rinaman. Thank you for always being open for a good discussion, whether it was scientific or something else entirely.

VITA

David Knez

EDUCATION

Doctor of Philosophy in Chemistry

University of California, Irvine

2024

Irvine, California

Master of Science in Chemistry

University of California, Irvine

2022

Irvine, California

Bachelor of Science in Chemistry

The Ohio State University

2018

Columbus, Ohio

RESEARCH EXPERIENCE

Graduate Research Assistant

University of California, Irvine

2018–2023

Irvine, California

TEACHING EXPERIENCE

Graduate Teaching Assistant

University of California, Irvine

2018–2021

Irvine, California

REFEREED JOURNAL PUBLICATIONS

- D. Knez, A.M. Hanninen, R.C. Prince, E.O. Potma, and D.A. Fishman, Infrared chemical imaging through non-degenerate two-photon absorption in silicon-based cameras
Light Sci Appl 9, 125 (2020) 2020
- E.O. Potma, D. Knez, Y. Chen et al., Rapid chemically selective 3D imaging in the mid-infrared
Optica 8, 995-1002 (2021) 2021
- E.O. Potma, D.Knez, M.H. Ettenberg, M. Wizeman, H. Nguyen, T. Sudol, D.A. Fishman, High-speed 2D and 3D mid-IR imaging with an InGaAs camera
APL Photonics 1 September 2021; 6 (9): 096108 2021
- D. Knez, B.W. Toulson, A. Chen, M.H. Ettenberg, H. Nguyen, E.O. Potma, D. A. Fishman, Spectral imaging at high-definition and high speed in the mid-infrared
Sci. Adv. 8, eade4247(2022) 2022
- D. Ziemkiewicz, D. Knez, S. Zielińska-Raczyńska, G. Czajkowski, E. Garcia, E.O. Potma, D. A. Fishman, Real Density Matrix Approach for Two-Photon Absorption in Silicon
Submitted 2024
- Y. Y. Luna Palacios, S. Khandani, E. Garcia, A. Chen, S. Wang, K. Roy, D. Knez, D. A. Kim, I. Rocha-Mendoza, E.O. Potma, Spectroscopic analysis of the sum-frequency response of the carbon-hydrogen stretching modes in collagen type I
Submitted 2024

REFEREED CONFERENCE PUBLICATIONS

- Coherent Nonlinear Optical Microscopy with Mid-infrared Radiation
Applied Physical Society March Meeting 2020
- Infrared chemical imaging with a silicon-based camera using non-degenerate two photon absorption
Photonics West 2020

| | |
|----------------------------------------------------------------------------------------------------------|-------------|
| Nonlinear optics improves mid-infrared vibrational imaging | 2021 |
| Photonics West | |
| High speed, high definition mid-infrared spectral imaging by non-degenerate two-photon absorption | 2023 |
| Photonics West | |

ABSTRACT OF THE DISSERTATION

Mid-Infrared Imaging through Nondegenerate Two-Photon Absorption

By

David Knez

Doctor of Philosophy in Chemistry

University of California, Irvine, 2024

Professor Eric O. Potma, Chair

The mid-infrared (MIR) part of the electromagnetic spectrum corresponds to an energy range that includes the resonances of molecular bond vibrations. For this reason, MIR light is extensively used to characterize samples, as the absorption of particular MIR frequencies results in a spectrum corresponding to the mode vibrations of chemical motifs. The ability to exploit this in the context of imaging would allow both the morphological character and chemical composition of samples to be visualized simultaneously.

Unfortunately, MIR imaging technologies still struggle to gain widespread adoption as analytical tools, as they fail to provide high-definition images quickly over the whole MIR spectrum. The work contained in this thesis seeks to overcome this hurdle by transferring the information carried by the MIR radiation to the visible-to-near-infrared part of the electromagnetic spectrum. In the latter spectral range, camera technologies are fast, sensitive and ever increasing in definition. Although the linear spectral responsivity of such cameras excludes the direct detection of MIR radiation, a nonlinear absorption process can be used to convert MIR light to charge carriers in the camera's light sensitive element. In this approach, two pulses of different energy, one in the MIR and one in the near infrared (NIR) are timed to simultaneously reach the detector, enabling the excitation of charge carriers through nondegenerate two-photon absorption (NTA). The use of NTA effectively turns a

visible/NIR camera into a MIR imager. This thesis explores this principle to generate MIR images of a variety of samples, where the image contrast is provided by the spectroscopic fingerprints of molecular vibrations.

The work in this thesis includes the first demonstration of the NTA principle for the purpose of widefield MIR imaging, followed by specific implementations that leverage the physical properties of ultrashort laser pulses to provide 3D imaging as well as hyperspectral imaging capabilities. In addition, this work discusses a rigorous theory of NTA in indirect semiconductors such as silicon. Together, the work presented herein provides a comprehensive picture of the physics and applications of the NTA process for rapid MIR imaging of a broad range of sample targets.

Chapter 1

Introduction

1.1 Current state of mid-infrared imaging

Imaging using mid-infrared (MIR) light offers the unique opportunity to visualize samples according to their chemical composition in addition to their morphological character. The ability to discriminate objects in this fashion is of practical use in a variety of imaging and sensing applications. These include histopathology [5], standoff detection of materials [6–9], gas analysis [10], and environmental surveying [11]. These use cases are however generally limited to static object analysis, with conventional imaging speeds too slow to realize hyperspectral imaging in real time [12]. The ability to rapidly produce spectrally resolved images that adequately sample the spatial character of the object under study is greatly desired, but is currently met with issues on both the generation and detection sides.

An ideal MIR source for spectroscopic purposes is one that exhibits sufficient brightness and broadband character over the entire MIR spectral region. Traditionally, broadband light sources in the MIR are based on the thermal emission of an electrically heated material, such as a global or Nernst lamp. The spectral radiance of these sources generally follows

that of a blackbody radiator, which favors emission in the NIR and less so in the MIR. While such sources have been used to great success in Fourier transform infrared (FTIR) spectroscopy, the reconstruction of the MIR absorption spectrum through an interferometric scan and postprocessing can be slow when used for imaging. The development of high brightness light sources in the MIR designed to overcome the limitations of blackbody radiators is relatively new, with end-user quantum cascade lasers (QCL)s debuting in the 21st century. QCL technology, however, cannot yet support the broadband emission necessary for MIR spectroscopy [13], instead the sweeping of multiple tunable narrowband QCL sources is required to cover the MIR spectral range [14]. Super-continuum (SC) sources appear to be an attractive solution, with designs coming ever closer to achieving a high intensity output that is uniformly distributed over the full MIR range. Current SC sources already provide spectral radiances well above those of thermal emitters, but below what is possible with QCLs [15]. Unfortunately, the technology is still young and suffers from a noisy output spectrum with a limited bandwidth. For instance, commercial SC sources feature a spectral range that extends from approximately $1\ \mu\text{m}$ to $4\ \mu\text{m}$, which is less than the $3\text{--}20\ \mu\text{m}$ range used in MIR spectroscopy. Genuinely broad and bright MIR super-continuum sources have been experimentally demonstrated, but are still the subject of academic study [16–19]. Moreover, SC platforms are typically ultrafast sources, which may be unsuitable for use by non-experts [20, 21].

Detection of MIR light, on the other hand, is mature in technological development but hampered by its fundamental physics. The detectors in use are typically fabricated out of a low bandgap semiconductor material such as InSb or mercury cadmium telluride (MCT) for broadband MIR detection. The energy of the band gap is sufficiently small such that thermal excitation is inevitable at room temperature, giving rise to a large source of noise in detection. Cryogenic cooling is often used to eliminate the thermal noise, drastically increasing the size and cost of common MIR detectors or arrays. Image formation is achieved either by raster scanning a sample with a single element photodetector or in wide-field fashion with

an array detector. Pixel dwell times in raster scanning can be on the order of microseconds using QCL sources, but image construction requires obtaining thousands or millions of pixels individually over several discrete wavelengths to obtain both spectral and spatial information. Array sensors that are relatively small, usually comprised of 128×128 or 256×256 pixels, can have fast readout times to obtain spatial information quickly, but higher definition images then require mosaicking of smaller frames into a larger sized image.

MIR imaging instrumentation has reached somewhat of an impasse. MIR illumination continues to develop, but as of yet cannot overcome the limitation of current MIR detection strategies. This is in contrast to detection approaches in the visible or NIR range of the spectrum, where imagers are fast, sensitive, and have definitions well beyond 1000×1000 pixels, extending into the megapixel (Mpx) range, allowing rapid image acquisition at high definition. Therefore, nonlinear optical (NLO) techniques that enable the transfer of information carried by MIR light into the visible range of the spectrum are highly attractive, as they are compatible with mature visible/NIR detector technology, thus bypassing the limitations of MIR detectors.

1.2 Nonlinear optical methods to improve mid-infrared imaging

The suite of NLO methods for converting MIR radiation into a signal registered by a visible/NIR detector involves some conversion step. A common conversion approach makes use of a NLO crystal, which is employed to upconvert the MIR-encoded information into the visible/NIR through a parametric process [22]. The generated visible/NIR light is then detected by a sensitive detector in the visible/NIR range [23, 24]. Crystal upconversion can be quite efficient, offering a sensitive and rapid mechanism for (indirect) MIR signal detection [25–

27]. Yet, this approach is not a natural match for widefield detection. Not only do nonlinear materials have their own limited transparency windows that limit the range of MIR frequencies that can be converted, the upconversion process is subject to phase-matching, which complicates alignment and further constrains the addressable spectral range. To cover a broad MIR bandwidth, phase-matching requires the tuning of either the crystal temperature or orientation, thus complicating its practical implementation [28]. In addition, for wide-field imaging, different phase matching settings are required during acquisition, necessitating several post processing steps for image reconstruction [29].

A unique form of indirect MIR detection using a crystal are the nonlinear interferometers with entangled sources [30, 31]. These techniques involve creating an “induced coherence” between two parametrically created signal beams [32, 33]. First, a non-degenerate signal-idler pair is generated by a $\chi^{(2)}$ process in a NLO crystal where the idler in the MIR interacts with the sample, changing the spatial distribution of its amplitude and phase. This MIR idler beam is then used to generate another signal beam that is used to interfere with the original signal. The detection of the interference pattern then retrieves the information encoded in the MIR. As the fluences of the light must be kept extremely low to maintain quantum coherence, these techniques are useful for nondestructive MIR imaging of light-sensitive samples [34–36]. However, these low light conditions necessitate long acquisition times, and interferometric approaches require precise stabilization of participating beam phases, making the experimental setups very delicate.

Another set of methods involve using the optical properties of the sample under study, eliminating the need of an external crystal altogether. Photothermal spectroscopy is a rapidly developing MIR pump-probe technique in chemically-sensitive microspectroscopy applications [37, 38]. As the name suggests, a MIR beam is absorbed by the sample, where it is dissipated as heat, in turn, modifying its refractive index [39]. This transient perturbation of the local refractive index is experienced as a deflection by a co-located visible probe beam.

While photothermal techniques have seen excellent success in microscopy applications [40–43], they are generally not robust enough to accommodate thick samples or those that are opaque to the visible probe.

In addition, leveraging the nonlinear optical response of samples can enable second or third order interactions to upconvert incident MIR radiation, termed sum frequency generation (SFG) [44] and third-order sum frequency generation (TSFG), respectively [45]. Here, two beams, one in the MIR and one in the NIR or visible are combined in the sample for upconversion. When the MIR beam is resonant with the sample, the process is promoted over a nonresonant background and is detected as a gain of photons at the sum frequency [46]. As SFG is a second order nonlinear optical process, the choice of samples for study is limited to interfaces or bulk materials that lack inversion symmetry [47–49]. TSFG has been developed to circumvent this by using a third order interaction, allowing the sum frequency signal to be generated from bulk materials [50, 51]. However, the optical fluences required to produce such a signal constrain their use to microscopy applications, and require samples yield enough signal before simply burning.

An alternative NLO approach for providing fast, high-definition imaging in the MIR is developed here for the first time. Using non-degenerate two-photon absorption (NTA), MIR spectroscopy and imaging can be accomplished with wide bandgap semiconducting materials designed for visible or NIR detection. Here, the upconverting step is achieved directly in the camera using the NLO properties of its light sensitive layer. Similar to up-conversion methods, the NTA technique takes advantage of the more the advanced visible/NIR camera technologies, but without the aforementioned difficulties of associated with up-conversion in crystals or samples. In NTA, the MIR signal beam (ω_{MIR}) is combined with another beam in the NIR (ω_{NIR}) at the detector plane to jointly excite charge carriers through the process of two-photon absorption. The absorption event does not require phase matching and can theoretically support imaging over the entirety of the MIR, provided that the combined

photon energy $\hbar(\omega_{\text{MIR}} + \omega_{\text{NIR}})$ is equal to or more than the bandgap energy of the detector material. As the nonlinear interaction happens in the detector, only the MIR interacts with the sample to acquire chemically-sensitive information, reducing the light dosage the sample receives and can be used with materials that normally do not transmit visible beams.

1.3 Scope of this dissertation

The content of this thesis is as follows. The mathematical and physical preliminaries distinguishing one- and two-photon absorption are described for both molecular and direct gap semiconducting systems in Chapter 2. In Chapter 3, a collaborative effort between the University of California, Irvine, and the Technical University of Bydgoszcz on the theory of NTA in indirect semiconductors is presented. The theoretical work is based on the real density matrix approach (RDMA), where the density matrix is comprised of the populations of valence band electrons, conduction band electrons, and excitons present within the material. Applying spectrally distinct fields to the material results in an analytical expression for the TPA coefficient as a function of the frequency of these fields. The theory is verified with the aid of pump-probe experiments on silicon. Historical data for degenerate and non-degenerate observations for Si are also studied, revealing new physical insight into the nature of the NTA transition, highlighting the role of bound excitons.

From there, Chapter 4 describes the first application of NTA for spectroscopy and high-definition imaging in the MIR. Using a tunable picosecond light source, MIR spectroscopy of dimethyl sulfoxide (DMSO) with a Si photodiode as the detector is described. Subsequently, NTA-based widefield imaging using a silicon charge-coupled device (CCD) camera is demonstrated for the first time. Chemically selective imaging and videography is shown for a wide variety of samples, underlining the potential of the technique to greatly increase image acquisition speed. Faster imaging is achieved by replacing the Si camera with an

InGaAs imager, which resulted in a $50\times$ decrease in camera exposure time.

Chapter 5 extends this concept to high-speed 3D MIR imaging of objects. The requirement of high-irradiance sources inspired the use of ultrashort pulses for enabling NTA-based time-of-flight imaging. The arrival time of the signal pulse is selectively registered at the detector plane by the gate pulse. As the time delay between the gate pulse and the MIR pulse is scanned, a 3D object is reconstructed one *en face* plane at a time. This eliminates the need for raster scanning of samples as traditionally done by low-coherence sources. Moving the signal pulse into the MIR confers two additional benefits. The first is increased penetration depth, as light scattering by small particles is reduced for longer wavelengths. The second is the spectroscopic utility of MIR light. Chemically selective reflection data is encoded into the magnitude and arrival time, providing some insight into the material composition of samples. Ultimately, this work shows that using NTA for 3D MIR imaging enables chemically sensitive profiling at increased depths with drastically improved acquisition times from minutes per volume to seconds.

Chapter 6 presents the opportunity to greatly increase the spectral resolution of the MIR images by applying a positive chirp to the MIR pulse. By spreading the frequency content of the MIR pulse in time in a controlled fashion, temporal gating by the NIR pulse allows capturing of images at a MIR spectral resolution as high as 8 cm^{-1} . Scanning the time delay between the pulses then permits the acquisition of hyperspectral datasets. While temporal gating reduces the overall NTA signal, we show that this approach nonetheless enables video rate image acquisition. Spectral imaging of several samples is demonstrated, with components discriminated by their MIR absorption spectrum. This result showcases that true MIR hyperspectral videography of targets may be possible in the near future.

Chapter 2

Basic Principles of One- and Two-Photon Absorption

The basic physics of one- and two-photon absorption are described here through quantization of the field and the material using Fermi's Golden Rule. We first discuss single photon absorption of an isotropic ensemble of molecules and relate the rate of optical transitions to the macroscopic susceptibility and absorption coefficient. Following this, we describe similar transitions for semiconducting materials.

From there, we then discuss the relationship of the transition rate for two-photon absorption to the third-order susceptibility and degenerate two-photon absorption coefficient for the same molecular systems. This is extended to include nondegenerate two-photon absorption, where the input fields differ in frequency. For two-photon transitions in semiconductors, the emphasis is placed on extracting "scaling laws" that arise in the absorption coefficient for these materials. All expressions below are in SI units.

2.1 Linear absorption

2.1.1 Fermi's Golden Rule and molecular transitions

We start by introducing Fermi's Golden Rule and apply it to optical transitions in molecules. Consider a system that is in a quantum state that includes both material and field degrees of freedom. We are interested in the rate at which this system is able to transition from one energy state to another. To achieve this, we will describe the system in terms of a composite wavefunction and apply perturbation theory to study the effect of light-matter coupling.

If the system is initially in state $|i\rangle$, the transition rate to final states $|f\rangle$ is given by *Fermi's golden rule* as follows:

$$W_{i \rightarrow f} = \frac{2\pi}{\hbar^2} \sum_f \left| \langle f | \hat{V}_R | i \rangle \right|^2 \delta(\omega_f - \omega_i) \quad (2.1)$$

which has units of s^{-1} . The delta function describes the resonance condition, where $\hbar\omega_i$ is the initial energy of the system and $\hbar\omega_f$ is its final energy. The light-matter interaction Hamiltonian is indicated by \hat{V}_R . For molecular systems we choose the interaction Hamiltonian to be of a simple dipolar form. This assumption is justified as the molecule is much smaller than the wavelength of light and the dipolar response is expected to be dominant. Under these conditions, we can write the interaction Hamiltonian as [52]:

$$\begin{aligned} \hat{V}_R(\mathbf{r}, t) &= -\hat{\mathbf{E}}(\mathbf{r}, t) \cdot \hat{\boldsymbol{\mu}}(\mathbf{r}) \\ &= -\sum_{\mathbf{k}, \mu} \mathbf{e}_\mu \cdot \hat{\boldsymbol{\mu}}(\mathbf{r}) \left\{ E_k(\mathbf{r}, t) \hat{a}_{\mathbf{k}, \mu} + E_k^*(\mathbf{r}, t) \hat{a}_{\mathbf{k}, \mu}^\dagger \right\} \end{aligned} \quad (2.2)$$

where \mathbf{e}_μ is the field polarization vector, \mathbf{k} is the quantized field mode, $\hat{\boldsymbol{\mu}}$ is the transition dipole operator, and $\hat{a}_{\mathbf{k}, \mu}$ and $\hat{a}_{\mathbf{k}, \mu}^\dagger$ are the annihilation and creation operators, respectively.

The single-mode field amplitudes are defined as:

$$E_k(\mathbf{r}, t) = i \left(\frac{\hbar\omega_k}{2V\varepsilon_0} \right)^{1/2} e^{i(\mathbf{k}\cdot\mathbf{r}-\omega_k t)} \quad (2.3)$$

We next use equation (2.1) to derive an expression for linear absorption. For the initial state we write $|n, a\rangle$, where n denotes the quantum state of the radiation field and a is the groundstate of the material (molecule). For the radiation field, we assume a single mode \mathbf{k} with angular frequency ω_k . The total unperturbed Hamiltonian for this system is given by $\hat{H}_m + \hat{H}_R$, where \hat{H}_m is the Hamiltonian for the molecule and \hat{H}_R the Hamiltonian for the radiation field. The energy of the initial state is then:

$$\hbar\omega_i = \langle n, a | \hat{H}_m + \hat{H}_R | n, a \rangle = \hbar\omega_a + (n + \frac{1}{2})\hbar\omega_k$$

To simplify things, we also assume that the molecule only has a single excited state b . The matrix element of the interaction Hamiltonian can be evaluated as follows:

$$\begin{aligned} \langle f | \hat{V}_R | i \rangle &= - \langle f | \mathbf{e} \cdot \hat{\boldsymbol{\mu}} \{ E_k(t) \hat{a}_k + E_k^*(t) \hat{a}_k^\dagger \} | n, a \rangle \\ &= - \langle f | \mathbf{e} \cdot \hat{\boldsymbol{\mu}} E_k(t) \hat{a}_k | n, a \rangle - \langle f | \mathbf{e} \cdot \hat{\boldsymbol{\mu}} E_k^*(t) \hat{a}_k^\dagger | n, a \rangle \\ &= - \mathbf{e} \cdot \boldsymbol{\mu}_{ba} \sqrt{n} \langle f | n-1, b \rangle E_k(t) - \mathbf{e} \cdot \boldsymbol{\mu}_{ba} \sqrt{n+1} \langle f | n+1, b \rangle E_k^*(t) \end{aligned}$$

For a single excited state b , only the first term survives as a final state for which the both the radiation field and the molecule have gained an energy quantum violates conservation of energy. We thus have $\langle f | = \langle n-1, b |$ so that,

$$\langle f | \hat{V}_R | i \rangle = \langle n-1, b | \hat{V}_R | n, a \rangle = -i \mathbf{e} \cdot \boldsymbol{\mu}_{ba} \sqrt{n} \left(\frac{\hbar\omega_k}{2V\varepsilon_0} \right)^{1/2} e^{i(\mathbf{k}\cdot\mathbf{r}-\omega_k t)} \quad (2.4)$$

and the energy of the final state of the system is,

$$\hbar\omega_f = \langle n-1, b | \hat{H}_m + \hat{H}_R | n-1, b \rangle = \hbar\omega_b + (n - \frac{1}{2})\hbar\omega_k$$

Dropping the subscript \mathbf{k} for the field mode considered, we can now write equation (2.1) as:

$$W_{i \rightarrow f} = \frac{\pi n \omega}{\hbar V \varepsilon_0} |\mathbf{e} \cdot \boldsymbol{\mu}_{ba}|^2 \delta(\omega_{ba} - \omega) \quad (2.5)$$

where $\omega_{ba} = \omega_b - \omega_a$. The rate of absorption in Watts per unit volume can then be formulated as:

$$S_{\text{abs}} = N \hbar \omega W_{i \rightarrow f} = \pi \left(\frac{\omega}{c}\right) I(\omega) \frac{N}{\varepsilon_0 \hbar} |\mathbf{e} \cdot \boldsymbol{\mu}_{ba}|^2 \delta(\omega_{ba} - \omega) \quad (2.6)$$

where N is the number density of molecules, and $I(\omega) = c n \hbar \omega / V$ is the intensity of the field mode considered.

Equation (2.6) can be written in an alternative form by using the following expression of the delta function:

$$\delta(\omega) = \frac{1}{\pi} \lim_{\Gamma \rightarrow 0} \frac{\Gamma}{\omega^2 + \Gamma^2} \quad (2.7)$$

which corresponds to a sharp Lorentzian line with a linewidth of 2Γ . The absorption rate can now be written as:

$$S_{\text{abs}} = \left(\frac{\omega}{c}\right) I(\omega) \left\{ \lim_{\Gamma \rightarrow 0} \frac{N |\mathbf{e} \cdot \boldsymbol{\mu}_{ba}|^2}{\varepsilon_0 \hbar} \frac{\Gamma}{(\omega_{ba} - \omega)^2 + \Gamma^2} \right\} \quad (2.8)$$

Our next step is to assume that the molecules in our sample are isotropically oriented. This allows us to perform an orientational average over the Euler angles (ϕ, θ, ψ) , defined in the

following way [53]:

$$\langle f(\phi, \theta, \psi) \rangle = \frac{1}{8\pi^2} \int_0^{2\pi} \int_0^\pi \int_0^{2\pi} p(\phi, \theta, \psi) f(\phi, \theta, \psi) \sin \theta d\phi d\theta d\psi \quad (2.9)$$

where $p(\phi, \theta, \psi)$ is the probability of a given orientation. For an isotropic distribution $p = 1$ and we may evaluate the function $|\mathbf{e} \cdot \boldsymbol{\mu}_{ba}|^2 = |\boldsymbol{\mu}_{ba}|^2 \cos^2 \theta$ as $|\boldsymbol{\mu}_{ba}|^2 \langle \cos^2 \theta \rangle = \frac{1}{3} |\boldsymbol{\mu}_{ba}|^2$. For small dephasing rates Γ , we may now write the absorption rate as:

$$S_{\text{abs}} = \left(\frac{\omega}{c} \right) I(\omega) \text{Im} \{ \chi^{(1)}(\omega) \} \quad (2.10)$$

where the linear susceptibility for isotropic samples is defined as:

$$\chi^{(1)}(\omega) = \frac{N}{3\varepsilon_0 \hbar} \left\{ \frac{|\boldsymbol{\mu}_{ba}|^2}{\omega_{ba} - \omega - i\Gamma} \right\} \quad (2.11)$$

We thus see that the rate of linear absorption is proportional to the imaginary part of the linear susceptibility and linearly dependent on the incident intensity $I(\omega)$.

2.1.2 Linear absorption coefficient

We can relate expression (2.6) to the linear absorption coefficient $\alpha(\omega)$. The amount of absorbed intensity by a slab of thickness dz can be formulated as:

$$dI(\omega, z) = S_{\text{abs}} dz = -\alpha(\omega) I(\omega, z) dz \quad (2.12)$$

so that

$$\frac{dI(\omega, z)}{dz} = -\alpha(\omega) I(\omega, z) \quad (2.13)$$

Comparing (2.6) and (2.12) retrieves the absorption coefficient as:

$$\alpha(\omega) = \left(\frac{\omega}{c}\right) \text{Im} \{ \chi^{(1)}(\omega) \} \quad (2.14)$$

which is valid in weakly absorbing media such that the real part of the refractive index of the material can be approximated as $n \rightarrow 1$. The linear absorption coefficient has units of m^{-1} .

The differential equation shown in (2.13) can be solved exactly:

$$I(\omega, z) = I_0 e^{-\alpha(\omega)z} \quad (2.15)$$

where I_0 is the intensity incident on the material. This result is known as the Bouguer-Beer-Lambert law for linear absorption, which is seen to follow a decaying exponential profile as a function of the penetration depth z .

2.1.3 Linear absorption in semiconductors

Semiconductors consists of atomic lattices that exhibit periodicity. For bulk semiconducting materials, it is no longer appropriate to simply make the assumption that optical absorption is mediated by point absorbers that respond in a purely dipolar fashion. Instead, the extended character of the material and its periodicity have to be taken into account from the start. For this reason, the interaction Hamiltonian takes on the form of the minimal coupling Hamiltonian in its $\mathbf{A} \cdot \mathbf{p}$ form, as follows [54]:

$$\hat{V}_R = -\frac{e}{m} \hat{\mathbf{A}}(\mathbf{r}, t) \cdot \hat{\mathbf{p}}(\mathbf{r}) \quad (2.16)$$

where m is the electron mass, $\hat{\mathbf{A}}$ is the vector potential operator and $\hat{\mathbf{p}} = -i\hbar\nabla$ is the momentum operator. Using the Coulomb gauge, the vector potential can be related to the time-harmonic electric operator field:

$$\begin{aligned}\hat{\mathbf{E}}(\mathbf{r}, t) &= -\frac{d\hat{\mathbf{A}}(\mathbf{r}, t)}{dt} = i\omega\hat{\mathbf{A}} \\ &= \sum_{\mathbf{k}, \mu} \mathbf{e}_\mu \left\{ E_k(\mathbf{r}, t)\hat{a}_{\mathbf{k}, \mu} + E_k^*(\mathbf{r}, t)\hat{a}_{\mathbf{k}, \mu}^\dagger \right\}\end{aligned}\tag{2.17}$$

where the field amplitude is defined as in equation (2.3). We will assume an incident field of a fixed polarization direction, so that we can drop the μ subscript for the polarization vector.

Compared to molecular systems, which can often be described conveniently by discrete states, the electronic structure of semiconductors is more complicated. Besides the \mathbf{k} -dependence of the material states, the states are organized into quasi-continuous band structures, each with their own dispersion (energy versus \mathbf{k}) behavior. For this purpose, we need to specify the dispersion of the states in the valence and conduction bands, which we assume have a simple parabolic form:

$$E_v(\mathbf{k}) = E_{0v} - \frac{\hbar^2 k^2}{2m_v}\tag{2.18}$$

$$E_c(\mathbf{k}) = E_{0c} + \frac{\hbar^2 k^2}{2m_c}\tag{2.19}$$

Here E_{0v} is the energy at the top of the valence band, whereas E_{0c} is energy at the bottom of the conduction band as shown in Figure 2.1. We also define the *bandgap energy* as $E_g = E_{0c} - E_{0v}$. The mass m_v is the mass of the hole in the valence band, and m_c represents the electron mass in the conduction band, both of which are defined here as positive values. We will consider interband optical transitions in the material, from the valence to the conduction

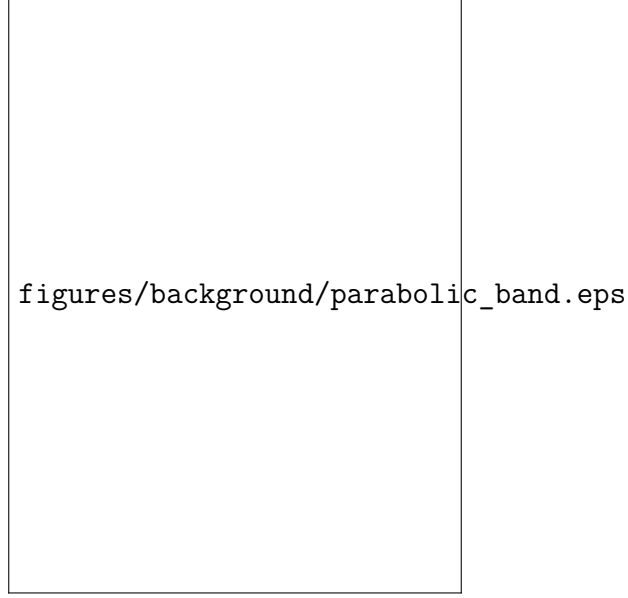


Figure 2.1: Dispersion diagram of parabolic valence and conduction bands in semiconductors. The linear absorption process is indicated by the orange arrows for a given point in \mathbf{k} -space, symbolizing a vertical transition.

band. In this case, the energy difference in the material due to an optical transition is:

$$E_{cv}(\mathbf{k}', \mathbf{k}) = E_c(\mathbf{k}') - E_v(\mathbf{k}) \quad (2.20)$$

A special case occurs when $\mathbf{k}' = \mathbf{k}$, which corresponds to vertical transitions in the dispersion diagram, which yields:

$$\begin{aligned} E_{cv}(\mathbf{k}, \mathbf{k}) &= E_g + \frac{\hbar^2 k^2}{2m_c} + \frac{\hbar^2 k^2}{2m_v} \\ &= E_g + \frac{\hbar^2 k^2}{2m_{cv}} \end{aligned} \quad (2.21)$$

where m_{cv} is the reduced conduction-valence effective mass, defined through:

$$\frac{1}{m_{cv}} = \frac{1}{m_c} + \frac{1}{m_v} \quad (2.22)$$

Equation (2.21) will be relevant in the calculation of the transition rate of linear absorption in this two-band model of the semiconductor.

To calculate the transition rate, taking equation (2.1) as the starting point, we first need to define the initial and final states of our combined light-matter system. We may indicate the initial state as $|i\rangle = |n, v\rangle$, where n is the photon occupation number and v indicates that the material state is found in the valence band. The final state is then $|f\rangle = |n - 1, c\rangle$. Limiting ourselves to absorptive events, only operations with the \hat{a} operator in equation (2.17) are relevant. Under these conditions, the matrix elements $V_{fi} \equiv \langle f | \hat{V}_R | i \rangle$ can be written as:

$$V_{cv} = \frac{e}{im\omega} \left(\frac{I(\omega)}{2c\varepsilon_0} \right)^{1/2} \langle c | e^{i\mathbf{q}_0\mathbf{r}} \mathbf{e} \cdot \hat{\mathbf{p}} | v \rangle \quad (2.23)$$

where we have re-written the photon wave vector in free space \mathbf{q}_0 as a plane wave, and the photon number states are implied to focus on the material response. Fermi's Golden Rule in equation (2.1) can now be recast as:

$$\begin{aligned} W_{i \rightarrow f} &= \frac{2\pi}{\hbar} |V_{cv}|^2 \delta(E_f - E_i) \\ &= \frac{2\pi}{\hbar} \left(\frac{e}{m\omega} \right)^2 \left(\frac{I(\omega)}{2c\varepsilon_0} \right) |\langle c | e^{i\mathbf{q}_0\mathbf{r}} \mathbf{e} \cdot \hat{\mathbf{p}} | v \rangle|^2 \delta(E_c(\mathbf{k}') - E_v(\mathbf{k}) - \hbar\omega) \end{aligned} \quad (2.24)$$

where we have written the resonance condition described by the delta function in terms of energy rather than angular frequency. To arrive at the second line in (2.24), we have integrated out the field states but not yet evaluated the integral over the material states.

To evaluate the resulting matrix element, we assume Bloch states for the material, which are specified by their wave vector \mathbf{k} . For the initial state we now write $|v, \mathbf{k}\rangle$, whereas the final state is formulated as $|c, \mathbf{k}'\rangle$. The Bloch states can be written as $\psi_{n,\mathbf{k}}(\mathbf{r}) = u_n(\mathbf{r})e^{i\mathbf{k}\mathbf{r}}$. We can then evaluate the matrix elements as:

$$\begin{aligned} \langle c, \mathbf{k}' | e^{i\mathbf{q}_0\mathbf{r}} \hat{\mathbf{p}} \cdot \mathbf{e} | v, \mathbf{k} \rangle &= \int d^3\mathbf{r} u_c^*(\mathbf{r}) e^{-i\mathbf{k}'\mathbf{r}} e^{i\mathbf{q}_0\mathbf{r}} \hat{\mathbf{p}} \cdot \mathbf{e} u_v(\mathbf{r}) e^{i\mathbf{k}\mathbf{r}} \\ &= \int d^3\mathbf{r} u_c^*(\mathbf{r}) e^{i(\mathbf{q}_0 - \{\mathbf{k}' - \mathbf{k}\})\mathbf{r}} \{ \hbar\mathbf{k} + \hat{\mathbf{p}} \} \cdot \mathbf{e} u_v(\mathbf{r}) \end{aligned} \quad (2.25)$$

This produces two integrals. In order to further evaluate them, we note that the $u_n(\mathbf{r})$ func-

tions vary rapidly with a lattice cell, whereas the complex exponential is virtually invariant over the length of cell. The former is a property of the cell whereas the latter is a property of the entire lattice. We can use the lattice vector \mathbf{R} to describe variation on the level of the lattice, whereas \mathbf{r} provides the scale for variations within the cell. The first integral can now be written as:

$$\hbar\mathbf{k} \cdot \mathbf{e} \int d^3\mathbf{r} u_c(\mathbf{r}) e^{i(\mathbf{q}_0 - \{\mathbf{k}' - \mathbf{k}\})\mathbf{r}} u_v(\mathbf{r}) = \hbar\mathbf{k} \cdot \mathbf{e} \sum_m e^{i(\mathbf{q}_0 - \{\mathbf{k}' - \mathbf{k}\})\mathbf{R}_m} \times \int_{\text{cell}} d^3\mathbf{r} u_c^*(\mathbf{r}) u_v(\mathbf{r})$$

which is zero because of the orthogonality of the $u_n(\mathbf{r})$ wavefunctions. In the same fashion, the second integral is evaluated as:

$$\sum_m^N e^{i(\mathbf{q}_0 - \{\mathbf{k}' - \mathbf{k}\})\mathbf{R}_m} \int_{\text{cell}} d^3\mathbf{r} u_c^*(\mathbf{r}) \hat{\mathbf{p}} \cdot \mathbf{e} u_v(\mathbf{r}) \approx \delta_{\mathbf{q}_0, \mathbf{k}' - \mathbf{k}} \mathbf{p}_{cv}$$

where the summation over all N lattice cells takes the form of a Kronecker delta function when $N \rightarrow \infty$. The resulting matrix element $\mathbf{p}_{cv} = \langle c | \hat{\mathbf{p}} \cdot \mathbf{e} | v \rangle$ represents the contribution of all lattice cells. The transition rate is now:

$$W_{i \rightarrow f} = \frac{2\pi}{\hbar} \left(\frac{e}{m\omega} \right)^2 \left(\frac{I(\omega)}{2c\epsilon_0} \right) |\mathbf{p}_{cv}|^2 \delta_{\mathbf{q}_0, \mathbf{k}' - \mathbf{k}} \delta(E_{cv}(\mathbf{k}, \mathbf{k}') - \hbar\omega) \quad (2.26)$$

After summing over all *final* states \mathbf{k}' , the transition rate R_{cv} from the valence to the conduction band is:

$$W_{cv} = \sum_{\mathbf{k}'} W_{i \rightarrow f} = \frac{\pi}{\hbar c \epsilon_0} \left(\frac{e}{m\omega} \right)^2 |\mathbf{p}_{cv}|^2 I(\omega) \delta(E_{cv}(\mathbf{k}, \mathbf{k} + \mathbf{q}_0) - \hbar\omega) \quad (2.27)$$

Equation (2.27) reveals that the transition probability (i) scales linearly with the incident intensity, (ii) depends on the square of the *interband momentum matrix* element \mathbf{p}_{cv} , and (iii) grows when the photon energy approaches the transition energy $E_{cv}(\mathbf{k}, \mathbf{k} + \mathbf{q}_0)$. This last notion reveals the momentum conservation $\mathbf{k}' = \mathbf{k} + \mathbf{q}_0$ condition, which states that

the accessible states in the transition are those \mathbf{k} -states that have a crystal momentum that differs by \mathbf{q}_0 , which is proportional to the photon momentum. Given that $|\mathbf{q}_0| \sim 2\pi/\lambda$, which is very small compared the values of $|\mathbf{k}|$ throughout the first Brillouin zone, the allowed transitions are those that occur for $\mathbf{k}' \approx \mathbf{k}$, i.e. vertical transitions in \mathbf{k} -space.

Equation (2.27) gives the transition rate in s^{-1} for a given point \mathbf{k} in \mathbf{k} -space. The total rate, integrated over all possible \mathbf{k} in the first Brillouin zone can be computed as:

$$R_{cv} = \frac{1}{4\pi^3} \int W_{cv} d^3\mathbf{k} = \frac{1}{4\pi^3} \int W_{cv} k^2 dk \sin\theta d\theta d\phi \quad (2.28)$$

Note that the units of the rate are now in $(\text{s} \cdot \text{m}^3)^{-1}$. In performing the integration, it is common to assume that the matrix element \mathbf{p}_{cv} only weakly depends on \mathbf{k} , so that it can be taken out of the integral, yielding the term $\langle |\mathbf{p}_{cv}|^2 \rangle$, where the brackets indicate the angular average in \mathbf{k} -space. The transition rate is now expressed as:

$$\frac{1}{4\pi^2 \hbar c \epsilon_0} \left(\frac{e}{m\omega} \right)^2 \langle |\mathbf{p}_{cv}|^2 \rangle I(\omega) \int \delta(E_{cv}(\mathbf{k}, \mathbf{k}) - \hbar\omega) d^3\mathbf{k}$$

To evaluate the integral we make use of the following property of the delta function:

$$\delta(g(k)) = \frac{\delta(k - k_0)}{|g'(k_0)|}$$

where $g(k)$ is a continuously differentiable function and k_0 is its root. Making use of equation (2.21), we may write:

$$g(k) = \frac{k^2 \hbar^2}{2m_{cv}} + E_g - \hbar\omega$$

which yields $k_0 = \sqrt{2m_{cv}(\hbar\omega - E_g)}/\hbar$ and $g'(k_0) = \sqrt{2\hbar^2(\hbar\omega - E_g)/m_{cv}}$, so that:

$$\frac{1}{4\pi^3} \int \delta(E_{cv}(\mathbf{k}, \mathbf{k}) - \hbar\omega) d^3\mathbf{k} = \frac{1}{2\pi^2} \left(\frac{2m_{cv}}{\hbar^2} \right)^{3/2} (\hbar\omega - E_g)^{1/2} \equiv f(E) \quad (2.29)$$

This last expression is known as the *joint density of states* of the simple two-band model, and it measures the number of pairs of valence-conduction band states per unit volume and per unit energy interval that have an energy separation $E = \hbar\omega$. This expression is valid for the case when the valence band is nearly full and the conduction band is initially empty. The transition rate per unit volume for the case of a linear interband transition is now:

$$R_{cv} = \frac{\pi}{\hbar c \epsilon_0} \left(\frac{e}{m\omega} \right)^2 f(E) I(\omega) \langle |\mathbf{p}_{cv}|^2 \rangle \quad (2.30)$$

which is directly proportional to the joint density of states. The values for $\langle |\mathbf{p}_{cv}|^2 \rangle$ are often known and commonly expressed as $E_p = 6 \langle |\mathbf{p}_{cv}|^2 \rangle / m$. For instance, $E_p = 22.7$ eV for GaAs, 22.4 eV for InSb and 17.0 eV for InP [55].

The rate of absorption in Watts per unit volume can be written in a manner similar to equation (2.6):

$$S_{\text{abs}} = \hbar\omega R_{cv} = \frac{\pi e^2}{m^2 \omega c \epsilon_0} f(E) \langle |\mathbf{p}_{cv}|^2 \rangle I(\omega) = \alpha(\omega) I(\omega) \quad (2.31)$$

which defines the linear absorption coefficient of the semiconducting material. In comparing the expressions obtained for the transition rates for molecular and semiconductor one photon absorption, two differences are revealed. The coupling of the two discrete molecular states is given by the magnitude of the dipole operator $\boldsymbol{\mu}_{ba}$. For semiconductors, the interband momentum matrix element \mathbf{p}_{cv} plays a similar role, but its value is averaged over the available valence and conduction band states of many unit cells. Furthermore, the presence of a singular excited state for the molecular system gives rise to a Lorentzian lineshape centered at the transition frequency ω_{ba} in equation (2.8). The joint density of states instead modulates the absorption rate based on the amount of transition opportunities admitted by the band structure.

2.2 Nonlinear absorption

2.2.1 Quantum description of two-photon absorption

We next apply Fermi's golden rule to describe the process of two-photon absorption (TPA) for an ensemble of molecules, where we assume a simple model of two material eigenstates, namely the ground state a and the excited state b . Unlike in linear absorption, the TPA transition $i \rightarrow f$ occurs via intermediate states n . In the wavefunction description, we must now perturb the system's state twice with \hat{V}_R , which can be achieved by considering the perturbation up to second-order. The transition rate is then given by:

$$W_{i \rightarrow f} = \frac{2\pi}{\hbar^2} \sum_f \left| \frac{1}{\hbar} \sum_n \frac{\langle f | \hat{V}_R | n \rangle \langle n | \hat{V}_R | i \rangle}{\omega_i - \omega_n} \right|^2 \delta(\omega_f - \omega_i) \quad (2.32)$$

which is the quantum mechanical form of the Kramers-Heisenberg formula [52]. We consider two incident fields, labeled as ω_1 with photon occupation number n_1 and ω_2 with photon occupation number n_2 . The quantum states of the system can then be formulated as $|n_1, n_2, m\rangle$, with m the quantum state of the molecule.

For simplicity, we initially consider only one quantum pathway, namely the one where the first interaction is with ω_1 and the second interaction with ω_2 . Using similar steps as outlined above, we find for the denominator in Equation 2.32:

$$\begin{aligned} \omega_i - \omega_n &= \{\omega_a + \omega_1 n_1 + \omega_2 n_2\} - \{\omega_n + \omega_1 (n_1 - 1) + \omega_2 n_2\} \\ &= \omega_{an} + \omega_1 = -(\omega_{na} - \omega_1) \end{aligned}$$

Similarly, the argument in the delta function is evaluated as:

$$\begin{aligned}\omega_f - \omega_i &= \{\omega_b + \omega_1(n_1 - 1) + \omega_2(n_2 - 1)\} - \{\omega_a + \omega_1 n_1 + \omega_2 n_2\} \\ &= \omega_{ba} - \omega_1 - \omega_2\end{aligned}$$

Finally, matrix elements in the numerator of equation (2.32) for the chosen pathway can be written as:

$$\begin{aligned}\langle n | \hat{V}_R | i \rangle &= \langle n_1 - 1, n_2, n | \hat{V}_R | n_1, n_2, a \rangle = -i \mathbf{e}_1 \cdot \boldsymbol{\mu}_{na} \sqrt{n_1} \left(\frac{\hbar \omega_1}{2V \epsilon_0} \right)^{1/2} e^{i(\mathbf{k}_1 \cdot \mathbf{r} - \omega_1 t)} \\ \langle f | \hat{V}_R | n \rangle &= \langle n_1 - 1, n_2 - 1, b | \hat{V}_R | n_1 - 1, n_2, n \rangle = -i \mathbf{e}_2 \cdot \boldsymbol{\mu}_{bn} \sqrt{n_2} \left(\frac{\hbar \omega_2}{2V \epsilon_0} \right)^{1/2} e^{i(\mathbf{k}_2 \cdot \mathbf{r} - \omega_2 t)}\end{aligned}$$

so that equation (2.32) takes on the form:

$$W_{i \rightarrow f} = \frac{n_1 n_2 \pi \omega_1 \omega_2}{2V^2 \epsilon_0^2} \left| \frac{1}{\hbar} \sum_n \frac{(\mathbf{e}_2 \cdot \boldsymbol{\mu}_{bn})(\mathbf{e}_1 \cdot \boldsymbol{\mu}_{na})}{\omega_{na} - \omega_1} \right|^2 \delta(\omega_{ba} - \omega_1 - \omega_2) \quad (2.33)$$

Defining the TPA polarizability tensor as follows:

$$\boldsymbol{\alpha}_{\text{TPA}}(\omega) = \frac{1}{\hbar} \sum_n \left\{ \frac{\boldsymbol{\mu}_{bn} \boldsymbol{\mu}_{na}}{\omega_{na} - \omega} \right\} \quad (2.34)$$

the total TPA transition rate can be written as:

$$W_{\text{TPA}} = \frac{n_1 n_2 \pi \omega_1 \omega_2}{2V^2 \epsilon_0^2} |\mathbb{M}|^2 \delta(\omega_{ba} - \omega_1 - \omega_2) \quad (2.35)$$

with

$$\mathbb{M} = \{\mathbf{e}_2 \cdot \boldsymbol{\alpha}_{\text{TPA}}(\omega_1) \cdot \mathbf{e}_1\} + \{\mathbf{e}_1 \cdot \boldsymbol{\alpha}_{\text{TPA}}(\omega_2) \cdot \mathbf{e}_2\} \quad (2.36)$$

where the second term represents a second pathway, namely one for which the first interaction

is with ω_2 and the second interaction with ω_1 . Using expression (2.7), equation (2.35) can be recast as:

$$W_{\text{TPA}} = \frac{I(\omega_1)I(\omega_2)}{2\hbar c^2 \varepsilon_0^2} |\mathbb{M}|^2 \text{Im} \left\{ \frac{1}{\hbar} \frac{1}{[\omega_{ba} - (\omega_1 + \omega_2) - i\Gamma_{ba}]} \right\} \quad (2.37)$$

We can further simplify the result by performing isotropic averaging again. This yields terms of the form $|\alpha_{\text{TPA}}|^2 \langle \cos^4 \theta \rangle = \frac{1}{5} |\alpha_{\text{TPA}}|^2$, where

$$\alpha_{\text{TPA}}(\omega) = \frac{1}{\hbar} \sum_n \left\{ \frac{|\boldsymbol{\mu}_{bn}| |\boldsymbol{\mu}_{na}|}{\omega_{na} - \omega} \right\} \quad (2.38)$$

Assuming $\omega = \omega_1 = \omega_2$, i.e. degenerate two-photon absorption, we can write the two-photon absorption rate as:

$$W_{\text{TPA}} = \frac{I^2(\omega)}{10\hbar c^2 \varepsilon_0^2} \text{Im} \left\{ \frac{1}{\hbar} \frac{|\alpha_{\text{TPA}}(\omega)|^2}{[\omega_{ba} - 2\omega - i\Gamma_{ba}]} \right\} \quad (2.39)$$

Equations (2.37) and (2.39) have the the following properties:

- The transition rate scales linearly with $I(\omega_1)$ and linearly with $I(\omega_2)$. In case of single beam illumination, the transition rate scales as $I^2(\omega)$.
- The transition rate increases when $\omega_1 + \omega_2$ approaches the transition frequency ω_{ba} of the material. This is the two-photon resonance condition.
- The transition rate also increases when the TPA polarizability approaches its resonance condition, which occurs when the intermediate state n approaches a real eigenstate, i.e. $n \rightarrow b$ in equation (2.34). We thus find that the TPA transition rate grows when either ω_1 or ω_2 get close to ω_{ba} .

2.2.2 Degenerate two-photon absorption coefficient

We next consider the case of degenerate two-photon absorption, so that $\omega = \omega_1 = \omega_2$ and the light intensity is described by $I(\omega, z)$. We also assume a medium that has, at a given angular frequency ω , negligible one-photon absorption, but non-negligible two-photon absorption. The change in intensity is then given by:

$$\frac{dI(\omega, z)}{dz} = -\alpha_2(\omega)I^2(\omega, z) \quad (2.40)$$

where $\alpha_2(\omega)$ is the *degenerate two-photon absorption coefficient*. This coefficient is formally defined as:

$$\alpha_2(\omega) = \frac{\text{power absorbed per unit volume in J}/(\text{s} \cdot \text{m}^3)}{\text{square of the incident intensity in J}^2/(\text{s}^2 \cdot \text{m}^4)} \quad (2.41)$$

and has units of m/W . The solution of equation (2.40) is:

$$I(\omega, z) = \frac{I_0}{1 + \alpha_2(\omega)zI_0} \quad (2.42)$$

Note that the distance-dependent intensity loss due to two-photon absorption is quite different from the intensity loss seen for linear absorption, which was given by equation (2.15). Figure 2.2 shows a comparison between the distance dependence of one-photon and two-photon absorption. Since the power absorbed in the mode ω per unit volume equals $2N\hbar\omega|W_{\text{TPA}}|$, with W_{TPA} defined as in equation (2.37), we can write α_2 in the following form:

$$\alpha_2(\omega) = \frac{2N\hbar\omega}{I_0^2}|W_{\text{TPA}}| \quad (2.43)$$

$$= \frac{\omega}{c^2\varepsilon_0} \text{Im} \left\{ \chi_{\text{TPA}}^{(3)}(\omega) \right\} \quad (2.44)$$

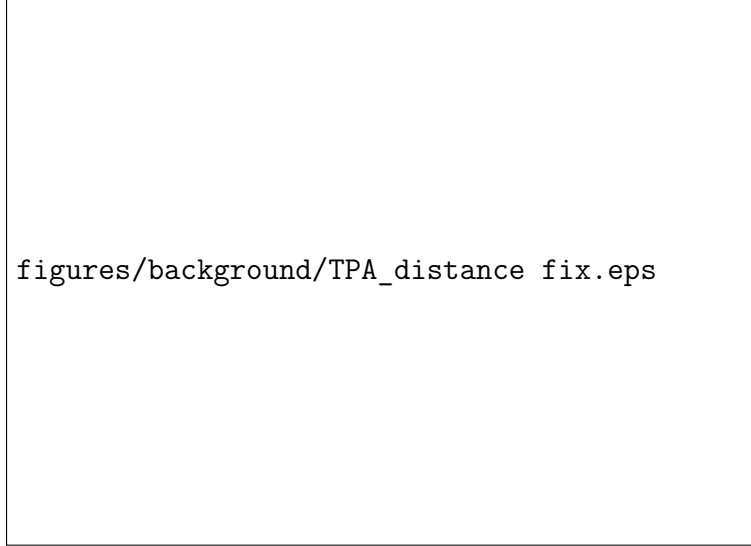


Figure 2.2: Intensity loss as a function of propagation distance due to absorption. Linear absorption (1PA, yellow line) was calculated for $\alpha = 0.05 \mu\text{m}^{-1}$ and two-photon absorption (TPA, red line) was calculated with an α_2 -coefficient that was scaled such that the two curves intersect at the 50% loss point. Because the TPA process depends nonlinearly on the incident intensity, it shows a steeper depth-dependence at shorter distances and a shallower depth-dependence at longer distances relative to the linear absorption curve.

where the third-order susceptibility for the degenerate two-photon absorption process is defined as:

$$\chi_{\text{TPA}}^{(3)}(\omega) = \frac{N}{5\varepsilon_0\hbar} \frac{|\alpha_{\text{TPA}}(\omega)|^2}{[\omega_{ba} - 2\omega - i\Gamma_{ba}]} \quad (2.45)$$

which is resonant when $2\omega = \omega_{ba}$ and grows when α_{TPA} reaches its resonance condition. Note that whereas the linear absorption coefficient is proportional to $\chi^{(1)}$, the two-photon absorption coefficient scales as $\chi^{(3)}$.

2.2.3 Non-degenerate two-photon absorption

In the case of non-degenerate two-photon absorption, i.e. $\omega_1 \neq \omega_2$, the change in the intensity of the incident light beams is described by two coupled differential equations. Writing

$I(\omega_1, z) \equiv I_1(z)$ and $I(\omega_2, z) \equiv I_2(z)$, we find

$$\begin{aligned}\frac{dI_1(z)}{dz} &= -\alpha_2(\omega_1, \omega_1)I_1^2(z) - \alpha_2(\omega_1, \omega_2)I_1(z)I_2(z) \\ \frac{dI_2(z)}{dz} &= -\alpha_2(\omega_2, \omega_2)I_2^2(z) - \alpha_2(\omega_2, \omega_1)I_1(z)I_2(z)\end{aligned}\tag{2.46}$$

For simplicity, we will assume that the polarization directions of the incident beams, \mathbf{e}_1 and \mathbf{e}_2 , are the same. In the above, $\alpha_2(\omega_i, \omega_j)$ describes the *non-degenerate two-photon absorption* (NTA) coefficient for $i \neq j$. In equation (2.46), the NTA coefficients are defined from the perspective of the incoming fields, and describe the optical loss experienced in one beam due to the presence of another. For the purpose of this thesis, it is also useful to define the NTA in an alternative fashion, namely it terms how much light energy is absorbed by the material due to the NTA process. In this case, the NTA coefficient can formally be defined as

$$\alpha_2(\omega_i + \omega_j) = \frac{\text{power absorbed per unit volume in J/(s} \cdot \text{m}^3\text{)}}{\text{incident intensity at } \omega_i \text{ times intensity at } \omega_j \text{ in J}^2\text{/(s}^2 \cdot \text{m}^4\text{)}}\tag{2.47}$$

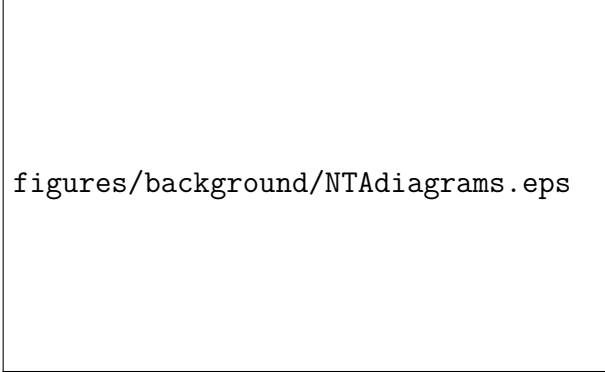
and, using the formalism in section 2.2.1, takes on the following form:

$$\alpha_2(\omega_i + \omega_j) = \frac{(\omega_i + \omega_j)}{2c^2\varepsilon_0} \text{Im} \left\{ \chi_{\text{TPA}}^{(3)}(\omega_i, \omega_j) \right\}\tag{2.48}$$

where

$$\chi_{\text{TPA}}^{(3)}(\omega_i, \omega_j) = \frac{N}{5\varepsilon_0\hbar} \sum_p \frac{|\alpha_{\text{TPA}}(\omega_i)|^2}{[\omega_{ba} - (\omega_i + \omega_j) - i\Gamma_{ba}]}\tag{2.49}$$

Note that there are two permutations (p) for the angular frequency ordering in equation (2.49), which means that there are two contributions to the overall NTA process. Writing the incident angular frequencies as ω_1 and ω_2 , the general resonance condition for the NTA coefficient is $\omega_1 + \omega_2 = \omega_{ba}$. In addition, the NTA coefficient increases when $\alpha_{\text{TPA}}(\omega_i)$ reaches a resonance, which occurs when ω_i approaches ω_{na} where $|n\rangle$ is a real state. A special situation occurs when $\omega_i \rightarrow \omega_{ba}$, which means that one of the photon energies gets



figures/background/NTAdiagrams.eps

Figure 2.3: Two Jablonski diagrams depicting the two permutations of the NTA process for system with two (real) states a and b , denoted by the solid black lines. The virtual intermediate state n is indicated by the dotted line. In this example, $\omega_1 > \omega_2$. In the case of extreme NTA, ω_1 approaches ω_{ba} and ω_2 approaches zero, giving rise to an increase of the NTA coefficient.

very close to the targeted two-photon transition frequency. Similarly, when $\omega_{na} \rightarrow 0$ and ω_i is very small, a second pre-resonance condition is at play. Both situations are referred to as *extreme* NTA, as sketched in Figure 2.3. Under such conditions, we may expect very high values of the NTA coefficient [56].

2.2.4 Two-photon absorption in semiconductors

Proper descriptions of two-photon absorption in semiconductors can be very complex. More accurate models can include detailed band structures and spin [57–59]. In line with the previous parabolic band structure considered, we attempt to provide a grossly simplified description that highlights the main physical characteristics of interband two-photon excitations in semiconductors.

Our goal is to cast the two-photon absorption signal in terms of the Kramers-Heisenberg expression, given in equation (2.32). Based on our analysis in section 2.1.3, we can write the

matrix elements of the interaction Hamiltonian as:

$$V_{fi}(\omega) = \frac{e}{im\omega} \left(\frac{I(\omega)}{2c\varepsilon_0} \right)^{1/2} \mathbf{p}_{fi} \delta_{\mathbf{q}_0, \mathbf{k}_f - \mathbf{k}_i} \quad (2.50)$$

where the spatial integration over the lattice cells has been performed, but we have not taken the orientational average. Note that expression (2.50) contains the momentum conservation condition for a given $i \rightarrow f$ transition. We will assume that the optical transitions are vertical, so that $\mathbf{k}_f \approx \mathbf{k}_i$. In this case we can simply write for energy differences $E_f(\mathbf{k}_f) - E_i(\mathbf{k}_i) = E_{fi}(\mathbf{k})$. Note that $E_g = E_{cv}(0)$. The transition rate can now be written as:

$$W_{cv} = \frac{2\pi}{\hbar} \sum_p \left| \sum_n \frac{V_{cn}(\omega_2)V_{nv}(\omega_1)}{E_{nv}(\mathbf{k}) - \hbar\omega_1} \right|^2 \delta(E_{cv}(\mathbf{k}) - \{\hbar\omega_1 + \hbar\omega_2\}) \quad (2.51)$$

The summation is over the two frequency permutations (p) of the incident angular frequencies ω_1 and ω_2 . To calculate the rate per unit volume, we integrate over all \mathbf{k} in the first Brillouin zone, as in equation (2.28), which yields [60]:

$$R_{cv} = \frac{2\pi}{\hbar} \left(\frac{e^2}{m^2\omega_1\omega_2} \right)^2 \frac{I(\omega_1)I(\omega_2)}{4c^2\varepsilon_0} \sum_p f(\hbar\omega_1 + \hbar\omega_2) \langle |S_{cv}(k)|^2 \rangle \quad (2.52)$$

with

$$S_{cv}(k) = \sum_n \frac{\mathbf{p}_{cn}\mathbf{p}_{nv}}{E_{nv}(k) - \hbar\omega_1} \quad (2.53)$$

and where it is assumed that the polarization vectors \mathbf{e} of the incident fields are the same. In (2.53), $k = \sqrt{2m_{cv}(\hbar\Omega - E_g)}/\hbar$ refers to the magnitude of the electron wavevector for the transition at point \mathbf{k} in the first Brillouin zone, and $\Omega = \omega_1 + \omega_2$. Equation (2.52) shows similarities with the two-photon transition rate derived for the molecular system in equation (2.37), as both show a linear dependence on $I(\omega_1)$ and $I(\omega_2)$. Compared to the single Lorentzian peak contained in equation (2.37), the multi-photon resonance condition

for the transition rate per unit volume of the semiconductor system is captured by the joint density of states $f(\hbar\Omega)$. This function is poorly defined when $\hbar\Omega < E_g$, and grows as the square root of $(\hbar\Omega - E_g)$ when the combined photon energy exceeds the bandgap energy. Finally, the $\langle |S_{cv}(k)|^2 \rangle$ term in (2.52) plays a role similar to $|\alpha_{\text{TPA}}|^2$ of the molecular system.

2.2.5 Scaling rules for two-photon absorption in semiconductors

In the context of the two-band model, the two-photon absorption coefficient in semiconducting systems is obtained from equation (2.52) as:

$$\begin{aligned} \alpha_2(\omega_1 + \omega_2) &= \frac{\hbar\Omega}{I(\omega_1)I(\omega_2)} R_{cv} \\ &= \frac{\pi\Omega}{2c^2\varepsilon_0} \left(\frac{e^2}{m^2\omega_1\omega_2} \right)^2 \sum_p f(\hbar\omega_1 + \hbar\omega_2) \langle |S_{cv}(k)|^2 \rangle \end{aligned} \quad (2.54)$$

It is often of interest to examine the magnitude of α_2 as a function of the dimensionless incident photon energy $x = \hbar\Omega/E_g$. To study how the $S_{cv}(k)$ term scales with x , we need to evaluate the matrix elements \mathbf{p}_{nv} and \mathbf{p}_{cn} . Whereas good estimates are available for \mathbf{p}_{cv} , which is associated with fundamental interband transitions, the involvement of a virtual state (n) renders such matrix elements ill-defined in the two-band model. Therefore, it is common to describe $S_{cv}(k)$ in terms of \mathbf{p}_{cv} and \mathbf{p}_{ii} , where $i = c, v$. The latter matrix elements are associated with *intragap* transitions, and can be expressed in terms of known parameters, as follows [60]:

$$\mathbf{p}_{ii} = s_i \frac{m}{m_i} \hbar k \quad (2.55)$$

where $s_i = 1$ when $i = c$ and -1 when $i = v$. For the interband transitions, the following relation will be useful:

$$\mathbf{p}_{cv} = fmP/\hbar \quad (2.56)$$

where f is a scaling parameter and P is known as Kane's momentum parameter [61]. Using this definition, it is also possible to express the reduced mass in terms of P [60]:

$$m_{cv} = \frac{E_g \hbar^2}{4f^2 P^2} \quad (2.57)$$

Describing the two-photon process in terms of just \mathbf{p}_{cv} , \mathbf{p}_{cc} and \mathbf{p}_{vv} may yield tangible expressions, but the question arises what it means when the first or last step in the two-photon light-matter interaction is an intraband transition. Such intraband transitions have low transition energies, i.e. $E_{ii}(k) \rightarrow 0$, which can be much lower than the photon energy $\hbar\omega$, and thus appear to violate the conservation of energy during the process, see Figure 2.4. However, whereas the initial and final states in the perturbation description need to abide by the conservation of energy (and momentum), such a requirement is relaxed for the intermediate steps. In this context, the final expressions obtained by making the assumptions above are still meaningful, although care should be taken when trying to physically interpret the process during intermediate steps.

Proceeding with the strategy outlined above, the $S_{cv}(k)$ term can now be expressed as:

$$\begin{aligned} S_{cv}(k) &= \frac{\mathbf{p}_{cv}\mathbf{p}_{vv}}{E_{vv}(k) - \hbar\omega_1} + \frac{\mathbf{p}_{cc}\mathbf{p}_{cv}}{E_{cv}(k) - \hbar\omega_1} \\ &= \frac{\mathbf{p}_{cv}\mathbf{p}_{vv}}{-\hbar\omega_1} + \frac{\mathbf{p}_{cc}\mathbf{p}_{cv}}{\hbar\omega_2} \\ &= \mathbf{p}_{cv}k \left\{ \left(\frac{m}{m_c} \right) \frac{1}{\omega_2} + \left(\frac{m}{m_v} \right) \frac{1}{\omega_1} \right\} \end{aligned} \quad (2.58)$$

where the second line follows from $E_{vv}(k) \sim 0$ and $E_{cv}(k) = \hbar\Omega$. For simplicity, we consider



Figure 2.4: Two-photon absorption in the two-band model, described in terms of a fundamental interband transition (orange arrow), mediated by \mathbf{p}_{cv} , and an intraband transition (red arrow), mediated by \mathbf{p}_{cc} or \mathbf{p}_{vv} . Both frequency permutations are shown.

the degenerate case so that $\omega_1 = \omega_2$, in which case expression (2.58) takes on the simple form $S_{cv}(k) = \mathbf{p}_{cv}mk/(m_{cv}\omega)$. Using this result and expressing m_{cv} as in equation (2.57), we can write the degenerate two-photon absorption coefficient as:

$$\alpha_2(\omega) = f' \frac{2^5 \sqrt{2}}{\pi \varepsilon_0} \left(\frac{e^2}{c\hbar} \right)^2 \frac{P}{E_g^3} F_{\text{DTA}}(x) \quad (2.59)$$

where f' is another scaling parameter and the function $F_{\text{DTA}}(x)$ is defined as [60, 62]:

$$F_{\text{DTA}}(x) = \frac{(x-1)^{3/2}}{x^5} \quad (2.60)$$

with $x = 2\hbar\omega/E_g$. We see that $\alpha_2(\omega)$ scales as E_g^{-3} , and thus increases for materials with smaller bandgap energies. Figure 2.5 compares the linear absorption coefficient α as a function of x along with the degenerate two-photon absorption coefficient α_2 . Within the parabolic two-band model, the linear absorption coefficient scales with the square root of the gap energy, but begins to decrease as the ω^{-1} term in equation (2.31) becomes more

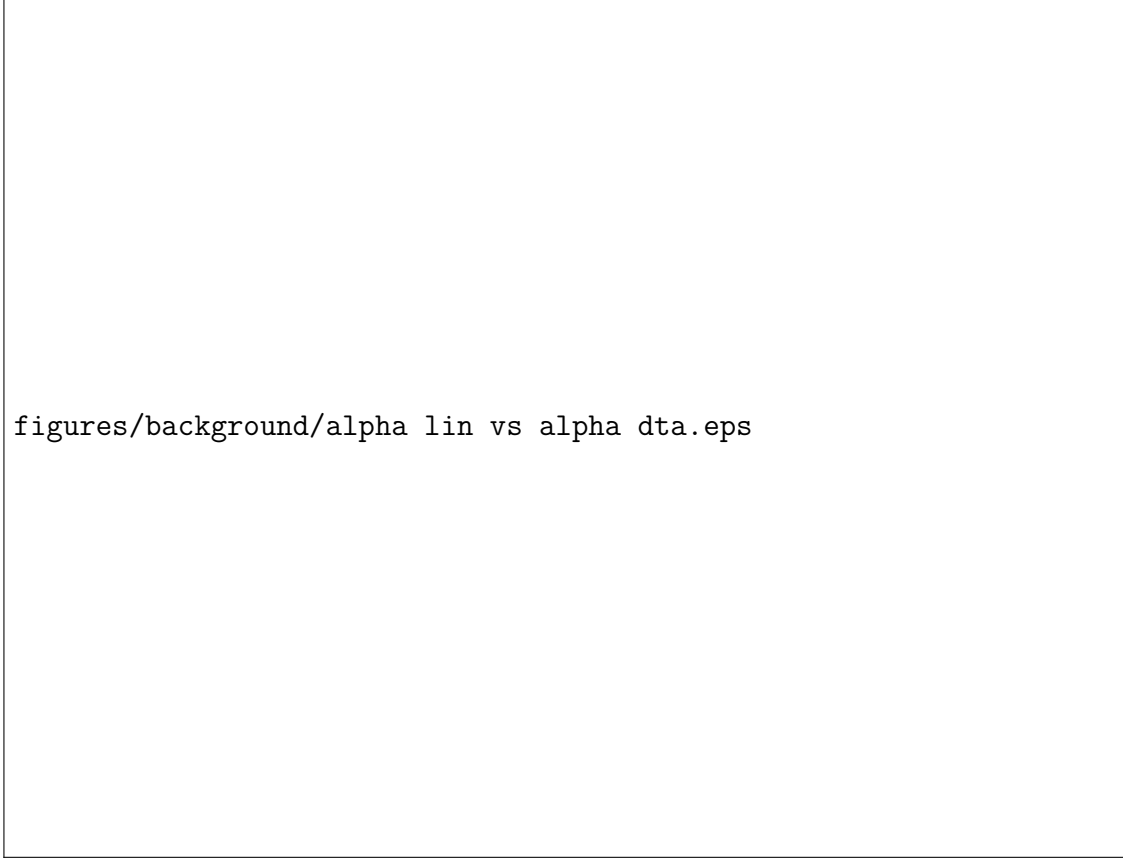


Figure 2.5: Scaling of the linear absorption coefficient (blue) with the normalized photon energy and the derived degenerate two-photon absorption coefficient (orange).

dominant. The scaling function F_{DTA} peaks near $x \sim 1.5$, after which it decreases sharply as the x^{-5} term begins to govern the behavior of the degenerate two photon absorption coefficient. Despite being derived under the parabolic two-band approximation, the scaling of the two-photon absorption coefficient has agreed well with experiment [56].

A similar equation can be derived for the NTA process. Using the definition of the absorption coefficient as in equation (2.54), $\alpha_2(\omega_1 + \omega_2)$ is found to have a form similar to the result in equation (2.59), but with a modified factor f' and with the F_{DTA} function replaced with

$$F_{\text{NTA}}(x_1, x_2) = \frac{(x_1 + x_2 - 1)^{3/2}}{x_1 x_2} \left(\frac{1}{x_1} + \frac{1}{x_2} \right)^3 \quad (2.61)$$

where $x_1 = \hbar\omega_1/E_g$ and $x_2 = \hbar\omega_2/E_g$. The scaling functions F in Eqs.(2.60) and (2.61)

are intuitively powerful results, as they dictate the dispersion of the two photon absorption coefficient admitted by the band structure of the semiconductor. While the analysis here directly considers the nonlinear absorption coefficient terms of power absorbed by the material, a similar F function can be obtained from observing the generation of photoelectrons N_c in the material through the loss of photon numbers N_1 and N_2 [2]:

$$\frac{dN_c}{dz} = \frac{K\sqrt{E_p}N_1N_2}{n_1n_2\tau\pi w_0^2E_g^2}F_{\text{NTA}}^{\text{tot}} \quad (2.62)$$

where K is a material-independent constant, $\sqrt{E_p}$ is the Kane energy parameter, n_1 and n_2 are the refractive indices, $\hbar\omega_i$ are the photon energies, τ is the interaction time of the beams, and πw_0^2 is the illumination area. In this formulation, the scaling function $F_{\text{NTA}}^{\text{tot}}$ is found as:

$$\begin{aligned} F_{\text{NTA}}^{\text{tot}} &= x_2F_{\text{NTA}}(x_1, x_2) + x_1F_{\text{NTA}}(x_2, x_1) \\ &= \frac{(x_1 + x_2 - 1)^{3/2}}{2^6x_1^3x_2^3}(x_1 + x_2)^2 \end{aligned} \quad (2.63)$$

Where x_1 and x_2 are the normalized photon energies given above. Notable in both analyses, *degenerate* two-photon absorption is actually a saddle point in the dispersion curve, visualized in Figure 2.6. For increasingly nondegenerate input photons, this can offer an enormous increase in two-photon absorption efficiency. Additionally, the rate expressions in Eq. (2.46) and (2.63) dictate that the nondegenerate material response is linear with respect to each input photon number. This offers the opportunity to allow photodetectors fabricated from large gap semiconductors to produce a *linear* response to a sub-gap optical signal in the presence of an additional gating beam through a *nonlinear* optical response.



Figure 2.6: Plot of scaling function $F_{\text{NTA}}^{\text{tot}}$ defined through photoelectron generation in Eq. 2.63.

Chapter 3

Dispersion of the Two-Photon Absorption Coefficient in Silicon

3.1 Introduction

The perturbative approach discussed in the previous chapter demonstrated its success in producing expressions that generally predict the energy scaling of the two-photon absorption (TPA) coefficient in *direct* bandgap materials, including the expected enhancement of the TPA effect in the case of extremely non-degenerate photon energies. However, this analysis does not effectively describe *indirect* gap materials, where the photon does not have enough momentum to complete the transition alone, and an additional interaction with a lattice phonon is necessary. As the “scaling laws” arose from approximations made to the momentum matrix elements, it was assumed the same general intuition would hold for the initial NTA imaging experiments using the indirect gap semiconductor silicon discussed in the next chapter.

Here, we recognized the need for a more thorough understanding of indirect two-photon tran-

sitions. Current descriptions have so far relied heavily on the models developed for direct gap transitions. For instance, to account for the interaction vertex with lattice phonons, higher order perturbative expansions of stationary [63, 64] or dressed states [65] have been developed to derive expressions for the nonlinear absorption coefficient. Although such models reproduce the general behaviour of measured two-photon absorption coefficients, quantitative matching between experiment and theory has proven more challenging. The perturbative approach, while flexible with respect to band structure, do not incorporate dephasing mechanisms explicitly, and extra care must be taken to account for material anisotropy. [66] Recently, Faryadraz et al. obtained a semi-empirical scaling law for NTA coefficients, which was compared with experimental data [67]. While semi-empirical models can be useful for gaining mechanistic insights, a more complete theory of two-photon absorption in indirect bandgap materials is needed to quantitatively predict the scaling of 2PA coefficients over a wide range of the energy ratio $\hbar\omega_2/\hbar\omega_1$.

Together with the Technical University of Bydgoszcz, Poland, we sought to address this need. This chapter offers a theoretical description of the two-photon absorption process in silicon through the application of the real density matrix approach (RDMA). This approach has been successfully used by our collaborators for describing the linear and nonlinear optical properties of semiconductors in terms of Rydberg excitons for the case excitation with a single frequency [68, 69]. The RDMA method allows the use of a small number of well-known parameters (e.g., effective masses, gap energy, dielectric constant) to derive expressions for the optical response of the material. We adapt the RDMA for the case of two-photon excitation in semiconductors, extending it for the case of silicon to include both excitonic and continuum states, as well as lattice phonons for momentum matching. Using this approach, we derive analytical expressions for the two-photon coefficient while including dephasing times and anisotropy of the material under study. We compare the energy scaling of the predicted NTA coefficient with published experimental data, supplemented with new experimental data, and demonstrate excellent quantitative agreement over a broad range of

$\hbar\omega_2/\hbar\omega_1$ dispersion values.

3.2 Theory

3.2.1 Real density matrix approach

The theoretical work presented here was spearheaded by our collaborators, and is reproduced here for completeness. In the RDMA approach the nonlinear response is described by a set of coupled equations for the exciton density represented by the coherent amplitude $Y(\mathbf{r}_1, \mathbf{r}_2)$, the density matrix for the conduction electrons $C(\mathbf{r}_1, \mathbf{r}_2)$, and the density matrix $D(\mathbf{r}_1, \mathbf{r}_2)$ for the holes in the valence band [68]. These matrices are sub-matrices of the following density matrix:

$$\hat{\underline{\underline{\rho}}} = \begin{pmatrix} C & Y^* \\ Y & 1 - D \end{pmatrix} \quad (3.1)$$

The evolution of the system is described by Heisenberg equation for the density matrix $\frac{\delta \hat{\underline{\underline{\rho}}}}{\delta t} = [\hat{\underline{\underline{\rho}}}, \hat{H}]$, supplemented by relaxation terms. We also define the excitonic center-of-mass coordinate:

$$\mathbf{R} = \mathbf{R}_{12} = \frac{m_h \mathbf{r}_1 + m_e \mathbf{r}_2}{m_h + m_e}, \quad (3.2)$$

and $\mathbf{r} = \mathbf{r}_1 - \mathbf{r}_2$ is the electron-hole relative coordinate.

The Hamiltonian consists of two parts:

$$\hat{H} = H_{eh} + H', \quad (3.3)$$

where H_{eh} is the electron-hole Hamiltonian [68], and H' describes the exciton-phonon interaction:

$$H' = a(\mathbf{q}) e^{-i\omega_{ph}t} V_p(\mathbf{q}, \mathbf{r}) + \text{c.c.}, \quad (3.4)$$

where

$$V_p(\mathbf{q}, \mathbf{r}) = \left(\frac{\hbar}{2M\omega_{ph}} \right)^{1/2} \times \sum_{R_a} e^{i\mathbf{q}\mathbf{R}_a} \mathbf{e}_0 \nabla_r V(r - R_a). \quad (3.5)$$

The $a(q)$ is the phonon annihilation operator, $V(\mathbf{r} - \mathbf{R}_a)$ is the potential at the point \mathbf{R}_a , \mathbf{e}_0 is the phonon polarization, ω_{ph} is the phonon frequency and \mathbf{q} is its wave vector.

The constitutive equations for the Y, C and D matrices have the following form:

$$i\hbar\partial_t Y - H Y = -\mathbf{M}\mathbf{E} + \mathbf{E}\mathbf{M}_0 C + \mathbf{E}\mathbf{M}_0 D + i\hbar \left(\frac{\partial Y}{\partial t} \right)_{\text{irrev}}, \quad (3.6)$$

$$i\hbar\partial_t C + H_{ee} C = \mathbf{M}_0 \mathbf{E} (Y - Y^*) + i\hbar \left(\frac{\partial C}{\partial t} \right)_{\text{irrev}}, \quad (3.7)$$

$$i\hbar\partial_t D - H_{hh} D = \mathbf{M}_0 \mathbf{E} (Y - Y^*) + i\hbar \left(\frac{\partial D}{\partial t} \right)_{\text{irrev}}, \quad (3.8)$$

where the smeared-out transition dipole density $\mathbf{M}(\mathbf{r})$ and its integrated strength \mathbf{M}_0 are related to the bilocality of the amplitude Y and describe the quantum coherence between the macroscopic electromagnetic field and the inter-band transitions. The electron-electron and hole-hole interaction Hamiltonians H_{ee} and H_{hh} were defined in reference [68]. In expressions (3.6)-(3.8), the electromagnetic field \mathbf{E} includes two frequencies ω_a and ω_b , and is written as:

$$\mathbf{E} = \mathbf{E}_{0a} \exp(i\mathbf{k}_a \mathbf{R} - i\omega_a t) + \mathbf{E}_{0b} \exp(i\mathbf{k}_b \mathbf{R} - i\omega_b t) + \text{c.c.} \quad (3.9)$$

The terms $(\frac{\partial \dots}{\partial t})_{\text{irrev}}$ describe the dissipation and relaxation processes, and satisfy:

$$\left. \frac{\partial \hat{\rho}}{\partial t} \right|_{\text{irrev}} = - \begin{pmatrix} \frac{1}{T_1}[C(t) - C^{(0)}] & \frac{1}{T_2}[Y^*(t) - Y^{*(0)}] \\ \frac{1}{T_2}[Y(t) - Y^{(0)}] & \frac{1}{T_1}[D(t) - D^{(0)}] \end{pmatrix}$$

where the states with superscript (0) represent the steady state solutions. The times T_1, T_2 describe the characteristic duration of all dephasing processes: electron-electron, electron-phonon, and electron-photon interactions. Here, T_1, T_2 are taken as phenomenological constants.

The excitonic part of the polarization is obtained from:

$$\mathbf{P}(\mathbf{R}, t) = 2 \int d^3r \mathbf{M}^*(\mathbf{r}) \text{Re}\{Y(\mathbf{R}, \mathbf{r}, t)\} = \int d^3r \mathbf{M}^*(\mathbf{r}) [Y(\mathbf{R}, \mathbf{r}, t) + \text{c.c.}]. \quad (3.10)$$

The linear optical properties are calculated by solving the interband equation (3.6), supplemented by the corresponding Maxwell equation, where the polarization (3.10) acts as a source. For computing the nonlinear optical properties we use the entire set of constitutive equations (3.6)-(3.8). Although finding a general solution of the equations is challenging, in special situations a solution can be found. For example, if one assumes that the matrices Y, C and D can be expanded in powers of the electric field \mathbf{E} , an iterative procedure can be used.

In general, solving for Y, C and D in the context of two-photon absorption depends on the relation between the incoming frequencies ω_a, ω_b (and thus energies $\hbar\omega_a, \hbar\omega_b$) and the fundamental gap energy E_g , which enters as a parameter in the electron-hole Hamiltonian.

We consider two relevant cases, to be discussed separately:

1. When $\hbar\omega_a + \hbar\omega_b < 2E_g$, the excitation of discrete excitonic states is possible. Therefore we seek solutions in terms of eigenfunctions and eigenvalues of the electron-hole

Hamiltonian, also taking into account the participation of phonons.

2. In the energy range $\hbar\omega_a + \hbar\omega_b > 2E_g$, we solve the equations (3.13), (3.36) and following equations for the matrices C, D assuming $V_{eh} = 0$ [68], thus entering the energy range represented by continuum states. The solution is obtained in terms of an appropriate Green function.

3.2.2 Discrete states

Our goal is to derive expressions for the NTA absorption coefficients. These can be obtained from the third-order nonlinear susceptibility, which, in turn, can be determined via an iterative procedure within the context of the RDMA. The first step in the iteration consists of solving the equation (3.6), which at this stage takes on the form:

$$i\hbar\partial_t Y^{(1)} - H_{eh}Y^{(1)} = -\mathbf{M}\mathbf{E} + i\hbar \left(\frac{\partial Y^{(1)}}{\partial t} \right)_{\text{irrev}} \quad (3.11)$$

For the irreversible part we assume the simple form:

$$\left(\frac{\partial Y^{(1)}}{\partial t} \right)_{\text{irrev}} = -\frac{1}{T_2} Y \quad (3.12)$$

In the discussion of nonlinear effects we also take into account the non-resonant parts of the amplitude Y . The excitonic density Y will consist of two parts, Y_a, Y_b . Therefore, Eq.(3.11) generates four equations: a pair for an amplitude Y_a : one for $Y_{a-}^{(1)} \propto \exp(-i\omega_a t)$, and the

second for $Y_{a+}^{(1)} \propto \exp(i\omega_a t)$:

$$i\hbar \left(i\omega_a + \frac{1}{T_2} \right) Y_{a+}^{(1)} - H_{eh} Y_{a+}^{(1)} = -\mathbf{M}\mathbf{E}_a^*(\mathbf{R}, t) \quad (3.13)$$

$$i\hbar \left(-i\omega_a + \frac{1}{T_2} \right) Y_{a-}^{(1)} - H_{eh} Y_{a-}^{(1)} = -\mathbf{M}\mathbf{E}_a(\mathbf{R}, t)$$

and similar equations for $Y_{b\pm}^{(1)}$. In the following, we consider only one component of the vectors \mathbf{E} , \mathbf{P} and \mathbf{M} .

For the case of discrete exciton states, the exciton density in the first step is found as:

$$\begin{aligned} Y_{da-}^{(1)} &= E_a(\mathbf{R}, t) \sum_n \frac{c_n \varphi_n(\mathbf{r})}{\hbar(\Omega_n - \omega_a - i/T_{2n})} \\ Y_{da+}^{(1)} &= E_a^*(\mathbf{R}, t) \sum_n \frac{c_n \varphi_n(\mathbf{r})}{\hbar(\Omega_n + \omega_a - i/T_{2n})} \end{aligned} \quad (3.14)$$

and similar expressions for $Y_{db\pm}^{(1)}$. The subscript “d” indicates the case of discrete excitonic states. In equations (3.14), we define:

$$\begin{aligned} c_{n00} &\equiv c_n = \int d^3r M(\mathbf{r}) \varphi_{n00}(\mathbf{r}), \\ \hbar\Omega_{n00} &= \hbar\Omega_n = E_g + E_n(\gamma_a) \\ \varphi_{n\ell m} &= R_{n\ell}(r) Y_{\ell m}(\theta, \phi) \end{aligned} \quad (3.15)$$

where $R_{n\ell}$ are the hydrogen radial functions of an anisotropic Schrödinger equation, $Y_{\ell m}(\theta, \phi)$

are spherical harmonics, $E_{n\ell m}$ the corresponding eigenvalues:

$$E_{n\ell m} = -\frac{\eta_{\ell m}^2(\gamma_a)R^*}{n^2}, \quad n = 1, 2, \dots,$$

$$\ell = 0, 1, 2, \dots, n-1, \quad m = 0, 1, 2, \dots, \ell, \quad (3.16)$$

R^* is the effective excitonic Rydberg energy:

$$R^* = \frac{\mu_{\parallel} e^4}{2(4\pi\epsilon_0\sqrt{\epsilon_{\parallel}\epsilon_z})^2\hbar^2} \quad (3.17)$$

the anisotropy parameter γ_a is defined as:

$$\gamma_a = \frac{\mu_{\parallel}\epsilon_{\parallel}}{\mu_z\epsilon_z}, \quad (3.18)$$

and $\eta_{\ell m}(\gamma_a)$ is given by the following expression:

$$\eta_{\ell m}(\gamma_a) = \int_0^{2\pi} d\phi \int_0^{\pi} \frac{|Y_{\ell m}|^2 \sin\theta d\theta}{\sqrt{\sin^2\theta + \gamma_a \cos^2\theta}} \quad (3.19)$$

At room temperature, given the relatively low binding energy of excitons in Si (15 meV [70]), only the lowest excitonic state is relevant. Thus, one may assume $n = 1, \ell = m = 0$ and a single lifetime $T_{2n,n=1} = T_2$.

The solutions for $Y_{da,b\pm}^{(1)}$ determined above allow the calculation of the linear polarization:

$$\begin{aligned} P^{(1)}(\omega) &= \int d^3r \left[Y_{da-}^{(1)} + Y_{da+}^{(1)*} \right] M^*(\mathbf{r}) + \int d^3r \left[Y_{db-}^{(1)} + Y_{db+}^{(1)*} \right] M^*(\mathbf{r}) \\ &= \frac{E_{0a}}{\hbar} \frac{2|c_1|^2\Omega_1}{\Omega_1^2 - (\omega_a + i/T_2)^2} + \frac{E_{0b}}{\hbar} \frac{2|c_1|^2\Omega_1}{\Omega_1^2 - (\omega_b + i/T_2)^2} \\ &= \epsilon_0\chi_d^{(1)}(\omega_a)E_{0a} + \epsilon_0\chi_d^{(1)}(\omega_b)E_{0b} \end{aligned} \quad (3.20)$$

The susceptibilities defined in equation (3.20) can be expressed in terms of the band parameters and, for energies below the gap, when spatial dispersion is neglected, we obtain:

$$\chi_d^{(1)}(\omega_j) = \epsilon_b \frac{f_1 \Delta_{LT} / R^*}{(E_{T1} - \hbar\omega_j - i\Gamma_1) / R^*} \quad (3.21)$$

where $\Gamma_1 = \hbar/T_2$, and E_T is the energy of the first exciton resonance. The anisotropy-dependent oscillator strength f_1 has the form:

$$f_1 = \frac{\eta_{00}^3 (1 - \eta_0 r_0 / a^*)}{(1 + \eta_{00} r_0 / a^*)^4} \quad (3.22)$$

The above formula is obtained when the dipole density $M(\mathbf{r})$ is assumed in the form:

$$M(\mathbf{r}) = M_0 \frac{1}{\sqrt{4\pi}} \frac{1}{r r_0^2 \gamma_a^{1/2}} e^{-r/r_0} Y_{00}(\theta, \phi), \quad (3.23)$$

where $r_0 = (2\mu E_g / \hbar^2)^{-1/2}$ is the so-called coherence radius. The longitudinal transverse splitting of the ground state is:

$$\frac{\Delta_{LT}}{R^*} = 2 \frac{2\mu_{\parallel}}{\epsilon_0 \epsilon_b \pi a^* \hbar^2} M_0^2 \quad (3.24)$$

and is $f_n \Delta_{LT}$ for the excited states. Treating Δ_{LT} as a known quantity, the above relation determines the dipole matrix element M_0 .

To obtain the nonlinear response, the solutions for $Y_{da,b\pm}^{(1)}$ are inserted as a source term in the conduction band equation (3.7) and the valence band equation (3.8). Note that each of these equations depend on the electromagnetic field. If the irreversible terms are well defined, the equations (3.7,3.8) can be solved, and this second step of the iteration yields expressions for the density matrices C and D . These density matrices can then, in turn, be used as a source term for equation (3.6), which can be solved to obtain expressions for $Y_{da,b\pm}^{(3)}$ in the final step

of the iteration.

Accounting for the presence of phonons, we obtain the nonlinear polarization for the region of discrete states. We separate the polarization related to the emission of a phonon (subscript “em”), and to the absorption of a phonon (subscript “abs”). The emission contribution has the form:

$$P_{d,em}^{(3)}(\omega_a, \omega_b) = P_{da,em}^{(3)} e^{-i\omega_a t} + P_{db,em}^{(3)} e^{-i\omega_b t} \quad (3.25)$$

where the polarization amplitudes are defined by:

$$\begin{aligned} P_{da,em}^{(3)} &= \epsilon_0 \chi_{d,self,em}^{(3)}(\omega_a, \omega_a) |E(\omega_a)|^2 E(\omega_a) + \epsilon_0 \chi_{d,cross,em}^{(3)}(\omega_a, \omega_b) |E(\omega_b)|^2 E(\omega_a), \\ P_{db,em}^{(3)} &= \epsilon_0 \chi_{d,self,em}^{(3)}(\omega_b, \omega_b) |E(\omega_b)|^2 E(\omega_b) + \epsilon_0 \chi_{d,cross,em}^{(3)}(\omega_b, \omega_a) |E(\omega_a)|^2 E(\omega_b), \end{aligned}$$

The nonlinear susceptibilities have the form:

$$\begin{aligned} \chi_{d,self,em}^{(3)}(\omega_j, \omega_j) &= -(n_{ph} + 1) \frac{2M_0^2}{\epsilon_0} \frac{1}{T_2} \left(T_1 + \frac{i\hbar\delta(\omega - 2\omega_j)}{\hbar\omega + i\hbar/T_1} \right) \\ &\times \sum_{\ell} \frac{c_{\ell}(A_{\ell} + B_{\ell})\hbar\Omega_{\ell,em}}{(\hbar\Omega_{\ell,em})^2 - (\hbar\omega_j + i\hbar T_2^{-1})^2} \times \sum_n \frac{c_n \varphi_n(0)}{(\hbar\Omega_{n,em} - \hbar\omega_j)^2 + (\hbar/T_2)^2}, \end{aligned} \quad (3.26)$$

$$\begin{aligned} \chi_{d,cross,em}^{(3)}(\omega_a, \omega_b) &= -(n_{ph} + 1) \frac{2M_0^2}{\epsilon_0} \left(\frac{T_1}{T_2} \right) \\ &\times \sum_{\ell} \frac{c_{\ell}(A_{\ell} + B_{\ell})\hbar\Omega_{\ell,em}}{(\hbar\Omega_{\ell,em})^2 - (\hbar\omega_a + i\hbar T_2^{-1})^2} \times \sum_n \frac{c_n \varphi_n(0)}{(\hbar\Omega_{n,em} - \hbar\omega_b)^2 + (\hbar/T_2)^2} \end{aligned} \quad (3.27)$$

and the additional cross term $\chi_{d,cross,em}^{(3)}(\omega_b, \omega_a)$ is obtained by permuting the frequencies ω_a and ω_b in equation (3.27). The number of available phonons n_{ph} is estimated by the formula:

$$n_{ph} = \frac{1}{|\exp \frac{\hbar\omega_{ph}}{k_B\mathcal{T}} - 1|} \quad (3.28)$$

with k_B is the Boltzmann constant, and \mathcal{T} the temperature. $\hbar\Omega_{n,em,abs}$ are the exciton resonance energies that include the phonon energies $\hbar\omega_{ph}$;

$$\hbar\Omega_{n,em,abs} = E_g + E_n \pm \hbar\omega_{ph} \quad (3.29)$$

where “+” stands for phonon emission and “-” for phonon absorption. As discussed in [71, 72], the phonon density of states contains two local maxima at 20 meV and 60 meV, respectively, with a weighted average of approximately 40 meV. This simplified approach of taking an estimate of the average phonon energy has been used in previous calculations, providing proper fits to experimental data.

The coefficients A_ℓ, B_ℓ in equations (3.26,3.27) are related to the irreversible terms in the equations (3.7,3.8), and have the form:

$$\begin{aligned} A_\ell &= \int d^3r \varphi_\ell(\mathbf{r}) e^{-r^2/2\lambda_{th,e}^2}, \quad \ell = 1, 2, \dots \\ B_\ell &= \int d^3r \varphi_\ell(\mathbf{r}) e^{-r^2/2\lambda_{th,h}^2} \end{aligned} \quad (3.30)$$

where $\lambda_{th,e}, \lambda_{th,h}$ are the so-called thermal lengths for electrons and holes, respectively,

$$\lambda_{th,e} = \left(\frac{\hbar^2}{m_e k_B \mathcal{T}} \right)^{1/2} \quad \lambda_{th,h} = \left(\frac{\hbar^2}{m_h k_B \mathcal{T}} \right)^{1/2}$$

The above expressions are valid when: $\hbar\omega < E_g + \hbar\omega_{ph}$. For $\hbar\omega > E_g + \hbar\omega_{ph}$ one should

replace $n_{ph} + 1$ by:

$$\mathcal{C}(\hbar\omega - E_g - \hbar\omega_{ph})^2(n_{ph} + 1) \quad (3.31)$$

where \mathcal{C} is a constant. [73]

Analogous expressions can be obtained for the susceptibilities related to the phonon absorption:

$$\begin{aligned} \chi_{\text{d, self,abs}}^{(3)}(\omega_j, \omega_j) &= -n_{ph} \frac{2M_0^2}{\epsilon_0} \frac{1}{T_2} \left(T_1 + \frac{i\hbar\delta(\omega - 2\omega_j)}{\hbar\omega + i\hbar/T_1} \right) \\ &\times \sum_{\ell} \frac{c_{\ell}(A_{\ell} + B_{\ell})\hbar\Omega_{\ell,abs}}{(\hbar\Omega_{\ell,abs})^2 - (\hbar\omega_j + i\hbar T_2^{-1})^2} \\ &\times \sum_n \frac{c_n\varphi_n(0)}{(\hbar\Omega_{n,abs} - \hbar\omega_j)^2 + (\hbar/T_2)^2} \end{aligned} \quad (3.32)$$

$$\begin{aligned} \chi_{\text{d, cross,abs}}^{(3)}(\omega_a, \omega_b) &= -n_{ph} \frac{2M_0^2}{\epsilon_0} \left(\frac{T_1}{T_2} \right) \\ &\times \sum_{\ell} \frac{c_{\ell}(A_{\ell} + B_{\ell})\hbar\Omega_{\ell,abs}}{(\hbar\Omega_{\ell,abs})^2 - (\hbar\omega_a + i\hbar T_2^{-1})^2} \\ &\times \sum_n \frac{c_n\varphi_n(0)}{(\hbar\Omega_{n,abs} - \hbar\omega_b)^2 + (\hbar/T_2)^2} \end{aligned} \quad (3.33)$$

plus the additional cross term $\chi_{\text{d, cross,abs}}^{(3)}(\omega_b, \omega_a)$ obtained by permuting the input frequencies in (3.33). The above expressions are valid when $\hbar\omega < E_g - \hbar\omega_{ph}$. Otherwise, n_{ph} should be replaced by:

$$\mathcal{C}(\hbar\omega - E_g + \hbar\omega_{ph})^2 n_{ph} \quad (3.34)$$

In section 3.2.4, we use the expressions for the nonlinear susceptibility above to determine the nonlinear absorption coefficients in silicon.

3.2.3 Continuum states

If $(\hbar\omega - \hbar\omega_{ph}) > E_g$ for the case of phonon emission, or $(\hbar\omega + \hbar\omega_{ph}) > E_g$ for the case of phonon absorption, then there is no generation of bound exciton states, and continuum states constitute the final states instead. In this case, $Y^{(1)}$ is calculated in the first iteration step by setting $V_{eh} = 0$ in the electron-hole Hamiltonian [68], giving rise to equations of the form:

$$\left(E_g \pm \hbar\omega \pm \hbar\omega_{ph} - i\Gamma - \frac{\hbar^2}{2\mu} \nabla^2 \right) Y_{\pm} = \mathbf{M}(\mathbf{r})\mathbf{E} \quad (3.35)$$

Equation (3.35) can be solved by means of the appropriate Green function:

$$Y_{\pm}^{(1)} = \int d^3 r' g_{\pm}(r, r') \mathbf{M}(r', \theta, \phi) \mathbf{E}, \quad (3.36)$$

where

$$g_{\pm}(r, r') = \frac{2\mu}{\hbar^2} \frac{\sinh \kappa_{\pm} r^{<}}{4\pi \kappa_{\pm} r^{< r^{>}}} e^{-\kappa_{\pm} r^{>}} \quad (3.37)$$

$r^{<} = \min(r, r')$ and $r^{>} = \max(r, r')$ and

$$\kappa_{\pm}^2 = \frac{2\mu}{\hbar^2} (E_g \pm \hbar\omega \pm \hbar\omega_{ph} - i\Gamma) \quad (3.38)$$

Assuming a linear polarization and the wave vector \mathbf{E} having a component E_0 in a direction α , simultaneously with the dipole density \mathbf{M} having a component M_0 in the same direction and, for simplicity, using the dipole density of the form:

$$M(\mathbf{r}) = \frac{M_0 \delta(r - r_0)}{4\pi r_0^2} e^{-r/r_0}$$

we obtain:

$$Y_{\pm}^{(1)} = M_0 E_0 g_{\pm}(r, r_0). \quad (3.39)$$

We may again define amplitudes of the form $Y_{ca\pm}^{(1)}, Y_{cb\pm}^{(1)}$ where the subscript “c” now indicates the involvement of continuum states. If, in the case of phonon emission, we encounter $\kappa^2 < 0$, we introduce:

$$\kappa = -i\tilde{\kappa} \quad (3.40)$$

where:

$$\tilde{\kappa}_-^2 = \hbar\omega - \hbar\omega_{ph} - E_g + i\Gamma$$

and, in this case, the Green function takes on the form:

$$g_-(r, r') = \frac{2\mu}{\hbar^2} \frac{\sin \tilde{\kappa}_{\pm} r^<}{4\pi \tilde{\kappa}_{\pm} r^< r^>} e^{i\tilde{\kappa}_{\pm} r^>} \quad (3.41)$$

The linear terms for the case of phonon emission and absorption and input frequency ω_a are found as:

$$\begin{aligned} Y_{ca-,em}^{(1)}(r) &= M_0 E_{0a} g_{a-,em}(r, r_0) \\ Y_{ca-,abs}^{(1)}(r) &= M_0 E_{0a} g_{a-,abs}(r, r_0) \end{aligned} \quad (3.42)$$

with

$$\begin{aligned} g_{a-,em}(r, r_0) &= \frac{2\mu_{\parallel H}}{\hbar^2} \frac{\sin(\tilde{\kappa}_{a-,em} r^<)}{4\pi \tilde{\kappa}_{a-,em} r r_0} e^{i\tilde{\kappa}_{a-,em} r^>}, \\ \tilde{\kappa}_{a-,em}^2 &= \frac{2\mu_{\parallel H}}{\hbar^2} [\hbar\omega_a - (E_g + \hbar\omega_{ph})] + i \frac{2\mu_{\parallel H}}{\hbar^2} \frac{\hbar}{T_2}. \end{aligned}$$

Similar expressions can be obtained for the amplitudes at input frequencies ω_b . The linear amplitudes thus obtained form the source for calculating the C and D matrices, followed by third step to determine $Y_{ca,b\pm}^{(3)}$, similar to the procedure described in section 3.2.2. Once the $Y_{ca,b\pm}^{(3)}$ amplitudes are found, for both the phonon emission and absorption process, we may write the nonlinear cross susceptibility for the continuum states as:

$$\chi_{c,\text{cross}}^{(3)} = \chi_{c,\text{cross,em}}^{(3)}(\omega_a, \omega_b) + \chi_{c,\text{cross,abs}}^{(3)}(\omega_a, \omega_b), \quad (3.43)$$

with

$$\begin{aligned} \chi_{c,\text{cross,em}}^{(3)}(\omega_a, \omega_b) &= -(n_{ph} + 1) \frac{2}{\epsilon_0} \frac{T_1}{\hbar} M_0^4 \left(\frac{2\mu_{\parallel H}}{\hbar^2} \right)^2 \\ &\times \frac{1}{4\pi r_0} \left(\frac{\sin(\tilde{\kappa}_{a-,em} r_0)}{\tilde{\kappa}_{a-,em} r_0} \right)^2 \times [\tilde{\kappa}_{b-,em} r_0 + \tilde{\kappa}_{b-,abs} r_0] (A_e + A_h), \end{aligned} \quad (3.44)$$

$$\begin{aligned} \chi_{c,\text{cross,abs}}^{(3)}(\omega_a, \omega_b) &= -n_{ph} \frac{2}{\epsilon_0} \frac{T_1}{\hbar} M_0^4 \left(\frac{2\mu_{\parallel H}}{\hbar^2} \right)^2 \\ &\times \frac{1}{4\pi r_0} \left(\frac{\sin(\tilde{\kappa}_{a-,abs} r_0)}{\tilde{\kappa}_{a-,abs} r_0} \right)^2 \times [\tilde{\kappa}_{b-,em} r_0 + \tilde{\kappa}_{b-,abs} r_0] (A_e + A_h), \end{aligned} \quad (3.45)$$

where

$$\begin{aligned} \tilde{\kappa}_{j-,em} r_0 &= \left(x_j - \frac{E_g + \hbar\omega_{ph}}{E_g} \right)^{1/2} \\ \tilde{\kappa}_{j-,abs} r_0 &= \left(x_j - \frac{E_g - \hbar\omega_{ph}}{E_g} \right)^{1/2} \end{aligned}$$

Here A_e, A_h correspond to the expressions (3.30), related to the irreversible processes:

$$A_e = A'_e + iA''_e = \int d^3r' g_{a-}(r_0, r') f_{0e}(r') = 4\pi \frac{2\mu_{\parallel}}{\hbar^2} \frac{\sin(\kappa_a - r_0)}{\kappa_a - r_0} \int_{r_0}^{\infty} r dr e^{i\kappa_a - r} e^{-r^2/\lambda_{th,e}^2}$$

with an analogous expression for A_h .

3.2.4 Nonlinear absorption coefficients

The propagation of the field components E_{0a} and E_{0b} in the semiconductor follow from the wave equation with $P^{(3)}$ as a source term, which, after making the well-known slowly varying amplitude approximation, yield the following coupled equations for the field amplitudes:

$$\frac{\partial E_{0a}}{\partial z} = i \frac{\omega_a}{n_a c} \chi_{\text{self}}^{(3)}(\omega_a, \omega_a) |E_{0a}|^2 E_{0a} + i \frac{\omega_a}{n_a c} \chi_{\text{cross}}^{(3)}(\omega_a, \omega_b) |E_{0b}|^2 E_{0a} \quad (3.46)$$

$$\frac{\partial E_{0b}}{\partial z} = i \frac{\omega_b}{n_b c} \chi_{\text{self}}^{(3)}(\omega_b, \omega_b) |E_{0b}|^2 E_{0b} + i \frac{\omega_b}{n_b c} \chi_{\text{cross}}^{(3)}(\omega_b, \omega_a) |E_{0a}|^2 E_{0b} \quad (3.47)$$

From the equations above, the intensities of the input beams can be found as:

$$I_a = 2\epsilon_0 n_a c |E_{0a}|^2$$

$$\frac{\partial I_a}{\partial z} = 2\epsilon_0 n_a c \left[E_{0a}^* \frac{\partial E_{0a}}{\partial z} + E_{0a} \frac{\partial E_{0a}^*}{\partial z} \right] \quad (3.48)$$

Similar expressions are obtained for I_b , resulting in the following set of coupled equations 3.46 - 3.47 we obtain the set of equations:

$$\frac{\partial I_a}{\partial z} = -\alpha_2(\omega_a, \omega_a) I_a^2(z) - \alpha_2(\omega_a, \omega_b) I_a(z) I_b(z) \quad (3.49)$$

$$\frac{\partial I_b}{\partial z} = -\alpha_2(\omega_b, \omega_b) I_b^2(z) - \alpha_2(\omega_b, \omega_a) I_b(z) I_a(z)$$

These equations define the nonlinear absorption coefficients α_2 as:

$$\begin{aligned} \alpha_2(\omega_a, \omega_a) &= \frac{\omega_a}{2\epsilon_0 n_a^2 c^2} \text{Im} \left\{ \chi_{\text{self}}^{(3)}(\omega_a, \omega_a) \right\} \\ \alpha_2(\omega_a, \omega_b) &= \frac{\omega_a}{2\epsilon_0 n_a n_b c^2} \text{Im} \left\{ \chi_{\text{cross}}^{(3),I}(\omega_a, \omega_b) \right\} \end{aligned} \quad (3.50)$$

$$\begin{aligned} \alpha_2(\omega_b, \omega_a) &= \frac{\omega_b}{2\epsilon_0 n_a n_b c^2} \text{Im} \left\{ \chi_{\text{cross}}^{(3),I}(\omega_b, \omega_a) \right\} \\ \alpha_2(\omega_b, \omega_b) &= \frac{\omega_b}{2\epsilon_0 n_b^2 c^2} \text{Im} \left\{ \chi_{\text{self}}^{(3),I}(\omega_b, \omega_b) \right\}, \text{ nonnumber} \end{aligned} \quad (3.51)$$

where $\chi^{(3),I}$ indicates the imaginary part of $\chi^{(3)}$. The refractive indices $n_a = n(\omega_a)$, $n_b = n(\omega_b)$ are defined by the real parts of the linear susceptibility $\chi^{(1)}$, defined as:

$$n_a = \left\{ \left[\epsilon_b \left(1 + \frac{f_1 \Delta_{LT} [\hbar\Omega_{n,em}/E_g - x_a]}{[(\hbar\Omega_{n,em}/E_g) - x_a]^2 + \gamma_2^2} \right) \right] \right\}^{1/2}$$

with analogous formulas for ω_b and the absorptive term $\hbar\Omega_{n,abs}$. Here, f_1 is the oscillator strength (here for the heavy hole exciton), written as:

$$f_{1H} = \frac{\eta_{00H}^3}{[1 + \eta_{00H}(r_{0H}/a_H^*)]^3} \quad (3.52)$$

see Eq. (3.22).

The susceptibilities and, in consequence, the nonlinear absorption coefficients, are composed of 4 components: two corresponding to the contributions of discrete and continuous states, and each of them containing terms related to phonon emission and absorption:

$$\alpha_2(\omega_a, \omega_b) = \alpha_{2d}(\omega_a, \omega_b) + \alpha_{2c}(\omega_a, \omega_b) \quad (3.53)$$

For the discrete states, we only consider the lowest exciton state with $n = 1$, yielding the following form:

$$\begin{aligned} \alpha_{2d}(\omega_a, \omega_b) = & -2x_a \gamma_2 \alpha' \left(\frac{T_1}{T_2} \right) \times \\ & \left\{ \frac{\epsilon_b}{n_a n_b} \frac{n_{ph} + 1}{(\hbar\Omega_{1,em}/E_g - x_b)^2 + \gamma_2^2} \times \frac{\hbar\Omega_{1,em}/E_g}{[(\hbar\Omega_{1,em}/E_g)^2 - x_a^2]^2 + (2\gamma_2 x_a)^2} \right. \\ & \left. + \frac{\epsilon_b}{n_a n_b} \frac{n_{ph}}{(\hbar\Omega_{1,abs}/E_g - x_a)^2 + \gamma_2^2} \times \frac{\hbar\Omega_{1,abs}/E_g}{[(\hbar\Omega_{1,abs}/E_g)^2 - x_b^2]^2 + (2\gamma_2 x_b)^2} \right\} \end{aligned} \quad (3.54)$$

where the constant α' is defined as:

$$\begin{aligned} \alpha'(\omega_a, \omega_b) = & 2 \frac{4E_g}{\epsilon_0 \hbar n_a n_b 2c^2 E_g^3} \frac{2M_0^2}{\epsilon_0} [\varphi_{1H}(0)A_1 + \varphi_{1H}(0)B_1] c_{1H}^2 \\ = & 2 \frac{1}{4} \epsilon_0^2 \epsilon_b^2 \pi^2 a_H^{*6} \Delta_{LTH}^2 \times \frac{4}{\pi \epsilon_0 \hbar n_a n_b c^2 E_g^2} \\ & \times [\varphi_{1H}(0)A_1 + \varphi_{1H}(0)B_1] \left(\frac{\eta_H}{a_H^*} \right)^3 \frac{1}{(1 + \eta_H r_{0H}/a_H^*)^2} \\ = & 2 \frac{\pi \epsilon_b^2 \Delta_{LTH}^2 (\eta_H a_H^*)^3}{E_g^2 \hbar c^2 n_a n_b} \frac{[\varphi_{1H}(0)A_1 + \varphi_{1H}(0)B_1]}{(1 + \eta_H r_{0H}/a_H^*)^2} \end{aligned}$$

The continuum states contribution has the form:

$$\alpha_{2c}(\omega_a, \omega_b) = \alpha_{2c,em}(\omega_a, \omega_b) + \alpha_{2c,abs}(\omega_a, \omega_b), \quad (3.55)$$

where

$$\begin{aligned} \alpha_{2,em}(\omega_a, \omega_b) &= -\frac{4E_g(n_{ph} + 1)}{\epsilon_0 \hbar n_a n_b c^2} M_0^4 \left(\frac{2\mu_{\parallel H}}{\hbar^2} \right)^2 \frac{1}{4\pi r_0} \frac{T_1}{\hbar} \\ &\times x_a \left(\frac{\sin(\tilde{\kappa}_{a-,em} r_0)}{\tilde{\kappa}_{a-,em} r_0} \right)^2 [\tilde{\kappa}_{b-,em} r_0 + \tilde{\kappa}_{b-,abs} r_0] a_H^{*2} \times \frac{A_e'' + A_h''}{a_H^{*2}} \end{aligned} \quad (3.56)$$

$$\begin{aligned} \alpha_{2c,abs}(\omega_a, \omega_b) &= -\frac{4E_g n_{ph}}{\epsilon_0 \hbar n_a n_b c^2} M_0^4 \left(\frac{2\mu_{\parallel H}}{\hbar^2} \right)^2 \frac{1}{4\pi r_0} \frac{T_1}{\hbar} \\ &\times x_a \left(\frac{\sin(\tilde{\kappa}_{a-,abs} r_0)}{\tilde{\kappa}_{a-,abs} r_0} \right)^2 [\tilde{\kappa}_{b-,em} r_0 + \tilde{\kappa}_{b-,abs} r_0] a_H^{*2} \times \frac{A_e'' + A_h''}{a_H^{*2}} \end{aligned} \quad (3.57)$$

The solutions obtained in the two regimes of discrete and continuous states are smoothly connected with the use of hyperbolic tangent function. Using the above formula, we have calculated the 2PA coefficient $\alpha_2(\omega, \omega_b)$ as a function of the energies $\hbar\omega_a + \hbar\omega_b$. The band parameters used in the calculations are listed in Tables 3.2 - 3.4.

3.3 Experimental

The experiments outlined here are to both verify the newly presented RDMA expressions and expand upon the limited dataset available for the dispersion of the two photon absorption coefficient in silicon. We are primarily interested in wavelength combinations that

are relevant for the applications presented in the following chapters, where one wavelength is close to but less than the indirect gap, and the other is in the MIR. As both photons are below the gap, a non-collinear transmission pump probe is the preferred method over a two-color open aperture z-scan. Despite being designed expressly for measuring the two photon absorption coefficient in semiconductors, a two-color z-scan is difficult to perform properly. Both the pump and the probe must come to an identical focus, precluding the use of refractive optics. It also requires excellent knowledge of the spatial profile of both beams at each sample measurement position. The main benefit over a simple pump probe experiment chosen above is that the nature of the z-scan measurement allows for the extraction of the two photon absorption coefficient in the presence of dominant linear absorption of the probe beam, which does not coincide with pump and probe combinations used in applications discussed later. The pump probe experiments outlined here are less stringent in the preparation of the beams used, and so are chosen for its relative ease.

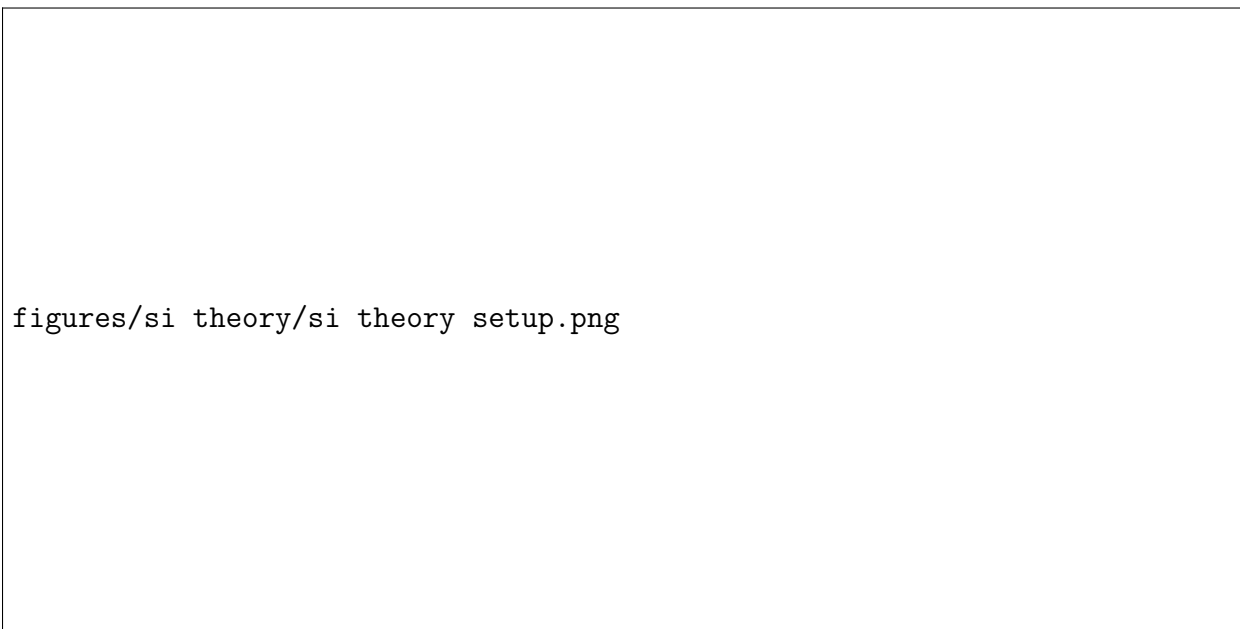


Figure 3.1: Schematic of non-collinear pump probe experiment.

A schematic of the experimental apparatus is in Figure 3.1. We use a 1-kHz amplified femtosecond laser system (Spitfire Ace, Spectra Physics) to seed two optical parametric

amplifiers (OPA, TOPAS-Prime, Light Conversion). One OPA is used as a source of near-infrared (NIR) probe radiation between 1150 nm - 1350 nm (1.08 eV - 0.91 eV), producing pulses in the range of 100-150 fs. The signal and idler pulses from the second OPA system are used to generate MIR pump pulses through the process of difference frequency generation in a nonlinear medium in the range of 2480 nm to 4651 nm (0.5 eV - 0.27 eV), producing 175-265 fs pulses. The MIR pump is modulated using an optical chopper at a frequency of 500 Hz that is synchronized to the laser output (MC2000B, Thorlabs). We use a 280 μm thick [100] silicon wafer (99.999% purity, University Wafer) as the sample target. The MIR and NIR pulses are focused in a non-collinear arrangement on the Si target, using normal incidence for the pump beam and a ~ 20 degree incidence angle for the probe beam, resulting in an internal propagation angle of ~ 6 degrees. Temporal overlap is controlled through an automated translation stage (GTS150, Newport) in the probe arm, producing a cross-correlation of pump induced probe absorption via nondegenerate two-photon absorption. The remaining probe is then attenuated by a 3 OD neutral density filter and detected using a home-built InGaAs photodiode. The modulated change induced by the MIR pump is analyzed by a lock-in amplifier (SR860, Stanford Research Systems). The low irradiance of the probe beam in conjunction with the use of a lock-in amplifier ensures that any degenerate two-photon absorption present is excluded from the measured signal. The pump beam is always the longer wavelength beam, minimizing free carrier absorption induced by the probe via three- or four-photon absorption. The resulting cross-correlation is then used to extract a nonlinear absorption coefficient α_2 as described by Negres et al. [74]

The prescription to obtain the two-photon absorption coefficient seeks to fit an analytical expression for the probe transmittance Q to the cross-correlations obtained. The transmittance is written as an integral over all time and fitting provides a value for the nonlinear

absorption parameter Γ . The expression for Q is given below in Equation 3.58:

$$Q(\tau_d) = \frac{e^{-2\sigma}}{W\sqrt{\pi}} \times \int_{-\infty}^{\infty} \exp \left\{ - \left(\frac{\tau + \tau_d - \rho}{W} \right)^2 \right\} \times \exp \left\{ - \frac{\Gamma\sqrt{\pi}}{\rho} [erf(\tau) - erf(\tau - \rho)] \right\} d\tau \quad (3.58)$$

In the absence of nonlinear absorption, the argument of the second exponential function is zero, causing the integration over the remaining Gaussian function to return $W\sqrt{\pi}$, with W being the ratio of probe to pump temporal widths w and w_p , respectively. In this limit, Q is simply the linear transmittance of the probe beam, where σ is the linear absorption parameter. This parameter was varied very slightly from zero to account for any small changes in the background (approximately one part in ten thousand). The initial transmitted flux was taken with the silicon wafer sample in place, so no linear absorption was observed during the experiment.

When nonlinear absorption occurs, the second exponential is nonzero, giving rise to an additional time dependent transmittance loss characterized by nonlinear absorption induced by the pump. Here, the temporal width of the transient absorption event is given by the two *erf* functions, where one is inverted and shifted by the temporal walk-off parameter ρ , which is the difference in group velocity indices of both beams normalized to the probe beam propagation:

$$\rho = \frac{L}{w_p c} \left[n - \lambda \frac{dn}{d\lambda} \Big|_{\lambda} - \left(n_p - \lambda_p \frac{dn}{d\lambda} \Big|_{\lambda_p} \right) \right] = \frac{L}{w_p c} \Delta n_g \quad (3.59)$$

The refractive index for the pump (n_p) and probe (n) wavelengths were taken from publicly available linear dispersion data on refractiveindex.info [75, 76], and L is the length of the material. The remaining parameter Γ is the target of the fitting process, which is proportional

to the two photon absorption coefficient:

$$\Gamma = L \frac{n}{n_p} I_p \alpha_2 \quad (3.60)$$

Where I_p is the irradiance of the pump beam. To calculate the irradiance and ensure a spatially uniform pump field for the probe to interact with, knife edge scans were done to maintain pump-to-probe beam radius ratios of at least 8:1. The nonlinear least squares fitting process is performed by fitting to the values of Γ and either pump (w) or probe (w_p) temporal width when either is unknown. An example fit overlaid on the data is shown in Figure 3.2. The fitting process was performed iteratively such that the found pulse widths were consistent across all measurements. The pulse width fit parameters were verified through auto- and cross-correlations of two probe pulses and two pump pulses. Autocorrelations of 0.918 eV and 0.992 eV measured through degenerate two photon absorption in a conventional Si photodiode, producing pulse widths of 125 fs and 139 fs, respectively. These measurements were also used to find the widths of two pump pulses of 2480 nm (0.5 eV) and 3295 nm (0.376 eV) via cross correlation in a Si photodiode, found to be 254 fs and 264 fs, respectively. The tabulated data of extracted α_2 values are presented in Table 3.1.

figures/si theory/Figure1.png

Figure 3.2: Exemplary pump probe data and corresponding nonlinear transmittance fit. The photon energies used here are 0.91 eV and 0.376 eV.

| Wavelength (nm) | 2480 | 3295 | 3755 | 4220 |
|-----------------|-------|-------|-------|-------|
| 1150 | 1.099 | 0.71 | 0.823 | 0.955 |
| 1200 | 0.951 | 0.638 | 0.705 | 0.817 |
| 1250 | 0.846 | 0.564 | 0.501 | 0.481 |
| 1350 | 0.634 | 0.452 | 0.385 | 0.307 |

Table 3.1: Experimentally obtained values for α_2 in cm/GW

3.4 Results and discussion

The derived form of α_2 that follows from the RDMA approach contains contributions from the two regimes of exciton production, namely the contributions from discrete states and continuum states, see equation (3.53). Both regimes rely on dipole allowed transitions while considering either the absorption or emission. The discrete regime is visually depicted in Figure 3.3, which highlights the two-dimensional dispersion of α_2 . The analysis recognizes the presence of a single discrete excitonic state below the band edge, corresponding to the creation of a bound state through absorption of a phonon, $\hbar\Omega_{abs}$, which may provide considerable enhancement to the 2PA process. This is manifested by the presence of resonant denominators for the discrete regime, which can be written in simplified form from equation (3.54) as

$$\alpha_{2d}(\omega_a, \omega_b) \propto \frac{1}{(\hbar\Omega_{abs}/E_g - \hbar\omega_b/E_g)^2 + \gamma_2^2} \times \frac{\hbar\Omega_{em}/E_g}{[(\hbar\Omega_{em}/E_g)^2 - (\hbar\omega_a)^2]^2 + (2\gamma_2\hbar\omega_a)^2} \quad (3.61)$$

This single state is the only one considered due to the low binding energy of Si, which precludes the formation of bound excitons with higher principal quantum numbers. When $\hbar\omega_b/\hbar\omega_a$ is detuned away from degeneracy, we observe an increase of α_2 that is as much as $5\times$ the equivalent degenerate response, amplifying the process as it becomes doubly resonant with the lowest discrete state and the edge of the continuum at room temperature. This behavior is evident in the corners of Figure 3.3. While smaller in magnitude, the $\hbar\Omega_{abs}$ state provides additional enhancement when at least one incident photon approaches this energy. An alternate resonance condition exists when both photons are resonant with the discrete exciton level at approximately 95% of the band gap. This is a singly resonant process where the intermediate state is the lowest excitonic state, providing some enhancement to the

two-photon process.

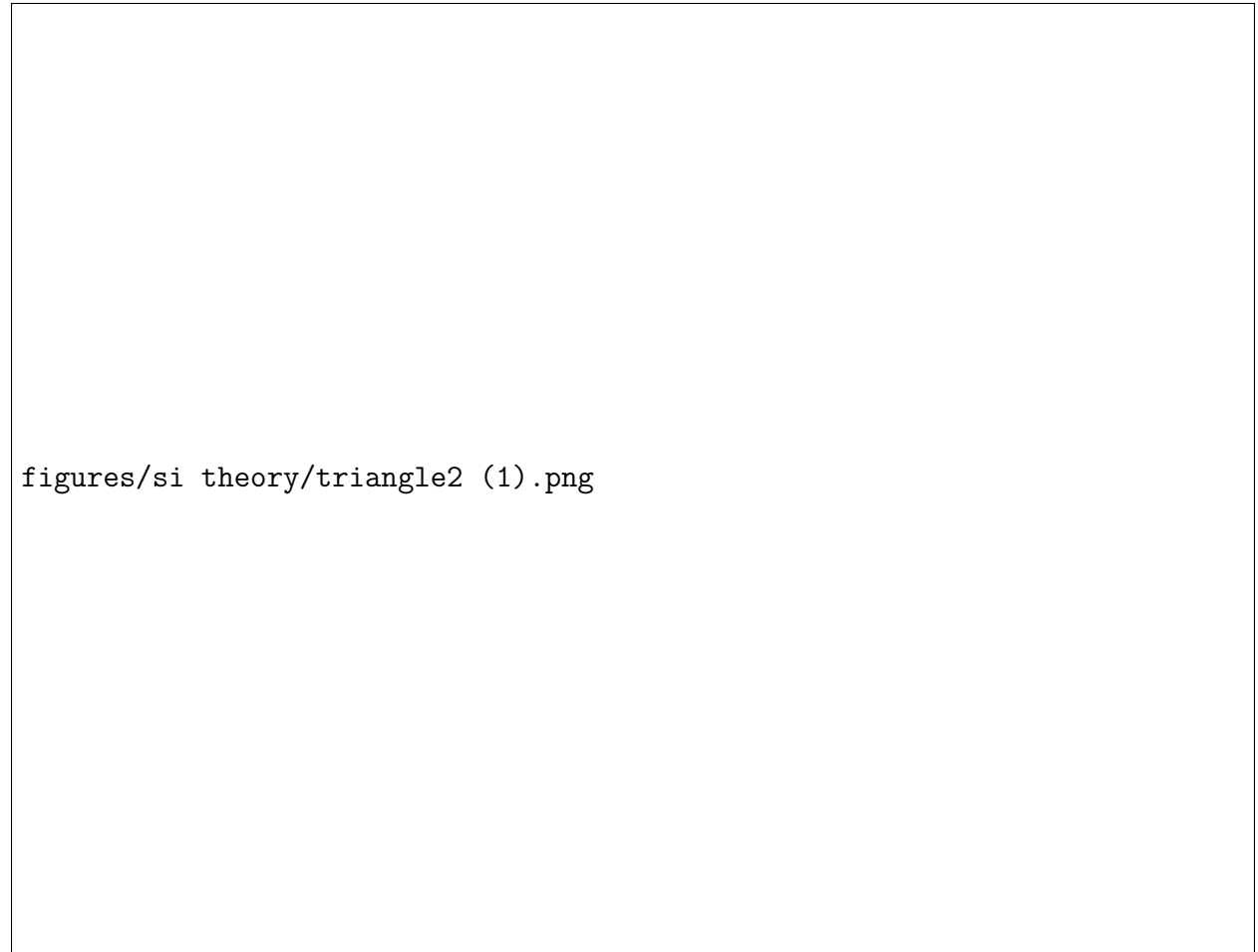



Figure 3.3: Scaling behavior of the two photon absorption coefficient α_2 as a function of normalized photon energy while both photons are below the gap.

If the the energy of the incident photons exceeds the bandgap energy, then the two-photon absorption process proceeds entirely via continuum states. This can be accessed by either phonon absorption or emission, and the nonlinear absorption coefficient has the form as in equation (3.55). Beyond the band edge, the continuum causes α_{2c} to further increase up to the point where the energy of at least one of the photons has enough energy to reach the direct gap of silicon at $E_g = 3.43$ eV. This increase is due to the oscillatory behavior of the linear coherent amplitude of the exciton density $Y^{(1)}$, which contributes to the induced polarization of the medium in order for two-photon absorption to occur.

To validate the performance of the model, we first apply it to explain an experimental data set of the degenerate two-photon (DTA) cross section obtained from an open aperture Z-scan reported in Ref [77]. As can be seen in Figure 3.4(a), α_2 for the DTA process reveals a resonance-like behavior as a function of photon energy. A previous analysis using a model for direct transitions, corrected for the center of mass energy when phonon scattering is involved [78], reproduced the general dependence of α_2 on the photon energy, but it failed to predict the observed resonance structure. The RDMA approach (indicated by the solid line in Figure 3.4), on the other hand, predicts a resonant behavior when the individual photon energy approaches the energy of the discrete exciton state, resulting in a satisfactory description of the data. When the photon energy exceeds the band gap, the role of the bound exciton states decreases and instead the response is largely dictated by continuum states, which results in a slight decrease of α_2 . Note that only the dephasing times in the RDMA analysis are fitting parameters, while all other parameters are obtained from the tabulated values shown Tables 3.2-3.4.




figures/si theory/Figure3.png

Figure 3.4: Scaling of the degenerate two-photon absorption coefficient α_2 as a function of $x = \hbar\omega/E_g$. Squares are obtained from Ref [77] and thick solid line results from the RDMA analysis of two-photon absorption.

We next use the model to describe the energy scaling of the NTA coefficient as measured in Ref [67], which encompasses a normalized photon energy range of $x = \hbar(\omega_a + \omega_b)/2E_g = 1.1 - 2$. In addition, we apply the model to fit a new data set that we have collected for a non-degenerate energy ratio in the $\hbar\omega_a/\hbar\omega_b = 2 - 4$ range, corresponding to pump photon energies of 0.294 eV–0.5 eV and probe energies of 0.91 eV–1.08 eV. Both data sets, shown in Figures 3.5 and 3.6, correspond to a normalized equivalent energy range of $x = 0.55 - 0.8$, but have different levels of non-degeneracy, thus complementing each other. The theoretical predictions for α_2 are in good agreement with both experimental data sets. The most

notable feature in the normalized photon energy curve is the appearance of a peak, which the model attributes to the presence of the bound exciton resonance. The position of this peak shifts in accordance with the energy tuning of the lower energy pump photon, and its magnitude is largely dictated by the damping terms in the resonant denominators of α_{2d} . However, this resonant behavior is significantly different from what is reported in [67], where the theoretical predictions made anticipate a quasi-linear scaling of α_2 as a function of the normalized photon energy. Future work may include performing NTA experiments to verify the behavior of α_2 and the influence of continuum states above the band edge, such as can be obtained with a two-color Z-scan.




figures/si theory/Figure4.png

Figure 3.5: Scaling of the non-degenerate two-photon absorption coefficient α_2 as a function of the normalized equivalent energy. Experimental data points are obtained from Ref [67] and thick solid lines represent the results from the RDMA analysis. Different colors correspond to different non-degeneracy energy ratios $\hbar\omega_a/\hbar\omega_b$.

This work is a significant departure from the conventional understanding of the two-photon absorption process in semiconductors. Previous methods have described the 2PA absorption process in terms of transition rate matrix elements based on electron band states, where significantly nondegenerate photons become resonant with the interband transition and an intraband transition simultaneously. Within the framework of the RDMA, the defining feature of the absorption process is the ability to produce either bound or free excitons within the material. Tracking the formation of excitons allows the RDMA to yield general expres-

sions for semiconducting materials with low binding energies, i.e. only the lowest discrete state needs to be considered. These results are analytical in that there is no parametrization done to provide free variables for fitting. The only variability results from loosely determined material parameters, namely the relaxation times T_1 and T_2 .

It is possible to apply this analysis to direct gap two-photon transitions as well, which omits the involvement of phonon absorption or emission processes in the final equations. The RDMA also accounts for the physical realities of material anisotropy and relaxation mechanisms that are often added phenomenologically elsewhere. Bolstered by the excellent agreement between theory and experiment over a wide range of photon energies and non-degeneracy ratios, we believe that the current description provides a deeper insight into two-photon absorption process in semiconducting materials.



figures/si theory/Figure5.png

Figure 3.6: Scaling of the non-degenerate two-photon absorption coefficient α_2 as a function of the normalized equivalent energy. Data points indicate experimental results and thick solid lines represent the results from the RDMA analysis. Different colors correspond to different non-degeneracy energy ratios $\hbar\omega_a/\hbar\omega_b$.

Table 3.2: Band parameter values for Si, masses in free electron mass m_0 , $R_{H,L}^*$ calculated from $(\mu_{H,Ltr}/\epsilon_b^2) \times 13600 \text{ meV}$, $a_{H,L}^*$ calculated from $(1/\mu_{H,Ltr})\epsilon_b \times 0.0529 \text{ nm}$, $m_{e,dos}$ calculated from $6^{2/3} (m_{e,tr}m_{e,lr}m_{e,long})^{1/3}$.

| Parameter | Value | Unit |
|--------------------------------|--------|-------|
| $E_g(4.2\text{K})$ [79] | 1170 | meV |
| $E_g(300\text{K})$ [79] | 1124 | meV |
| $R_H^*(4.2\text{K})$ | 13.61 | meV |
| $R_H^*(300 \text{ K})$ | 15.65 | meV |
| $R_L^*(0 \text{ K})$ | 8.64 | meV |
| $R_L^*(300 \text{ K})$ | 8.35 | meV |
| Δ_{LTH} [80] | 0.1 | meV |
| $m_{e,long}(4.2\text{K})$ | 0.9163 | m_0 |
| $m_{e,long}(300\text{K})$ [79] | 1.09 | m_0 |
| $m_{e,tr}$ | 0.1905 | m_0 |
| $m_{e,dos}(4.2\text{K})$ | 1.04 | m_0 |
| $m_{e,dos}(300\text{K})$ | 1.12 | m_0 |
| m_{hH} [81] | 0.49 | m_0 |
| m_{hL} [81] | 0.16 | m_0 |
| $m_{hH}(4.2\text{K})$ [79] | 0.59 | m_0 |
| $m_{hH}(300\text{K})$ [79] | 1.15 | m_0 |
| $\mu_{H,long}(4.2\text{K})$ | 0.319 | m_0 |
| $\mu_{H,long}(300\text{K})$ | 0.56 | m_0 |
| $\mu_{H,tr}(4.2\text{K})$ | 0.137 | m_0 |
| $\mu_{H,tr}(300\text{K})$ | 0.163 | m_0 |
| $\mu_{L,long}(4.2\text{K})$ | 0.136 | m_0 |
| $\mu_{L,long}(300\text{K})$ | 0.14 | m_0 |
| $\mu_{L,tr}(4.2\text{K})$ | 0.087 | m_0 |
| $\mu_{L,tr}(300\text{K})$ | 0.087 | m_0 |
| $a_H^*(4.2 \text{ K})$ | 4.52 | nm |
| $a_H^*(300 \text{ K})$ | 3.86 | nm |
| $a_L^*(4.2 \text{ K})$ | 7.11 | nm |
| $a_L^*(300 \text{ K})$ | 7.235 | nm |
| $r_{0H}(4.2\text{K})$ | 0.487 | nm |
| $r_{0H}(300\text{K})$ | 0.455 | nm |
| $r_{0L}(4.2\text{K})$ | 0.61 | nm |
| $r_{0L}(300\text{K})$ | 0.61 | nm |
| $\epsilon_b(4.2\text{K})$ | 11.7 | |
| $\epsilon_b(300\text{K})$ | 11.9 | |
| T_2 [70] | 0.1 | ns |
| T_1 (fit) | 8 | ns |
| $\hbar\omega_{ph}$ (fit) [72] | 40 | meV |

Table 3.3: Anisotropy parameters for Si, excitonic energies calculated from Eq. (3.19)

| Parameter | Value | Unit | $\eta_{00v} = \eta_v$ |
|----------------------------|-------|------|-----------------------|
| $\gamma_{aH}(4.2\text{K})$ | 0.43 | | 1.13 |
| $ E_{1H} (4.2\text{K})$ | 17.38 | meV | |
| $\gamma_{aH}(300\text{K})$ | 0.29 | | 1.18 |
| $ E_{1H} (300\text{K})$ | 21.75 | meV | |
| $\gamma_{aL}(4.2\text{K})$ | 0.64 | | 1.07 |
| $ E_{1L} (4.2\text{K})$ | 9.94 | meV | |
| $\gamma_{aL}(300\text{K})$ | 0.62 | | 1.078 |
| $ E_{1L} (300\text{K})$ | 9.70 | meV | |

Table 3.4: Thermal electron and hole lengths for Si and expressions $\varphi_{1H}(0)A_{1H}, B_{1H}$ $\varphi_{2H}(0)A_{2H}, B_{2H}$

| Quantity | Value 4.2K | Value 300 K |
|-------------------------|-----------------|------------------|
| $\bar{\lambda}_{eH}$ | 5.09 | 0.675 |
| $\tilde{\lambda}_{hH}$ | 4.70 | 0.42 |
| $\varphi_{1H}(0)A_{1H}$ | 4×1.64 | 4×0.23 |
| $\varphi_{1H}(0)B_{1H}$ | 4×1.57 | 4×0.155 |

Chapter 4

Mid-Infrared Imaging Through Nondegenerate Two-Photon Absorption

4.1 Introduction

Non-degenerate two-photon absorption as a MIR detection method was first demonstrated in 2011. The authors used pulsed fs sources to successfully detect approximately 20 pJ of $5.6 \mu\text{m}$ light using a GaN photodiode under a 390 nm gating pulse [82]. This remarkable result showed that, under the appropriate illumination conditions, the non-degenerate absorption process in a wide bandgap semiconductor can be more efficient than the linear absorption process in a mercury cadmium telluride (MCT) detector for MIR detection. While it is understood that the NTA process in the indirect gap semiconductor Si would be less efficient than the direct gap GaN detector used, its ubiquity as a photodetector substrate would make high speed, high pixel density solutions accessible to MIR radiation if the signals are

reasonably high. This chapter explores MIR detection and spectroscopy using NTA first in a Si photodiode. Then, given the success of these experiments, we demonstrate wide-field chemical imaging through NTA for the first time.

Si is an indirect semiconductor, and its nonlinear absorption coefficient is unfavorably low compared to those of direct bandgap materials. Another limitation of Si is its shallow linear absorption edge, which translates into a spectral response of the camera that displays a tail on the low energy side, extending from 900 nm to well over 1100 nm [83]. The shallow absorption edge profile limits flexible tuning of gate pulse energies due to one-photon absorption, which renders Si detectors incompatible for NTA-based MIR detection at energies below $\sim 900 \text{ cm}^{-1}$. The Urbach tail of direct bandgap semiconductors, on the other hand, generally displays a much steeper profile and would thus enable NTA detection over a more extended MIR tuning range [84]. A careful examination of two-photon absorption efficiencies as well as the practical tuning range for MIR detection identifies the direct gap semiconductor InGaAs as an ideal candidate for NTA applications.

Imaging using NTA is compared with the proof-of-concept demonstration of NTA in Si and subsequent experiments with InGaAs as the camera substrate. Using an InGaAs camera, we achieve MIR imaging with frame rates that are two orders of magnitude faster than shown for Si. We show high-speed imaging with 1 Mpx frames at 100 fps and 40kpx frames at 500 fps using exposure times as low as $60 \mu\text{s}$ per frame.

4.2 Results

4.2.1 MIR detection with a Si photodiode

We first discuss the utility of Si as a MIR NTA detector using picosecond pulses of low peak intensities. In Fig. 4.1, we compare the linear absorption of 9708 cm^{-1} (1030 nm) photons by a standard Si photodiode with that of NTA for a 2952 cm^{-1} (3388 nm) MIR and 6756 cm^{-1} (1480 nm) NIR gate pulse pair. Since the 1030 nm photon energy exceeds the Si bandgap energy ($E_g \sim 1.1\text{eV}$ (1100 nm)), strong one-photon absorption can be expected. Based on this measurement, the estimated responsivity is $R = 0.2\text{ A/W}$, close to the reported response for Si detectors at 1030 nm. In the NTA experiment, the MIR and NIR photon energies add up to the same energy (9708 cm^{-1}) as in the one-photon experiment, and thus, we may expect a response in Si, albeit weaker. The current photon energy ratio is $\omega_{\text{NIR}}/\omega_{\text{MIR}} = 2.2$. The NTA response is shown in orange and is compared with the degenerate two-photon absorption of the gate pulse. As expected, the NTA signal scales linearly with the NIR pulse energy. Note that there is a regime where the NTA is stronger than the degenerate two photon absorption of the gate using a 0.65 nJ MIR pulse at 3388 nm.

We next studied the sensitivity of MIR detection through NTA in Si. In Fig. 4.2, the detected NTA signal is plotted as a function of the MIR pulse energy MIR (at 2952 cm^{-1}) for various energies of the NIR gate pulse. For these experiments, especially at higher NIR peak intensities, the degenerate contribution of the gate pulse has been subtracted using the modulation of the MIR beam and lock-in detection. We observe that the signal scales linearly with the MIR pulse energy for all settings. The minimally detectable MIR picosecond pulse energy is $\sim 200\text{ fJ}$ using rather modest NIR peak intensities. In the work mentioned above with a direct large-bandgap GaN detector, a detection limit of 100 pJ was reported using femtosecond pulses and a photon energy ratio > 10 [82]. Here, we observe higher detection sensitivities in Si while using picosecond pulses and a much lower photon energy

ratio. Such high detection sensitivities are remarkable and are due in part to the favourable pulse repetition rate (76 MHz) used in the current experiment, offering much better sampling than the kHz pulse repetition rates used previously. The strategy used here offers superior sensitivity, detecting 4 orders of magnitude smaller MIR peak intensities of 20 W/cm^2 (with 0.09 MW/cm^2 at 1480 nm gate pulse) versus 0.2 MW/cm^2 (with 1.9 GW/cm^2 at 390 nm gate pulse), as previously reported [82]. Given that the enhancement scales with the photon energy ratio, we may expect even greater sensitivities for experiments with higher gate photon energies and lower MIR photon energies, with a projected detection floor as low as a few tens of femtojoules (1 W/cm^2).

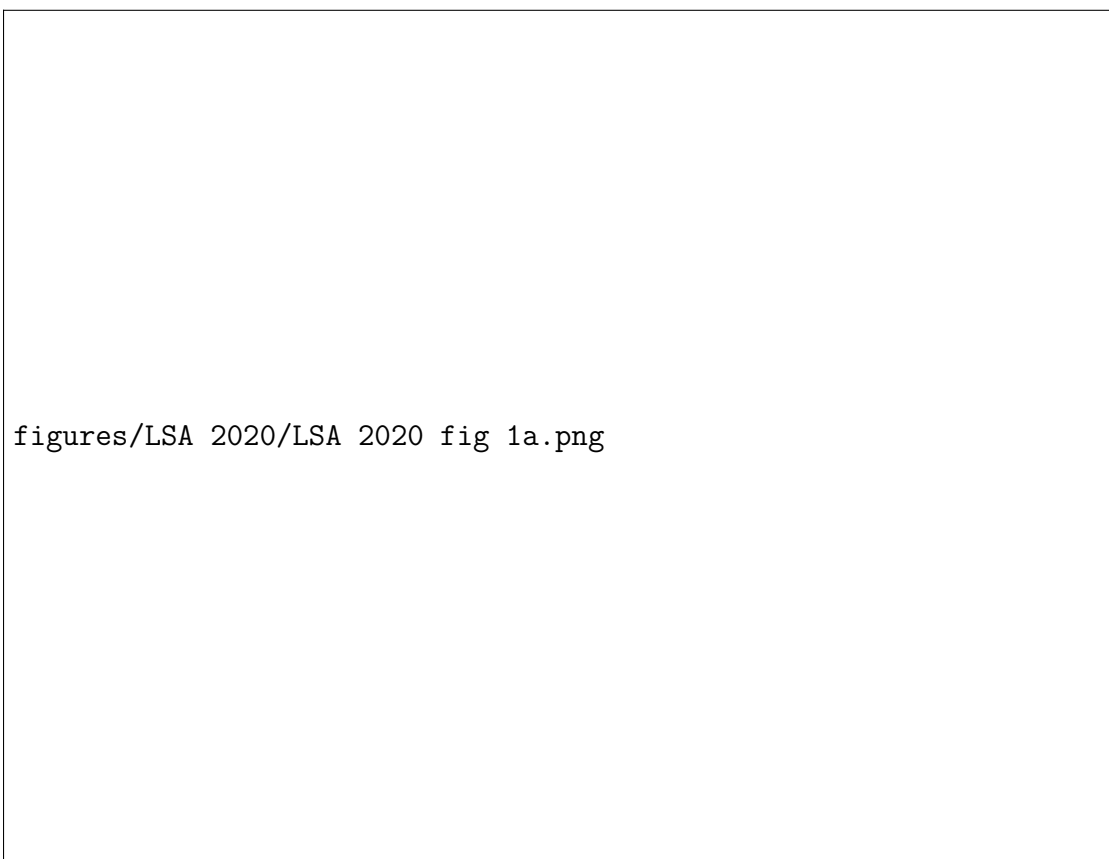


Figure 4.1: Linear absorption (blue) as a function of the pulse energy at 1030 nm, non-degenerate two-photon absorption (orange) as a function of the NIR gate pulse energy at 1480 nm and degenerate two-photon absorption (purple) as a function of the gate pulse energy at 1480 nm. For the non-degenerate curve, the MIR pulse energy at 3388 nm was set to 0.65 nJ. Inset: proposed scheme of photon absorption in Si.

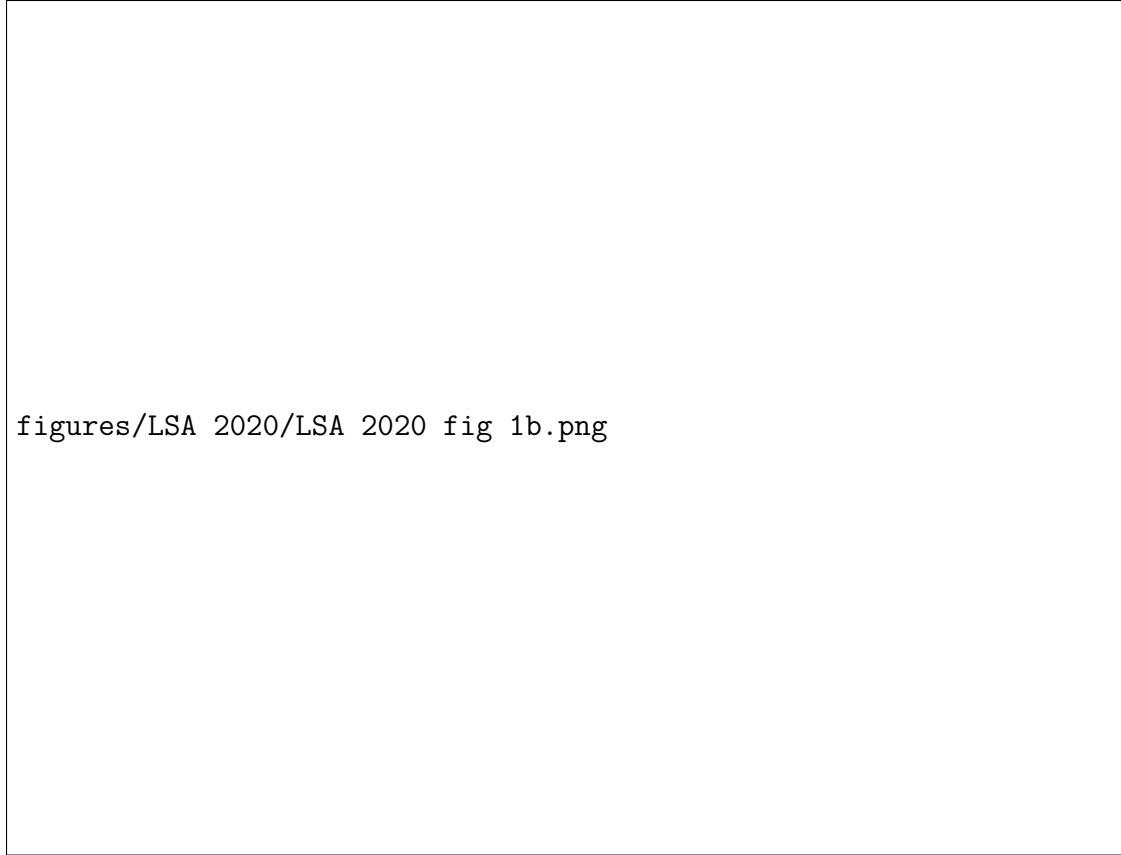


Figure 4.2: Full dynamic range for MIR detection with a detection floor of 200 fJ picosecond pulse energy for given detector parameters. 1 V on the y-axis corresponds to $8.2 * 10^4$ photoelectrons generated per pulse.

4.2.2 MIR spectroscopy with a single pixel Si detector

As an example of the utility of MIR detection with a Si photodetector, we perform an MIR absorption spectroscopy experiment on a dimethyl sulfoxide (DMSO) film of a few tens of microns. For this purpose, we spectrally scan the MIR energy in the $2750\text{-}3150\text{ cm}^{-1}$ range and detect the MIR transmission via NTA on a Si photodiode. The spectral resolution is determined by the spectral width of the picosecond pulse ($\sim 5\text{ cm}^{-1}$). For these experiments, the MIR pulse was kept at 15 mW (10 kW/cm^2 peak intensity), while the NIR gate beam was set to 100 mW (66 kW/cm^2). Because the NIR and MIR pulses are parametrically generated by the same source, there is no temporal walk-off on the picosecond timescale

while performing the scan. The resulting DMSO absorption spectrum shows the characteristic lines associated with the symmetric and asymmetric C–H stretching modes [85], which corroborates the Fourier transform IR (FTIR) absorption spectrum shown in Fig. 4.3.

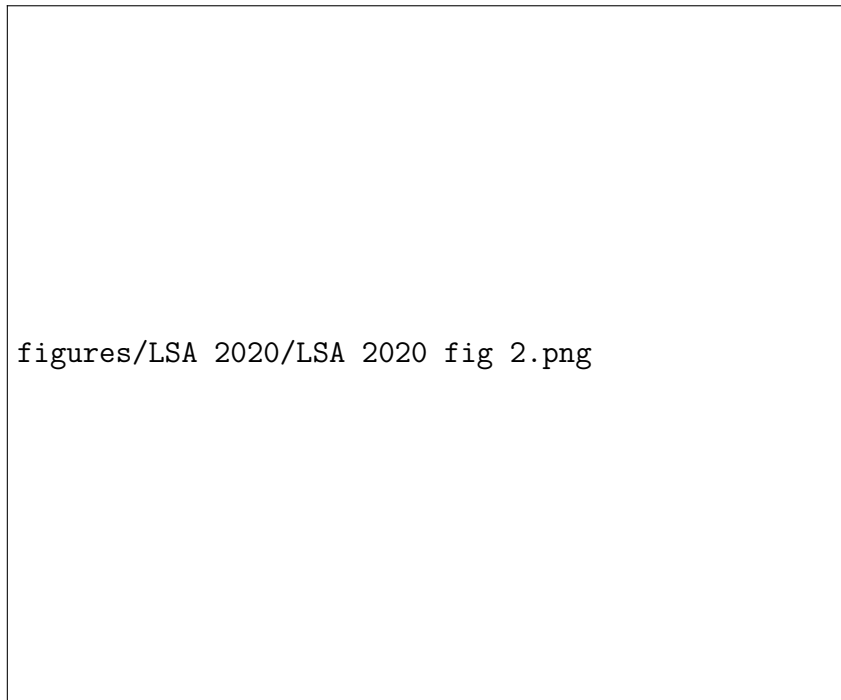


Figure 4.3: Absorption spectrum of dimethyl sulfoxide (DMSO) using non-degenerate two photon detection for measuring the transmitted MIR radiation. Results are in excellent agreement with spectrum measured obtained with conventional ATR-FTIR of bulk DMSO.

4.2.3 MIR imaging through on-chip NTA in a CCD camera

Given the excellent NTA performance of a single pixel Si detector, we next explored the feasibility of MIR imaging through direct on-chip NTA in a Si-based CCD camera. Figure 4.4 provides a schematic representation of the MIR wide-field imaging system based on NTA. The gate and MIR beams are generated by a 4 ps, 76 MHz optical parametric oscillator (OPO) and are expanded to a beam diameter of ~ 3 mm. The MIR arm contains the sample and a 100 mm CaF₂ lens to map the image in a 1:1 fashion onto the CCD sensor. The NIR gate beam spatially and temporally overlaps with the MIR beam with the aid of a dichroic

mirror so that both beams are coincident on the CCD chip. Note that phase matching is not important for NTA, implying that the angle of incidence of the gate beam can be adjusted freely. Here, we use a conventional, Peltier-cooled CCD camera (Clara, Andor, Northern Ireland) featuring $6.45 \times 6.45 \mu\text{m}^2$ pixels in a 1392×1040 array. The current magnification and effective numerical aperture of the imaging lens ($\text{NA} = 0.015$) provides an image with $\sim 100 \mu\text{m}$ resolution, corresponding to ~ 20 pixels on the camera.

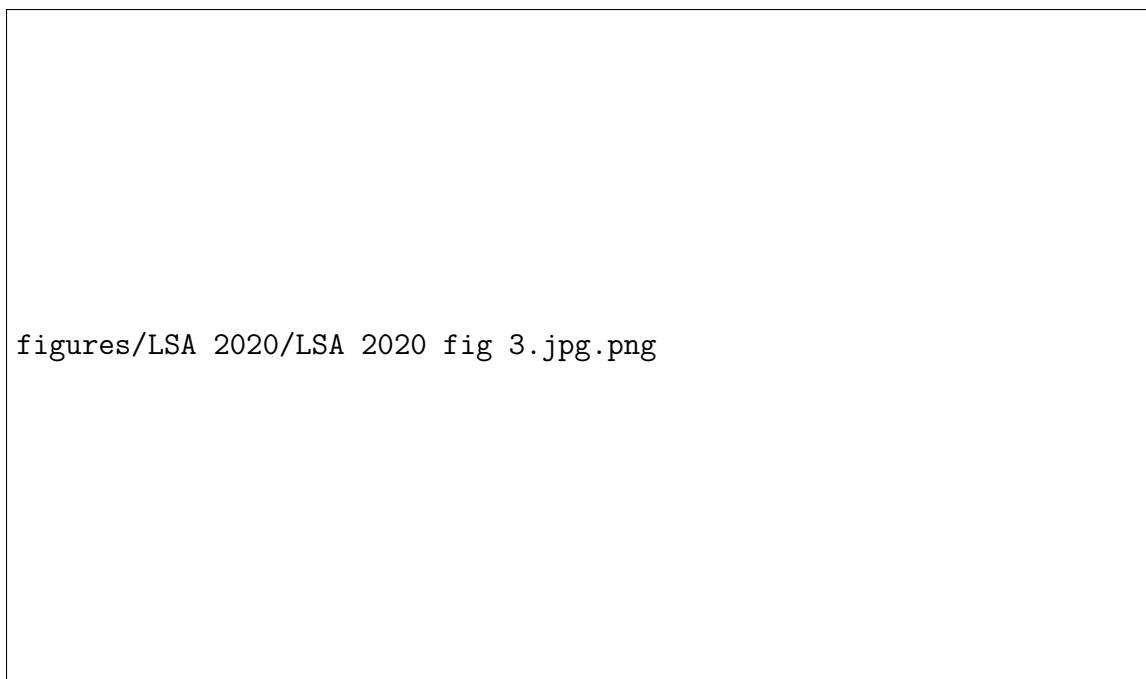


Figure 4.4: Schematic of wide-field MIR imaging system based on non-degenerate two-photon absorption in a Si-based CCD camera.

In Fig. 4.5a, we show the NTA image of the MIR beam projected onto the CCD sensor using a 1 s exposure time. The degenerate background signal has been subtracted to solely reveal the MIR contribution. The background has to be measured only once for a given NIR gate intensity and can be subtracted automatically during imaging, requiring no further postprocessing. Here, we used peak intensities of $\sim 1.5 \text{ kW}/\text{cm}^2$ for the MIR beam and $\sim 1.4 \text{ kW}/\text{cm}^2$ for the NIR gate beam. Under these conditions, each camera pixel only receives pulse energies on the order of a few femtojoules. In Fig. 4.5b, we show the same

MIR beam with a razor blade blocking half of the beam, emphasizing the attained MIR contrast. The fringing at the blade interface is a direct consequence of light diffraction at the step edge.

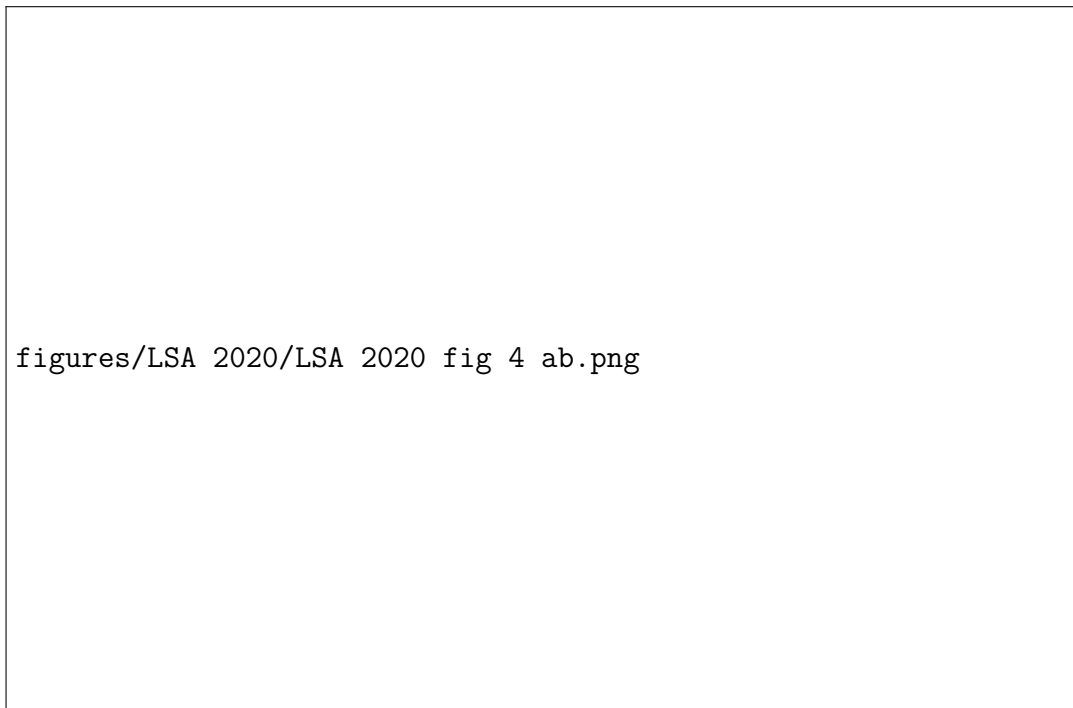


Figure 4.5: (a) Image of MIR (3394 nm) beam profile using a 1478nm NIR gate pulse. (b) Image of razor blade covering half of MIR. The cross section is shown in the top of the panel. Error function analysis shows that the resolution is about 15 pixels ($\sim 100 \mu\text{m}$) under the current conditions.

For the current experimental conditions, we find that the MIR intensity changes on the order of 10^{-2} OD in the image are easily discernible even with exposure times shorter than 1 s. To demonstrate the chemical imaging capabilities, we perform MIR imaging on an $\sim 150 \mu\text{m}$ thick cellulose acetate sheet commonly used as transparencies for laser jet printing. Figure 5a depicts the FTIR spectrum of cellulose acetate in the $2500\text{-}3500 \text{ cm}^{-1}$ range, showing a clear spectral feature due to C–H stretch vibrational modes. In Fig. 4.6b, a strip of the cellulose acetate sheet is imaged at 3078 cm^{-1} , off-resonant with the C–H stretching vibration. Transmission through the sheet is high because of the lack of absorption. To highlight the contrast, the letters “C–H” have been printed with black ink directly onto the

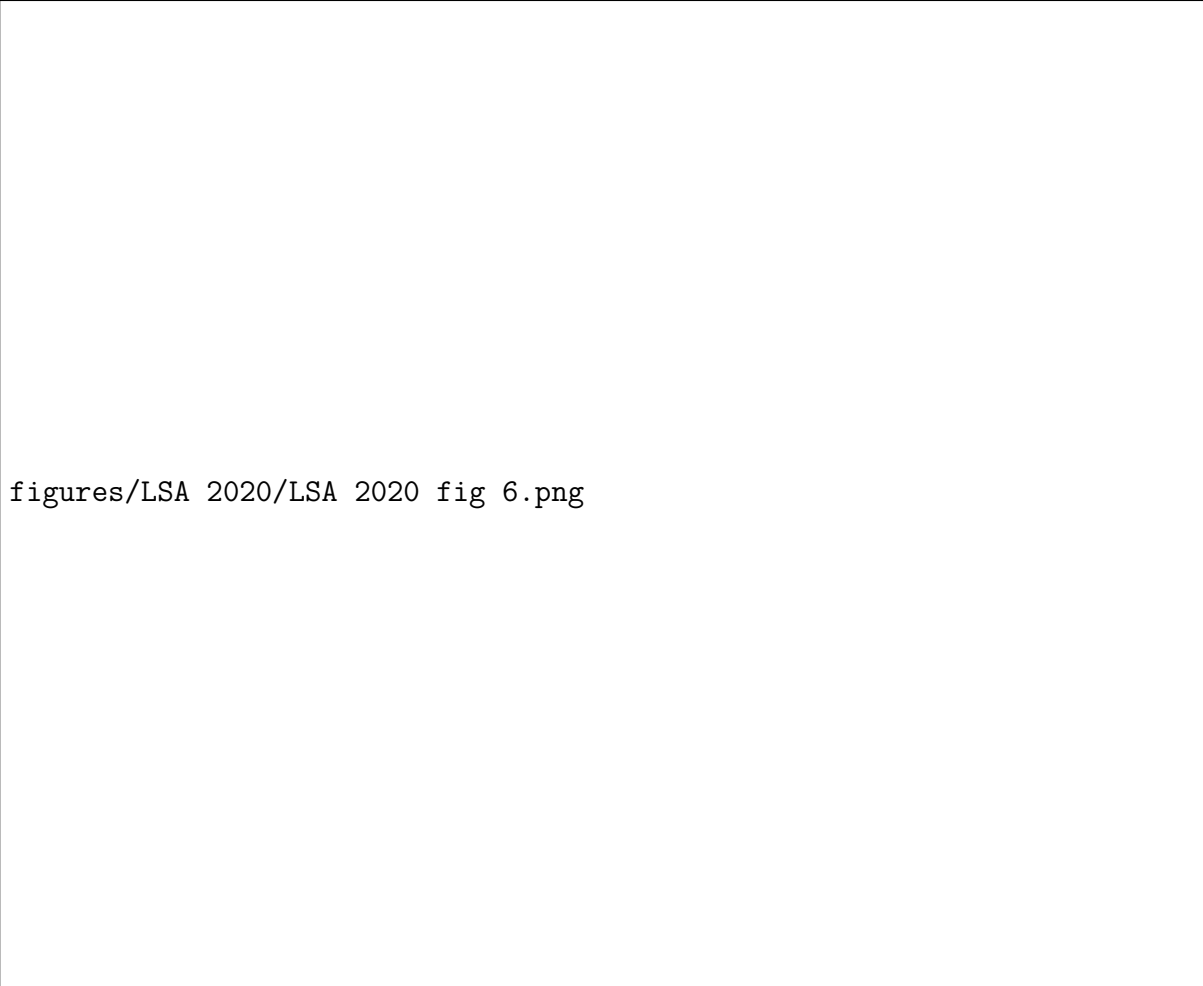
material, providing a mask with limited transmission throughout the 2500–3500 cm^{-1} range. When tuning into the CH-mode resonance (Fig. 4.6b, 3001 cm^{-1}), the transmission is seen to decrease, resulting in lower contrast between the ink and the film. When the MIR is tuned to the maximum of the absorption line (Fig. 4.6d, 2949 cm^{-1}), the limited transmission through the film completely eliminates the ink/film contrast. The relative magnitude of MIR absorption, extracted from the images, maps directly onto the absorption spectrum in Fig. 4.6a, demonstrating quantitative imaging capabilities. The observed contrast is based on a rather modest absorption difference of only 7×10^{-2} OD.



Figure 4.6: Spectral imaging of a 150 μm thick cellulose acetate film. The printed letters serve as a mask that blocks broadband radiation. (a) FTIR transmission spectrum. MIR image taken at (b) an off-resonance energy, (c) the high energy side of the absorption maximum and (d) the absorption maximum.

With the wide-field MIR imaging capabilities thus established, we highlight several examples of chemical imaging of various materials. To suppress contrast due to the refractive index differences, we suspended the materials in (vibrationally non-resonant) D_2O to reveal the

true absorption contrast. Figure 6a depicts the interface between D₂O and an $\sim 20 \mu\text{m}$ thick polydimethylsiloxane film, a silicon-based organic polymer commonly used as vacuum grease. The difference between the images taken on and off-resonance with the methyl stretching mode reveals clear chemical contrast. Note that the boundary between the polydimethylsiloxane film and D₂O is evident due to light scattering at the interface. Similarly, in Fig. 4.7b, chemical contrast is evident when tuning on and off the C–H stretching resonance of a $30 \mu\text{m}$ membrane of poly(2,6-dimethylphenylene oxide-co-N-(2,6-dimethylphenylene oxide) aminopyrene), a material of considerable interest as an ion-exchange membrane. Last, we demonstrate MIR imaging of a bee’s wing in Fig. 4.7c, a rather complex natural structure that is rich in chitin. The chitin MIR spectrum in the $2500\text{--}3500 \text{ cm}^{-1}$ range contains overlapping contributions from OH-, NH- and CH-groups, resulting in broad spectral features. The absorption difference between the 3239 and 3081 cm^{-1} vibrational energies is $\Delta\text{OD} = 0.04$, yet the contrast difference is still evident from the NTA MIR image.



figures/LSA 2020/LSA 2020 fig 6.png

Figure 4.7: MIR images of various materials accompanied with corresponding FTIR spectra. The left column shows non-resonant MIR images, whereas the middle column shows MIR images take at an energy that corresponds with a designated absorptive line. The right column displays the FTIR absorption spectra of the sample with on (orange) and off (grey) resonances indicated. (a) interface between D₂O and silicone lubricant. (b) APPPO polymer film. (c) Wing of a common bee. The exposure time for all images is 1 second.

4.2.4 MIR videography of sample dynamics

The signal strength is sufficient for MIR imaging at even faster acquisition rates. Given that the current camera requires an additional 100 ms of readout time per frame, the effective imaging acquisition time was pushed to 5 fps. Under these conditions, we recorded videos of several mechanical and physical processes as well as live microorganisms. First, in Figure

4.8, a time lapse of the real time movement of a printed target on cellulose acetate films is demonstrated, both under vibrational off resonance and on resonance conditions. In the off resonance condition, the printed target can be seen running across the field of view. Tuning the MIR to become resonant with the C-H stretch of the acetate causes a loss in contrast, and the targets can no longer be seen on the acetate.



Figure 4.8: Timelapse of printed cellulose acetate film. Each panel is a frame taken from a live recording at different time points. Top: MIR beam off resonance to C-H absorption (3078 cm^{-1}). Bottom: MIR beam on resonance with C-H stretch (2949 cm^{-1}). The printed characters running are no longer visible due to loss of MIR transmission.

In Figure 4.9, we show another timelapse of NTA-based MIR imaging of live nematodes suspended in a D_2O buffer, recorded at 3381 nm (2958 cm^{-1}). The image contrast is due to absorption by the methyl stretching vibrations of the protein in the digestive tract of the nematode, in addition to refractive effects. The video demonstrates that active, live nematodes can be captured in real time under the MIR illumination conditions used in NTA detection.

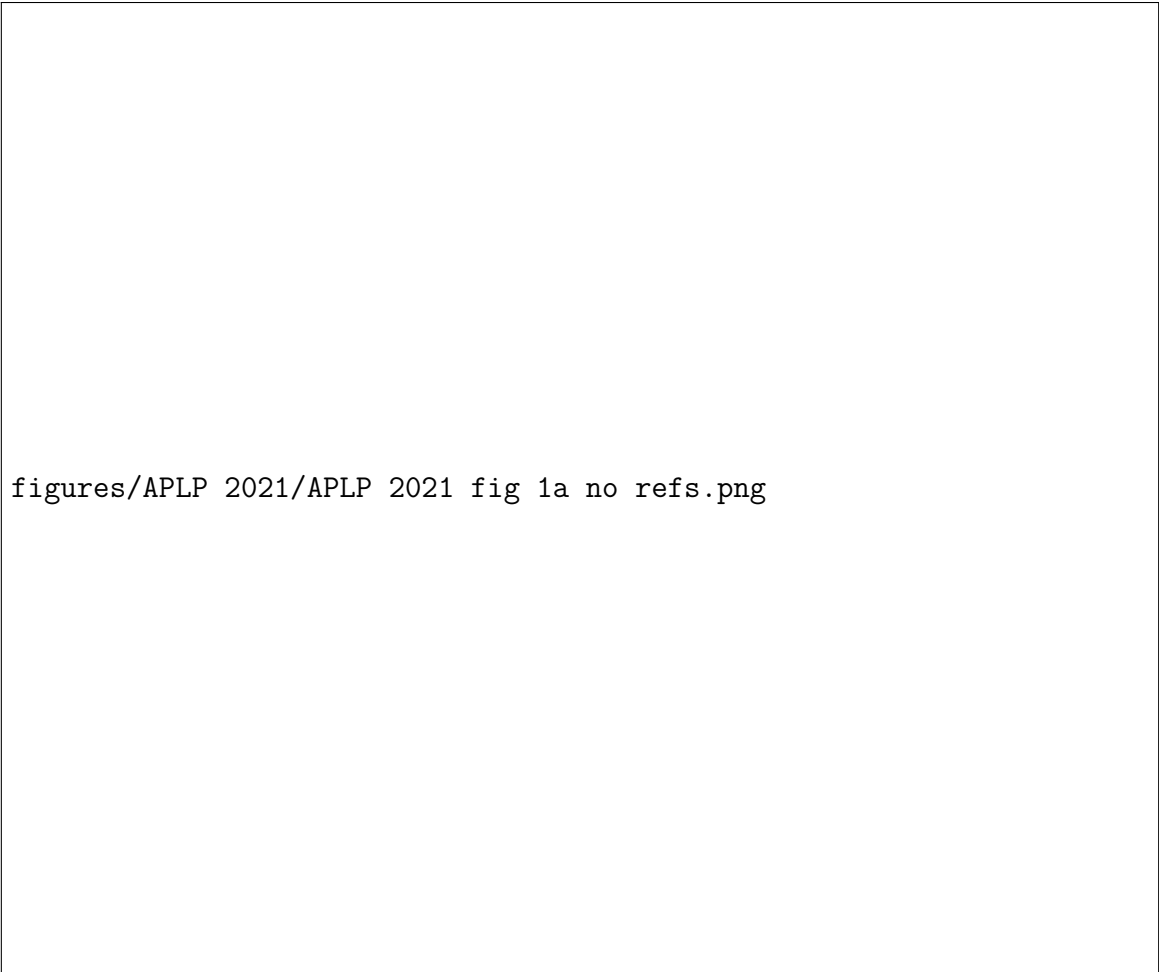
figures/LSA 2020/wormy timelapse.png

Figure 4.9: Timelapse of a live nematode (*C. elegans*) in D₂O buffer. Each panel is a frame taken from a live recording at different time points. MIR beam was tuned to 2950 cm⁻¹, on resonance with the C-H stretching vibrations of protein.

4.3 NTA imaging with InGaAs

4.3.1 Two-Photon absorption coefficient of Si and InGaAs

While the previous chapter sought to study the fundamental physics underlying the dispersion of the two-photon coefficient for Si, and this chapter applied NTA in Si for use as a MIR imaging method, the efficiency of the process is too low to achieve truly high-speed imaging. Experimentally observed DTA values for direct gap semiconductors with comparable bandgap energies are an order of magnitude higher than in Si, as depicted in Figure 4.10. To push the NTA imaging speed and sensitivity beyond what can be achieved with Si cameras, an array with a direct bandgap substrate can be used. In collaboration with Princeton Infrared Technologies, we have explored the ramifications of using an InGaAs camera for this purpose.



figures/APLP 2021/APLP 2021 fig 1a no refs.png

Figure 4.10: Scaling rule of the degenerate two-photon absorption coefficient as a function of semiconductor bandgap. Data for InSb from [86], InGaAs from [87], GaAs and ZnSe from [82], and CdTe, ZnO, ZnS from [56].

Using the established direct gap theory for InGaAs, and the newly presented indirect gap theory for Si, an estimation of the two photon absorption coefficient for the InGaAs material can be made. As the direct bandgap of InGaAs is approximately 0.73 eV, a NIR gate center wavelength of 1900 nm (0.65 eV) was chosen experimentally to limit linear absorption. For the above experiments in Si (1.12 eV), the NIR gate was at 1480 nm (0.84 eV). Using a common MIR signal at 3388 nm (0.37 eV), the anticipated InGaAs NTA coefficient is 343 cm/GW, compared to 3.47 cm/GW in Si, corresponding to an increase of 2 orders of magnitude. This increase was compounded by a change of illumination conditions, where

the light source was changed from a ps optical parametric oscillator (OPO) signal idler pair to two independent fs optical parametric amplifiers (OPA). The fs OPA system provided independent NIR/MIR combinations for improved freedom in center wavelength choice. Additionally, as the two photon process is dependent on irradiance, the use of fs pulses would further increase the efficiency, making NTA with the InGaAs camera even more favorable for MIR imaging.

4.3.2 Faster MIR imaging with InGaAs

Figure 4.11(a) shows an NTA image of the MIR beam at 4250 nm ($\sim 2350 \text{ cm}^{-1}$) on the InGaAs chip. The high optical nonlinearity of the InGaAs material enables efficient NTA, allowing an exposure time of only 60 μs . At such fast exposure times, light contamination from the surrounding is negligible. At the 1 kHz repetition rate of the light source, the inter-pulse separation is 1 ms, which is much longer than the exposure time. Consequently, the signal shown in Fig. 4.11(a) is caused by a single MIR/gate pulse pair. Similarly, for exposure times less than 1 ms, the NTA signal in illuminated frames is derived from single shots that fall within the exposure time window.

| | InGaAs | Si |
|-----------------------------------------------------|----------------------------|---------------------|
| MIR power | 130 μW | 1 mW |
| NIR power | 20 μW | 120 μW |
| Exposure time | 60 μs (1 pulse) | 100 ms (100 pulses) |
| $\hbar\omega_{\text{NIR}}/\hbar\omega_{\text{MIR}}$ | 2 | 3.2 |

Table 4.1: Parameters for comparison of Si and InGaAs in Fig. 4.11.

figures/APLP 2021/APLP 2021 fig 2.jpeg

Figure 4.11: (a) 4250 nm ($\sim 2350 \text{ cm}^{-1}$) single shot detection by an InGaAs camera using 60 μs exposure time. The MIR average power is 130 μW . The inset shows the spatial cross section of the beam profile on the camera chip (orange curve) when both MIR and gate pulses are present. The light blue curve shows the DTA background when only the 1900 nm gate beam is present. (b) 3840 nm ($\sim 2600 \text{ cm}^{-1}$) pulse train detection on a Si CCD camera using 100 ms exposure time. The average power is 1 mW.

For comparison, Fig. 4.11(b) shows an NTA image collected with a Si CCD camera (Clara, Andor Technologies). The average powers of the MIR and gate beams, as well as the exposure time, are adjusted to achieve roughly the same NTA signal level on the Si camera for experimentally relevant photon nondegeneracy ratios. The illumination parameters for this comparison are given in Table 4.1. Accounting for the differences in illumination conditions, optical properties of protective windows, and gain settings, we observe that the InGaAs camera exhibits a ~ 100 times higher detection efficiency than its Si counterpart. These observations are in good agreement with the estimation made above from Equations 2.63 for InGaAs and 3.54 for Si.



figures/APLP 2021/APLP 2021 fig 3.jpeg

Figure 4.12: Chemically selective 2D imaging of cellulose acetate film. A figure is printed on the film with black ink to generate contrast. If tuned to the C-H stretching mode, cellulose acetate becomes less transparent, decreasing the contrast between the clear and inked areas of the film. Exposure time: 1 ms.

To compare with the narrowband ps imaging demonstrated above, chemical imaging of another printed target on a $\sim 110 \mu\text{m}$ thick cellulose acetate sheet is shown in Fig. 4.12. The broad bandwidth of the fs pulses used for imaging with InGaAs still yield good image contrast, but the determination absorption peak position suffers, as underlined by the spectral bandwidth overlaid onto the FTIR spectrum of cellulose acetate depicted in Fig. 4.12(a). The absorption feature in the relevant spectral range corresponds to the same C-H stretching vibrational mode as in Fig. 4.6. In Fig. 4.12(b), the MIR beam is tuned to 3000 cm^{-1} where absorption is significant, reducing the transmission of the MIR light through the material, resulting in poor image contrast. When the MIR beam is tuned off the vibrational resonance, light absorption decreases, enabling more light to pass through the clear part of the film, as illustrated by Figs. 4.12(c) and 4.12(d). This highlights the tradeoff between using fs or ps

illumination, the short pulse time translates to high signals at the cost of spectral resolution.

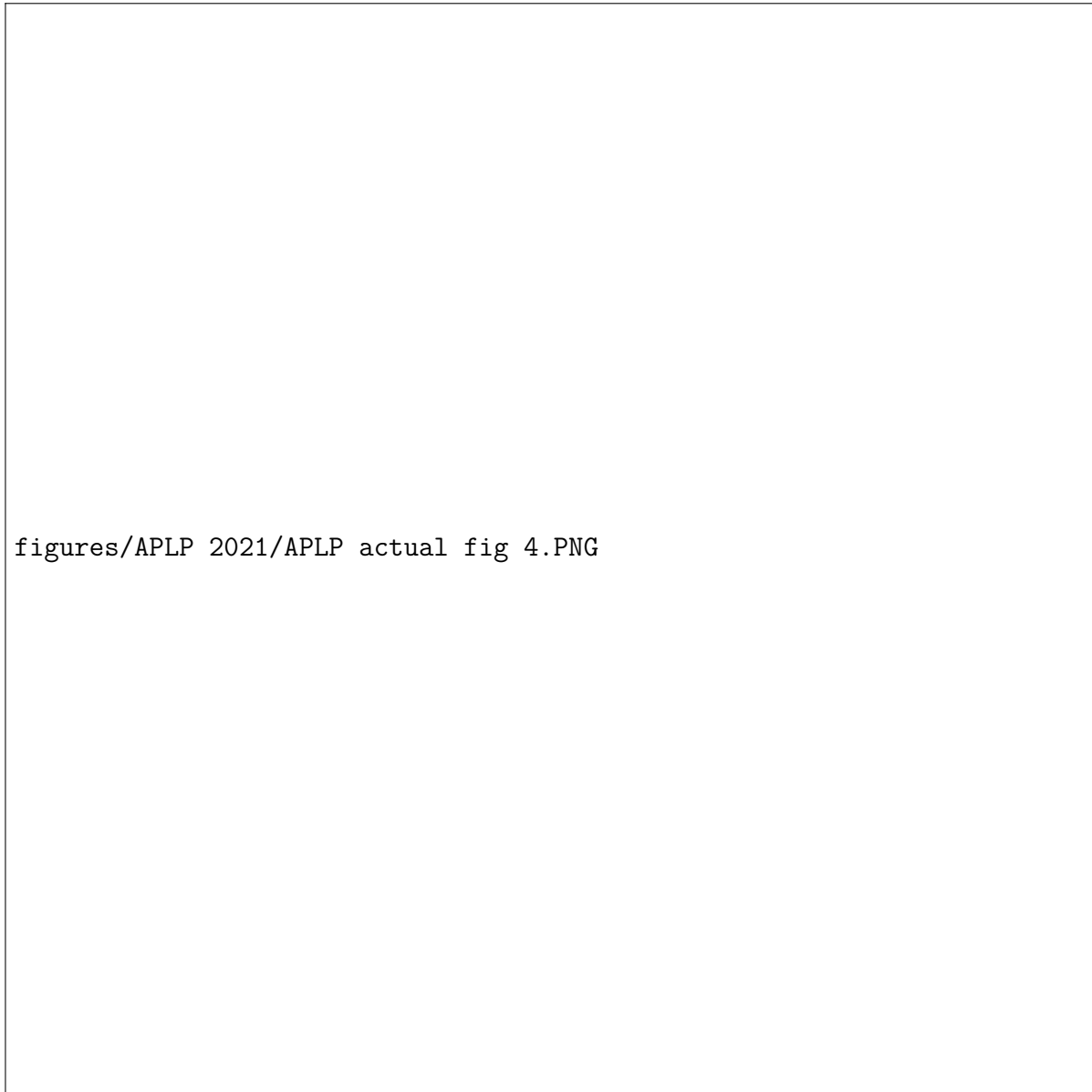


Figure 4.13: Chemically selective 2D imaging of cellulose acetate film. A figure is printed on the film with black ink to generate contrast. If tuned to the C-H stretching mode, cellulose acetate becomes less transparent, decreasing the contrast between the clear and inked areas of the film. Exposure time: 1 ms.

Despite this, the short exposure time enabled by the higher α_{NTA} of InGaAs opens up the possibility of high-speed MIR videography. Figure 4.13 shows the mixing of D₂O with methanol on a coverslip. In these mixing experiments, the active area is visualized in the

transmission geometry at acquisition rates of 500 fps. In the visible range, both liquids are transparent, hence indistinguishable. However, in the MIR spectral region, due to the distinct absorption band of D–O stretching vibrations, D₂O appears much darker at 2600 cm⁻¹ (3850 nm), while methanol remains nearly transparent, as shown in Fig. 4.13. Since mixing and hydrogen bonding between methanol and D₂O molecules is energetically favorable, the process is slightly exothermic [88, 89]. In the early mixing dynamics, the formation of sub-mm bubbles is observed, [90] which can possibly be attributed to the mechanism of solvated gas release (N₂, O₂, CO₂) induced by the local increase in temperature near the interfacial regions [91].

4.4 Discussion

We have shown for the first time that the principle of NTA can be extended to MIR imaging by direct on-chip two-photon absorption in a CCD camera. This has enabled us to acquire images at 100 ms exposure times at femtojoule-level picosecond pulse energies per pixel, experimental conditions that allow wide-field MIR imaging of live, freely suspended organisms at reasonable frame rates. The use of a CCD camera serves as an attractive alternative to standard MIR cameras, such as cryogenically and electronically cooled MCT detectors. NTA enables good quality MIR images without cryogenic cooling, significantly reducing the complexity and cost of the detector. In addition, NTA-enabled imaging benefits from the mature technology of Si-based cameras, offering robust and affordable detection solutions. These advantages are not at the expense of sensitivity, as previous work based on MIR femtosecond pulses has shown that NTA offers comparable sensitivity to (single pixel) MCT detectors [82]. The NTA process can be used to detect MIR radiation over a very broad range. Other than the steepness of the semiconductor’s band edge, there are no fundamental limitations on the detection spectral range [56, 77, 82, 92]. In fact, higher efficiencies of

the NTA process have been demonstrated when tuning towards higher MIR wavelengths near 10 μm , without the necessity of re-alignment, a sensor change or additional data processing.

Following this proof-of-concept work using Si, we have significantly advanced the speed of NTA-based MIR imaging by using an InGaAs camera. Compared to Si detectors, the high nonlinear absorption coefficient of InGaAs sensors increases the efficiency of NTA-induced photocurrents by over two orders of magnitude. We have shown that the higher NTA efficiency readily improves the imaging speed by a factor of at least 100 times. At such imaging rates, 2D and 3D visualization of fast dynamic processes at high pixel numbers, which was hitherto inaccessible for MIR imaging, becomes possible. In particular, using the improved imaging capabilities, we have successfully resolved liquid–liquid mixing dynamics of methanol and D₂O on the millisecond timescale, revealing the formation of gas bubbles within a ~ 100 ms time window.

4.5 Materials and methods

4.5.1 FTIR experiments

Conventional infrared absorption spectra were measured using a Jasco 4700 FTIR spectrometer both in transmission and attenuated total reflection (ATR) geometries. For the ATR experiments, the Jasco ATR-Pro One accessory equipped with a diamond crystal was used. The spectra were averaged over 20 scans and were acquired with a 2 cm^{-1} resolution, close to the resolution of the corresponding picosecond NTA experiments.

4.5.2 Sample handling

Most of the prepared samples were suspended in D₂O to suppress refractive effects and thus revealed pure absorption contrast. DMSO and silicone lubricant (Dow Corning) were obtained from Sigma-Aldrich and were used without further purification. The sample materials, including the APPPO polymer film and clipped bee wings, were immersed in D₂O and confined between hermetically sealed 1-mm thick CaF₂ windows (diameter = 1”). Experiments on cellulose acetate films were performed in air without the use of CaF₂ windows. *C. elegans* were obtained from Carolina Biological. Nematodes were picked up from agar plates with filter paper, immersed in a phosphate buffered saline D₂O solution and placed between two CaF₂ windows spaced by a 50 μ m Teflon spacer.

4.5.3 Non-degenerate two-photon absorption with a Si photodiode

We used a conventional Si photodiode (FDS100, Thorlabs) with the parameters described in Table 4.3. The transparent window in front of the Si material was removed to improve MIR transmission. The experiments were performed in a pump-probe geometry with the setup depicted in Fig. 3, without utilizing a separate imaging lens in the MIR arm. Both MIR and NIR beams were focused onto the Si photodiode by a $f = 100$ mm broadband achromat (Trestle Optics) [93]. The NIR intensity was varied by the combination of a half-wavelength plate and Glan-Thompson polarizer. The MIR intensities were controlled by another half waveplate and a wire-grid polarizer. The polarization of both NIR and MIR optical pulses were linear and parallel and were kept constant throughout the experiments. The MIR beam was modulated at 160 Hz by a mechanical chopper, and the NTA signal contribution was isolated by a lock-in amplifier (SR510, Stanford Instruments).

| | |
|----------------------|--------------------|
| MIR pulse width | 4.1 ps |
| MIR spot size | 250 μm |
| NIR spot size | 300 μm |
| Detector impedance | 1 M Ω |
| Detector chip size | 3.6 \times 3.6mm |
| Reverse bias voltage | 12 V |

Table 4.2: Si photodiode experiment specifications.

4.5.4 Imaging using a Si CCD camera

A Si-based CCD camera (DR-328G-CO2-SIL Clara, Andor) was used with relevant parameters in Table 4.3. The setup is explained in Fig. 3 of the main text. We used a 1:1 imaging system with an $f = 100$ mm CaF₂ lens to project the image onto the CCD camera (Clara, Andor). For live nematode imaging, the imaging system was changed to $2\times$ magnification using a 4f imaging system composed of an $f = 50$ mm CaF₂ lens and an $f = 100$ mm broadband achromat (Trestle Optics) [93].

| | |
|-----------------|------------------------------------------|
| MIR pulse width | 4.1 ps |
| MIR spot size | 3 mm |
| NIR spot size | 3.5 mm |
| CCD pixel size | 6.5 $\mu\text{m} \times 6.5 \mu\text{m}$ |
| CCD active area | 1392 \times 1040 |

Table 4.3: Si CCD experiment specifications.

4.5.5 Imaging using an InGaAs camera

Two femtosecond pulses, a tunable MIR beam and a fixed near-infrared (NIR) gate beam at 1900 nm (5263 cm^{-1}), are spatially overlapped on the InGaAs camera chip (1280MV-Cam, Princeton Infrared Technologies, Inc.). The chip is based on the lattice matched $\text{In}_{0.53}\text{Ga}_{0.47}\text{As}$ alloy, which exhibits a steep bandgap absorption edge around 1700nm (0.73 eV) at room temperature. The camera enables high-speed imaging utilizing the whole chip of 1280×1024 pixels ($12 \mu\text{m}$ pixel pitch) up to 100 fps. Faster voltage readout requires reduction of the region of interest, enabling 500 fps for 200×200 pixel frames. It is important to note that the camera chip is protected by a borosilicate window (thickness 2 mm), which significantly attenuates the MIR radiation ($\text{OD} = 1.25$ at 4200 nm, $\text{OD} > 5$ at 5000 nm). The estimated pulse energies are ~ 200 fJ per pixel for the MIR beam ($130 \mu\text{W}$ average power) and ~ 50 fJ per pixel for the 1900 nm gate beam ($20 \mu\text{W}$ average power). The MIR beam is directed to the sample and scattered light is collected by a 100 mm CaF_2 lens, forming an image of the sample onto the camera in a 1:1 fashion. The current magnification and effective numerical aperture of the imaging lens ($\text{NA} = 0.015$) provides an image with $\sim 100 \mu\text{m}$ resolution, corresponding to ~ 20 pixels on the camera.

Chapter 5

Three-Dimensional Mid-Infrared Imaging through Nondegenerate Two-Photon Absorption

5.1 Introduction

Tomographic imaging refers to a set of optical technologies that enable a three-dimensional reconstruction of an object under study. The most prominent of these is optical coherence tomography (OCT), where broad bandwidth visible or NIR light is reflected off of interfaces, and the returning light is used to obtain the 3D geometry through interferometric gating. OCT systems are well-developed and have achieved widespread clinical use for noninvasive pathology and use in nondestructive quality assurance of products. Seeking to improve upon an already advanced technique, MIR light has proven attractive for tomographic imaging. In particular, compared to visible and near-IR (NIR) radiation, MIR light has a much higher penetration depth in highly scattering materials such as ceramics, paints and printed

electronics, which has led to the development of MIR-based optical coherence tomography (MIR-OCT) techniques [94–102].

Although the unique imaging capabilities of MIR tomographic imaging, and MIR-OCT in particular, address an important need in the characterization of structured materials, its practical implementation is hampered by the same technical hurdles for MIR detection outlined previously. Likewise, the technologies used to circumvent them remain largely the same, simply applied to this new application space. These strategies have been leveraged to improve the performance of MIR-OCT, using either nonlinear upconversion [103] or nonlinear interferometry with entangled photons [104–108]. MIR tomographic images have been recorded at sub-10 μm axial resolution and total acquisition times of minutes per volume.

Despite these important advances in MIR-OCT, the total acquisition time for volumetric images is still long and relies on lateral raster scanning of the beam, rendering current approaches less practical for time-sensitive applications. Furthermore, signal levels appear insufficient for examining weakly reflective interfaces of organic materials, nor do current OCT applications take clear advantage of the spectroscopic sensitivity afforded by MIR light. Here we develop a new, high-speed 3D imaging technique that overcomes these shortcomings in MIR tomographic imaging. Instead of relying on interferometric gating to achieve depth resolution, our approach uses a nonlinear optical gate provided by an additional femtosecond pulse through the process of nondegenerate two-photon absorption (NTA) in a wide bandgap semiconducting photodetector. The principle of NTA has recently been used to acquire tomographic images in the MIR range by single pixel GaN photodiode [109]. To achieve 3D imaging, the object was raster scanned across a focused MIR beam, requiring multiple minutes to build up a volumetric dataset when using lock-in detection, similar to other techniques.

In contrast to 3D imaging with NTA in a photodiode, here it is applied to obtain MIR tomographic images in a massively parallel fashion through the use of a 1.4 Mpx Si CCD

camera and a 1 Mpx InGaAs CMOS camera. Doing so eliminates the need for lateral scanning of the sample altogether by acquiring whole (xy) sample planes in each image. This alone offers an enormous speedup in acquisition time, so much so that despite the relatively weak NTA response from the Si CCD achieved acquisition rates that are up to 2 orders of magnitude higher than MIR-OCT methods and 5000 times faster using the InGaAs CMOS. The first set of experiments using a Si based camera shows that NTA-enabled tomography allows background-free 3D MIR imaging of weakly reflective interfaces of organic materials, objects underneath a 3 mm thick GaAs wafer, and targets hidden under a 190 μm absorbing layer of water. To emphasize the chemical selectivity of MIR tomography, 3D images of polymer structures and protein crystals with spectroscopic contrast based on fundamental vibrational transitions in the 2000 – 3000 cm^{-1} range is also demonstrated. To push 3D NTA imaging to its present limit, single laser shot images are obtained using the InGaAs based camera, providing an entire volumetric data cube within 20 ms of acquisition time.

5.2 Concept and design

Leveraging the short coherence length of the ultrafast pulses participating in NTA imaging, this chapter uses the temporal cross correlation of these pulses to provide micrometer spatial resolution time-of-flight (TOF) measurements captured by the camera. The MIR beam is partially or wholly reflected by samples and selectively upconverted by the NIR gate based on their arrival time at the detector plane. Utilizing MIR light as the information carrying pulse confers two additional benefits; the longer wavelength reduces the amount of scattering losses from obfuscating media and the chemical sensitivity allows the amplitude and timing to convey some information regarding the composition of materials under study. The operating principle and motivating benefits will be discussed briefly here along with the experimental apparatus used to produce 3D MIR images.

The usage of pulsed light in ranging applications is not a new development, where the launching of an optical pulse and timing its return is used to measure the distance between the observer and the object [110]. The distance given by the arrival time of the pulse is a simple expression, $d = 1/2c\tau$, where half the round trip time τ is multiplied by the speed of light [111]. These so-called “direct time-of-flight” imagers usually use a flash from a light emitting diode (LED), producing a pulse of light in the nanosecond range [112]. Assuming the detection electronics are sufficiently fast to resolve the temporal profile of the pulse, the temporal pulse width is the limiting factor in the spatial resolution of this ranging measurement. For a 1 ns pulse, the length of the pulse would be approximately 30 cm. Returning pulses that are separated by less than this distance would overlap in time on the detector, and no certain placement of the distance of the object can be obtained with this simple understanding. Shortening the ranging pulse in time would increase the resolution of this measurement. For instance, an easily achievable 100 fs pulse would in theory offer a spatial resolution of a mere 30 μm .

While TOF measurements with ultrafast pulses have been demonstrated, they typically require more creative solutions to take advantage of these pulses, as detection electronics cannot fully capture their temporal profile directly. Common techniques involve interferometric gating with frequency combs or soliton femtosecond pulses [113, 114]. These achieve very high spatial resolution by interference between a local oscillator gate and the ranged signal, but require tight control over the phase stability between the two pulses. The alternative is to use a simple cross correlation, with the spatial resolution dictated by the convolution of the time gated pulse and the signal pulse [111, 115]. The cross correlation technique lends itself well for use with NTA, as the prerequisite for upconversion of the image carrying MIR beam discussed in the previous chapter is the appropriately timed arrival of the NIR gate pulse. While previous studies using ultrafast light sources primarily concern themselves with the determination of object distances on the order of meters to kilometers with ultrahigh resolution [116], the micrometer scale resolution enables the determination of

object distances in that regime. Here, cross-correlation based measurements such as NTA have not yet been properly utilized, instead favoring OCT-based techniques.

The natural extension of OCT techniques from visible light sources into the MIR has allowed the technique to obtain tomographic measurements of deeper buried interfaces. The increased penetration depth stems from both reduced absorptive and scattering losses in the MIR for certain materials. Most materials have transparency windows in this spectral range despite the presence of fundamental vibrational resonances. The majority of organic materials exhibit little absorption around $4\ \mu\text{m}$, known as the so-called “cell silent window” in biological systems [117, 118]. Inorganic materials like alumina and zirconia, often used in industrial products, lack any meaningful absorptive features from approximately $3\ \mu\text{m}$ to $6\ \mu\text{m}$ [119, 120]. Scattering of light at small particles in the surrounding media translates into optical losses due to the redirection of input light that does not contribute to the reflected signal. Elastic (Rayleigh) scattering at particles is inversely dependent to the fourth power of the wavelength of the input light, providing a large and favorable reduction in scattered intensity for longer wavelength sources [97]. Additionally, Mie scattering grows as the particle size approaches the wavelength of light, which becomes relevant for slightly larger particles under MIR illumination than in the visible [121]. While shifting the light source to the MIR offers solutions to limitations in more traditional visible or NIR based OCT measurements [95], the technique has yet to take full advantage of the spectroscopic utility of mid-infrared radiation.

Spectroscopic OCT (SOCT) does indeed enable extraction of spectroscopic information [122, 123], but its retrieval from the backscattered interferogram is a nontrivial task [124, 125], and has not been applied for use in the MIR. A unique advantage to the method of NTA and its cross-correlation based TOF measurement is that it does not require such numerical post processing. This is enabled by the use of relatively limited bandwidth fs sources and a time reference. For example, if one part of the reflected MIR pulse is temporally located at the first

interface of a sample, then later arrivals can be used to deduce other properties of interest, such as the thickness and refractive index of penetrated media. Furthermore, the use of MIR pulses allows for some understanding of the chemical composition of the sample under study through the sample reflection magnitude by way of its absorption spectrum [126, 127]. In essence, external reflectance spectroscopy combined with the Kramers-Kronig transform reveals the chemical composition of materials present at reflecting interfaces when MIR illumination is used [128–131].

The magnitude of reflecting light from the interface of two media is understood by the well-known Fresnel reflection equations in optics. The power reflection coefficient R dictates the amount of light reflected for either plane perpendicular (s) or parallel (p) polarized light, and is dependent on the complex refractive indices n_1, n_2 of the media sharing an interface:

$$\begin{aligned}
 R_s &= \left| \frac{n_1 \cos \theta_i - n_2 \sqrt{1 - \left(\frac{n_1}{n_2} \sin \theta_i\right)^2}}{n_1 \cos \theta_i + n_2 \sqrt{1 - \left(\frac{n_1}{n_2} \sin \theta_i\right)^2}} \right|^2 \\
 R_p &= \left| \frac{n_1 \sqrt{1 - \left(\frac{n_1}{n_2} \sin \theta_i\right)^2} - n_2 \cos \theta_i}{n_1 \sqrt{1 - \left(\frac{n_1}{n_2} \sin \theta_i\right)^2} + n_2 \cos \theta_i} \right|^2
 \end{aligned} \tag{5.1}$$

Where θ_i is the angle of the incoming ray normal to the surface, and the complex refractive index is defined as:

$$n_j(\omega) = n'_j(\omega) + i\kappa_j(\omega) \tag{5.2}$$

With the extinction coefficient κ being related to the absorption coefficient α of the medium by $\kappa(\omega) = 2\omega\alpha(\omega)/c$. The dispersion of the complex refractive index $n_j(\omega)$ for a given material j implicates the spectroscopic potential of obtaining reflection measurements of samples. If the absorption spectrum is known, the real refractive index can be obtained

by the Kramers-Kronig transformation [132]. With full knowledge of the dispersion of the complex refractive index in hand, it is possible to estimate the power reflection coefficients as a function of wavelength. Conversely, obtaining measurements of R yields information on both real and imaginary portions of the complex refractive index of the medium and can be used to retrieve them separately [130]. The work presented here utilizes this in two ways when the dispersion of the absorption coefficient of a material $\alpha(\omega)$ is known. The Kramers-Kronig transform retrieves the real refractive index $n'(\omega)$, which can be used to determine the thickness of media and the magnitude of the reflected beam R at an interface.

The confluence of concepts discussed here provides the foundation of 3D imaging in the MIR afforded by NTA. The unique opportunity to obtain chemically sensitive reflection data of buried interfaces through the cross correlation of the MIR signal and NIR gate also enables fast acquisition times of 3D volumetric images. Typical measurements by OCT approaches require scanning the sample in the lateral (xy) dimensions to render a 3D volume of the sample under study [133]. With NTA, a wide-field depth measurement can be performed, capturing an entire lateral plane in each image. The use of fs pulses in NTA imaging enables axial optical slicing through temporal gating by the NIR pulse, thus making 3D imaging possible. In this tomographic MIR imaging approach, the depth scan is realized by adjusting the time delay between the MIR and gate pulses at the camera chip. The limiting factor in these proof of concept measurements first demonstrated using a Si-based camera is then the efficiency of the NTA process in the detector substrate and the readout electronics of the relatively slow CCD. Then, an enormous improvement in acquisition times is obtained by replacing the camera substrate with InGaAs as shown in the previous chapter.

The experimental apparatus for 3D imaging with NTA is schematically depicted in Fig. 5.1(a). Two 100 fs pulse trains, a tunable MIR beam, and a fixed 1200 nm (8333 cm^{-1}) NIR gate are spatially overlapped on the Si chip of a CCD camera. The MIR beam path passes onto the sample, and the reflected/scattered light is collected by a 100 mm CaF_2 lens

that projects an image of the sample onto the CCD in a 1:1 fashion (effective NA ~ 0.015). The lateral spatial resolution is characterized as $100 \mu\text{m}$, which is diffraction limited for the effective NA of the imaging lens. An NTA signal is generated in the Si chip whenever the MIR temporally overlaps with the NIR gate pulse. The temporal gate selectively registers MIR light that has traveled a preset path length. This allows depth-dependent detection of reflected/scattered light off the illuminated sample interface. In this wide-field imaging geometry, acquisition of a full 3D scan requires a single axis scan of the time delay.

figures/Optica 2021/Optica-2021-fig-1.png

Figure 5.1: (a) Schematic representation of experimental setup. (b) Beam image on CCD Si chip with MIR (2850 cm^{-1} , 3500 nm) and gate NIR pulse (8333 cm^{-1} , 1200 nm). The inset shows a gate pulse image through DTA. (c) Spatial cross section of the beam image on CCD Si chip with (NTA, orange) and without MIR pulse (DTA, blue line). Inset: temporal cross-correlation of MIR and gate pulse, indicating a 110 fs pulse width (gray line is Gaussian fit)

Figure 5.1(b) shows an image of the MIR beam profile (2850 cm^{-1} , 3500 nm) acquired through NTA. The intensity ratio between the MIR and the gate pulse can be chosen such that the linear dependence dominates over the quadratic term, thus raising the NTA signal relative to the DTA background induced by the gate pulse. This is highlighted in the inset of Fig. 5.1(b), which shows the DTA background signal when the Si chip is exposed only

to the gate pulse. The NTA to DTA background signal is $10 \log_{10}(S_{\text{NTA}}/\sigma_{\text{DTA}}) = 34$ dB, standard deviation $\sim 1\%$, 100 ms per frame at the center of the beam profile, with a ratio up to 40 dB toward the wings of the intensity distribution. While the signal-to background ratio $\text{SBR} = 10 \log_{10}(S_{\text{NTA}}/S_{\text{DTA}})$ is 15 dB, the signal-to-noise ratio determined through the mean power root $\text{SNR} = 20 \log_{10}(S_{\text{NTA}}/\sigma_{\text{DTA}})$ is estimated as 68 dB (80 dB toward the wings) [134]. The high signal-to-background ratio permits imaging without modulation/demodulation techniques, beam profile/intensity precharacterization, or postprocessing of the images.

figures/Optica 2021/Optica 2021 supplemental/OS2.jpg

Figure 5.2: Spectral response of detection system to MIR pulse reflected off a gold mirror (orange dots represent average counts within the center of gaussian beam, blue dots represent constant DTA background of the NIR beam). Average power flux is $4 \text{ mW}/\text{cm}^2$ prior to the camera and the exposure time is 100 ms for all measurements. Horizontal lines represent the estimated Fourier limited spectral bandwidth of the 110 fs MIR pulse.

Contrary to MIR-OCT, where the axial resolution is determined by the spectral width of the light source via interferometric gating, in NTA tomographic imaging the resolution is determined by the temporal cross-correlation of the MIR and gate pulses. The inset of Fig. 5.1(c) shows the cross-correlation of pulses at the camera chip, indicating a correlation pulse width of ~ 110 fs (FWHM) assuming a Gaussian pulse shape. This temporal pulse width corresponds to an axial resolution of $\sim 15 \mu\text{m}$ (FWHM) (5.3). This axial resolution is much

higher than the resolution set by the Rayleigh range of the imaging system for the MIR beam ($NA = 0.015, z_R > 3\text{mm}$), and it is comparable to the confocal resolution offered by a $NA > 0.65$ lens.

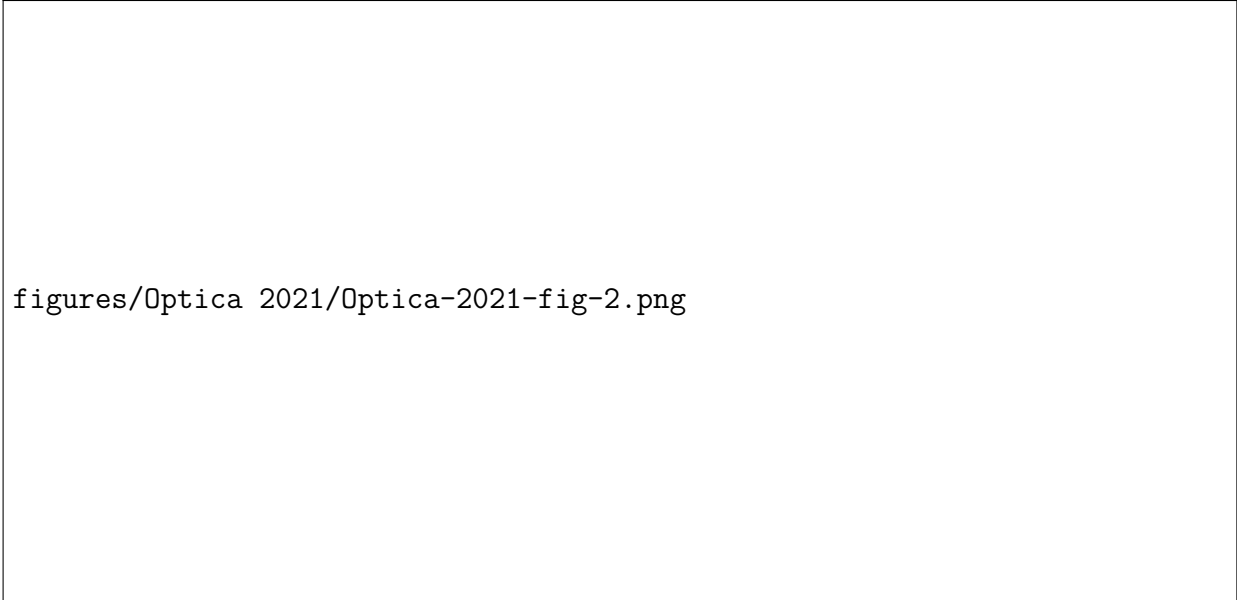


Figure 5.3: 3D imaging of cellulose acetate transparency ladder at 2600 cm^{-1} shown at different perspective angles (a) and (b). Though reflected from the same surface 2, photons propagating through cellulose acetate sheet 1 are temporally delayed (2') with respect to photons that travel in air (2). (c) Spatial cross-section of MIR pulse propagation in layered cellulose acetate structure. (d) Gauss fit for response on 2' interface (propagation through cellulose acetate). FWHM indicates spatial resolution of $12.6\text{ }\mu\text{m}$.

5.3 Results

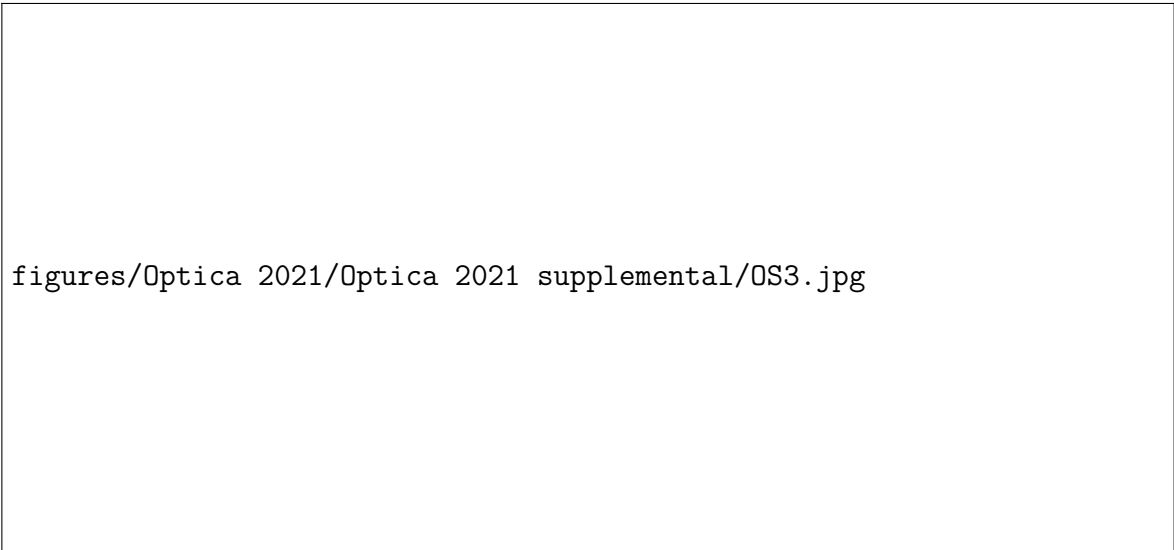
The 3D imaging capabilities of the wide-field NTA method by controlling the time delay between the MIR and NIR pulses was studied by first use of a model system. Figure 5.4(a) depicts a 3D image of a one cent US coin. This reconstruction is comprised of individual 2D wide-field images acquired at 100 ms/frame using 10 steps along the axial dimension, corresponding to a $\sim 75 \mu\text{m}$ sample height and an effective total acquisition time of 1 s. Two optical slices of the data stack are shown in Figs. 5.4(b) and (c), depicting the rectangular pillars of the Union Shield at different heights. The axial difference between these 2D layers is $30 \mu\text{m}$, which corroborates the height of the structures as revealed with confocal microscopy (Figure 5.5).

Whereas reflection/scattering off metal/air interfaces allows high-contrast imaging, in Fig. 5.4(c) we show that NTA-enabled detection also permits tomographic imaging of materials with a refractive index much closer to that of air. For this purpose, we used a polymer structure, consisting of a two-step ladder comprised of two $100 \mu\text{m}$ thick cellulose acetate sheets. The image reveals a $\sim 105 \mu\text{m}$ step size of the ladder, which closely matches the actual sheet thickness. The small difference between these values is attributed to flatness variations of the sheets, causing slight variations in the step size.



figures/Optica 2021/Optica-2021-fig-2.png

Figure 5.4: (a-c) Tomographic imaging of the structured metal surface of a one cent US Coin (Union Shield). (a) 3D reconstruction; (b) and (c) frames measured at height $h = 30 \mu\text{m}$ and $h = 0 \mu\text{m}$, respectively. (d)-(f) Tomographic imaging of stacked cellulose acetate sheets, a weakly reflection polymer structure. (d) 3D reconstruction; (e) and (f) 3D frames take at the top of each sheet ($\Delta h = 105 \mu\text{m}$). Total 3D scan time is 1 second.

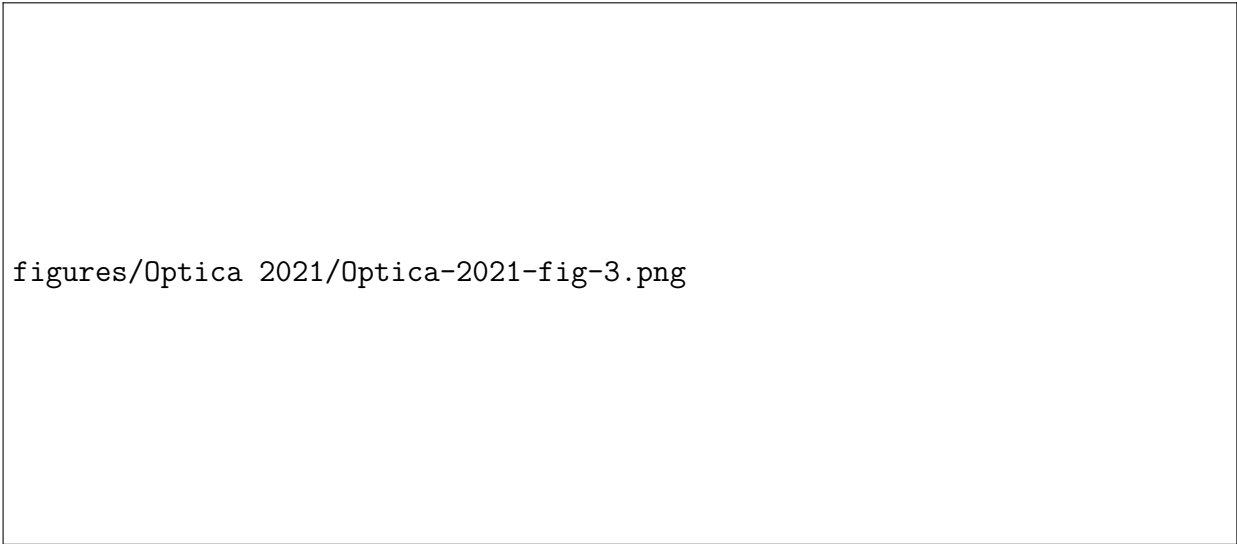


figures/Optica 2021/Optica 2021 supplemental/OS3.jpg

Figure 5.5: (a, b, c) Tomographic imaging of the structured metal surface of a one cent US coin (Union Shield). (a) 3D reconstruction, (b) and (c) are frames measured at height $h = 30 \mu\text{m}$ and $h = 0 \mu\text{m}$, respectively. (d) 3D reconstruction of confocal reflection imaging of the coin. (e) and (f) are 2D confocal scans measured at height difference $30 \mu\text{m}$.

5.3.1 3D imaging through transparent and highly absorbing media

Compared to tomographic imaging in the visible range, MIR based tomography benefits from reduced light scattering in various solids, permitting imaging through thicker materials. To illustrate this point, we perform tomographic imaging of a coin hidden behind a 3 mm GaAs wafer, shown schematically in Fig. 5.6(a). Although GaAs shows minimal absorption at the 2850 cm^{-1} energy of the MIR pulse, reflection at the wafer's top and bottom surfaces reduces the overall transmission of MIR light by 75% in the double-pass configuration. Figure 5.6(b) shows that, despite these losses, tomographic images of the coin's features can still be clearly distinguished. Moreover, the weak reflection off a three-step cellulose acetate ladder provides sufficient backscattered light for collecting a 3D image, depicted in Fig. 5.6(c), even though it is covered by a visibly opaque material of high refractive index.



figures/Optica 2021/Optica-2021-fig-3.png

Figure 5.6: Sketch of penetration experiment arrangement through (a) 3 mm thick GaAs wafer and (d) $190\text{ }\mu\text{m}$ water layer. (b) 3D reconstruction of one cent US coin (Union Shield) through 3 mm GaAs wafer. (c) Tomographic imaging of stacked cellulose acetate sheets through 3 mm GaAs wafer. Imaging of one cent US coin (Union Shield) through $190\text{ }\mu\text{m}$ water layer ($380\text{ }\mu\text{m}$ in double pass) at (e) 2850 cm^{-1} and (f) 2600 cm^{-1} .

The detection sensitivity afforded by using femtosecond pulses on the CCD camera also enables detection of objects placed under strongly absorbing materials. In Fig. 5.6(d), we

covered the coin with a 190 μm layer of deionized water. Water displays a strong MIR absorption due to the OH-stretching modes, which peaks in the 3000-3500 cm^{-1} range, with broad wings that extend to lower energies beyond 2600 cm^{-1} . In Fig. 5.6(e), the coin is visualized when the MIR energy is set to 2850 cm^{-1} , showing low signal due to the strong water absorption. At this setting, a double pass through the water layer amounts to a MIR intensity loss of $\text{OD} > 4$. When tuned to 2650 cm^{-1} , however, a two-dimensional image of the coin surface can be observed under the water at a 100 ms exposure time, despite a MIR transmission loss of $\text{OD} > 2$. Here, the much lower signal levels necessitate subtraction of the DTA background (~ 200 counts), yet the results underline that fs-NTA detection is sensitive enough to retrieve MIR images even in the presence of thick water layers.


5.3.2 Chemically-sensitive tomographic imaging

Using fs-NTA detection, we illustrate the principle of chemically selective 3D imaging by producing 3D images of the cellulose acetate ladder at different vibrational energies, shown in Fig. 5.7(a). To enhance contrast, letters have been printed on each layer using black ink. The FTIR spectrum of cellulose acetate is plotted in Fig. 5.7(b). Based on the theory of external MIR reflectance spectroscopy discussed above, we may expect strong reflection off cellulose acetate when tuning to the red side of the CH-stretching vibration, where the real part of the complex refractive index displays a local maximum. When tuning to 2875 cm^{-1} , near the peak of the CH-stretching band, a bright tomographic image is obtained as illustrated by the two projections in subfigures 5.7(c) and 5.7(d). At lower energies away from the resonance, the refractive index is expected to decrease, resulting in reduced reflection off the interface of the cellulose acetate material. This is indeed observed in subfigures 5.7(e) and 5.7(f), where the 3D image acquired at 2600 cm^{-1} is now significantly less bright compared to the near-resonance condition at 2875 cm^{-1} .

figures/Optica 2021/Optica-2021-fig-4.png

Figure 5.7: 3D imaging of stacked cellulose acetate sheets with printed letters. (a) 3D reconstruction of the structure. (b) FTIR transmission spectrum of cellulose acetate (blue line) and real part of the refractive index obtained through a Kramers-Kronig transformation (orange dotted line). Rectangles represent Gaussian pulse width of 150 cm^{-1} . (c) and (d) 3D imaging at 2875 cm^{-1} ; (e) and (f) 3D imaging at 2600 cm^{-1} . Total image acquisition time is 1 second.

The reduced reflection at 2600 cm^{-1} enhances light penetration in the sample, which allows collection of signal contributions from lower lying interfaces. As shown in Figure 5.3, signals from the buried interfaces (surface 2' and 3' in Figure 5.8) are clearly observed in the off-resonance condition. Since the optical path length is determined by the refractive index of the material, the apparent depth of the buried interfaces differs from that of the corresponding air-exposed interfaces (surface 2 and 3 in Fig. 5.3). From this time/optical path difference, we estimate the refractive index of cellulose acetate to be ~ 1.5 at 2600 cm^{-1} , resulting in a 4% Fresnel reflection at the sheet/air interface.

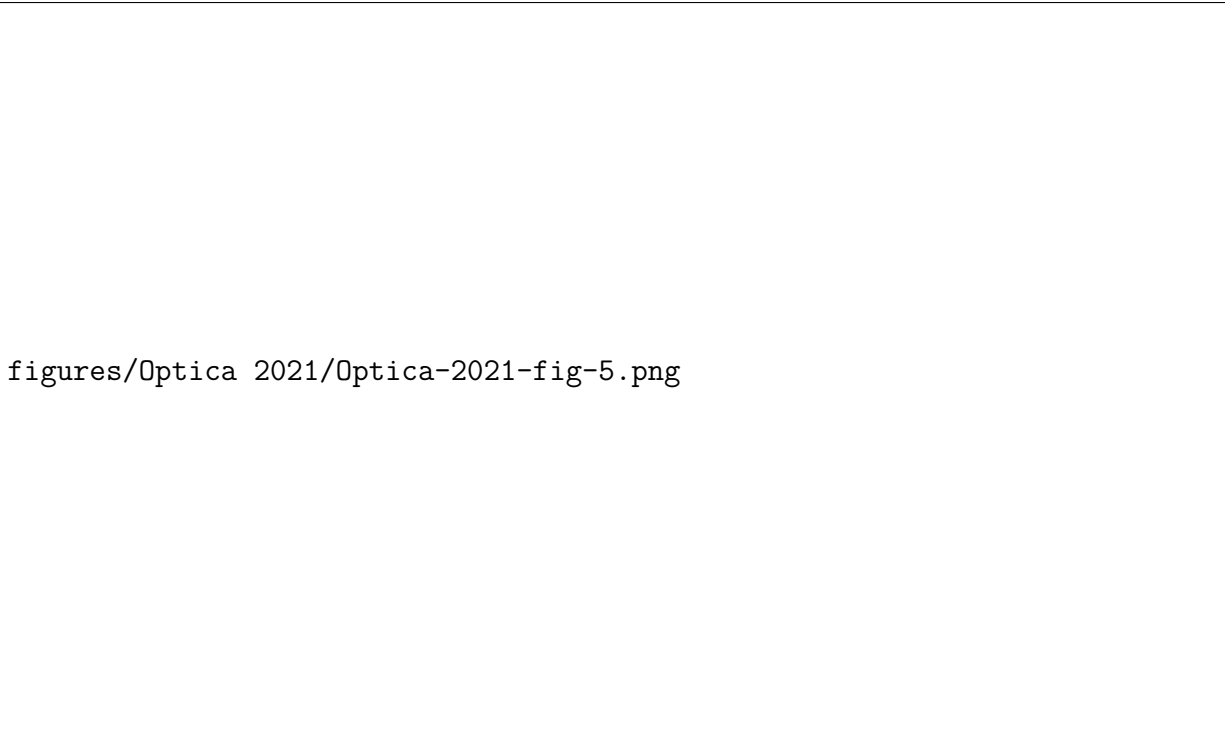


figures/Optica 2021/Optica 2021 supplemental/OS7.jpg

Figure 5.8: 3D image of cellulose acetate structure imaged at 2600 cm^{-1} and 2850 cm^{-1} from a top view perspective. (c) Peak positions of reflections off the different interfaces. The difference between the peak positions found for propagation in air and polymer reveals that $n \sim 1.5$ for 2600 cm^{-1} and $n \sim 1.87$ for 2850 cm^{-1} .

We next show 3D images of polymer structures fabricated with a projection-based photolithography technique (see the Methods section of this chapter). A visible image of the structure is shown in the inset of Fig. 5.9(a), and the relevant part of the FTIR spectrum of the polymer is given in Fig. 5.9(b). We observe increased signals from the structure's top surface when the MIR energy is tuned into near resonance with the material's CH-stretching vibrational mode [subfigures 5.9(c) and 5.9(d)] and lower signals when the MIR energy is tuned off resonance [subfigures 5.9(e) and 5.9(f)]. Due to the shape of the structure, sig-

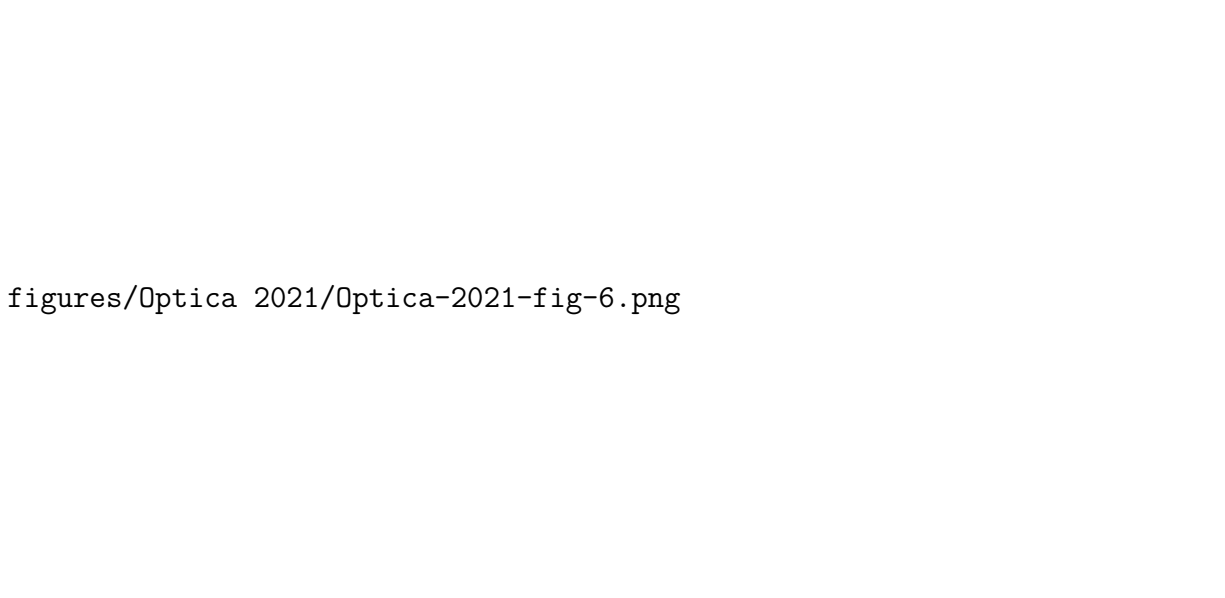
nificant light scattering occurs at angles beyond the collection NA of the imaging system, producing darker regions at curved surfaces.



figures/Optica 2021/Optica-2021-fig-5.png

Figure 5.9: 3D imaging of a resin structure manufactured through projection-based photolithography. (a) 3D reconstruction of resin structure. (b) FTIR absorption spectrum of the resin (blue line) and real part of the refractive index obtained through a Kramers-Kronig transformation (orange dotted line). Rectangles represent Gaussian pulse width of 150 cm^{-1} . (c) and (d) 3D imaging at 2775 cm^{-1} ; (e) and (f) 3D imaging at 2450 cm^{-1} . Structure height is $50 \mu\text{m}$. Images have been corrected for non-spectroscopic NTA efficiency variations (see Figure 5.2). Total image acquisition time is 1 second.

Last, we perform MIR tomography of a hydrated protein crystal. In Fig. 5.10, we show a 3D reconstruction of lysozyme crystals. The lysozyme enzyme forms stable tetragonal crystals that can grow to millimeter scales. The structure visualized in Fig. 5.10(a) is composed of an aggregate of smaller crystals, while Fig. 5.10(b) shows a 3D image of a single crystal. The spectral dependence of the signal from a single surface is presented in subfigures 5.10(c)–(e), confirming the chemical contrast encoded in the MIR light scattered onto the detector.



figures/Optica 2021/Optica-2021-fig-6.png

Figure 5.10: Imaging of different lysozyme crystals on mica glass. (a) 3D reconstruction of lysozyme crystal cluster at 2875 cm^{-1} , (d) 2600 cm^{-1} , and (f) 2450 cm^{-1} . Images have been corrected for non-spectroscopic NTA efficiency variations. FTIR absorption spectrum of lysozyme is shown on far right.

5.3.3 Faster 3D imaging with InGaAs

Since the time delay used in the experimental setup in 5.1 can be scanned rapidly, it allows for rapid acquisition of 3D image stacks. When combined with the increase in acquisition speed afforded by the InGaAs camera as mentioned in the previous chapter, truly high-speed 3D imaging in the MIR is within reach. The operating principle here remains the same, but again changing the camera substrate from Si to InGaAs to take advantage of its increased TPA coefficient. In Fig. 5.11, we demonstrate the same imaging capabilities by again visualizing features on the US penny and dime. Each 2D image frame is acquired in 1 ms, corresponding to a single laser shot from the NIR gate and MIR signal and with 20 images in the 3D data stack, the effective acquisition time is 20 ms. Such volumetric imaging rates are more than 50 times higher than the first experiments with Si done above, emphasizing the drastic improvement of imaging performance with InGaAs cameras.

The image area is mostly blank, with the text 'figures/APLP 2021/APLP 2021 fig 4.jpeg' centered. This text likely represents a missing or broken image link in the document's rendering.

figures/APLP 2021/APLP 2021 fig 4.jpeg

Figure 5.11: FIG. 5. Tomographic images of the US penny (a) and dime (b) scanned at 4250 nm (2350 cm^{-1}). The total acquisition time for each volumetric scan is 20 ms.

5.4 Discussion

The developments discussed in this chapter builds on wide-field NTA-enabled MIR imaging by extending this detection principle to 3D imaging mapping, optimally leveraging the time-gating property of fs-NTA. Our technology is fundamentally different from existing OCT techniques that operate in the MIR. The most promising MIR-OCT approaches are currently based on the Fourier-domain OCT (FD-OCT) [135, 136], which accomplishes depth scans (A-scan) or cross-sectional scans (B-scans) on a time scale set by the spectral acquisition time of the detector. This detection strategy has been successfully translated to MIR-OCT using both classical [101] or quantum [106] light, with A-scans acquired in just under 10 ms. However, in combination with lateral raster scanning, such imaging conditions translate into rather long total volume acquisition times of minutes/volume, extended further in duration by necessary referencing and postprocessing.

In contrast, volumetric imaging through fs-NTA uses different mechanisms for capturing information along the lateral and axial dimensions. First, fs-NTA uses a wide-field detection approach, which allows detection of both lateral dimensions in a single shot. The massively parallel detection enabled by Mpx camera chips provides a dramatic increase of the effective acquisition rate. We have used an off-the-shelf CCD camera, with an effective readout time of 10 Hz for Si and 500Hz with InGaAs. Using the Si camera, we initially reported a total effective acquisition time of 1 s (10 frames/s, 10 axial steps) for the 3D data stack, and were able to massively improve on this to 20 ms per stack by implementation of the InGaAs camera. Second, the axial information in fs-NTA tomography is retrieved through a scan of the time delay between the MIR and the gate pulses. Scanning along this dimension can be accomplished with automated translation stages over 1 mm distances, with 1.5 μm (5 fs) repeatability and 2 ms response times. Finally, the imaging system was based on a simple positive telescope with long focal lengths, with a very limited numerical aperture for scattered light collection. The highly directional output of the laser system in use alleviates this requirement substantially, as the tight propagation direction of the signal beam will ensure collection of relatively flat samples, but fails for highly scattering samples, such as the lithographed sample in 5.9. Improving the collection optics can increase both the amount of scattered light imaged and increase the magnification, allowing for tomographic imaging of microscale objects.

Compared to spectral interferometry approaches, volumetric imaging with fs-NTA is significantly more robust. Wide-field fs-NTA requires no DTA-background subtraction nor multiple processing steps to retrieve the MIR signal. Instead, 2D images are acquired in single-shot mode, allowing rapid and unimpeded axial scans for collecting 3D data stacks. For our current imaging conditions, the signal-to-noise ratio (SNR) of each frame is 68 dB for a 100 ms integration time, determined by using a gold mirror as the sample. The NTA to DTA background ratio is 15 dB, which is sufficiently high for enabling imaging under virtually background-free conditions.

We have also shown that MIR tomographic imaging enabled by fs-NTA exhibits chemical contrast based on vibrational resonances of the sample. Although the spectral resolution is limited by the bandwidth of the MIR pulse ($< 150 \text{ cm}^{-1}$), the spectroscopic contrast imparted by the sample's vibrational modes is clearly observed. It is nontrivial to achieve similar contrast with conventional FD-OCT methods, where spectroscopic imprints are difficult to retrieve in the presence of the strong interferometric modulations of the detected spectrum. Therefore, although MIR-OCT is recognized for its greater penetration depth, chemically selective imaging has remained a challenge.

5.5 Methods

5.5.1 Fourier Transform Infrared Spectroscopy

The MIR absorption of materials is measured with a commercial Fourier transform infrared (FTIR) spectrometer (Jasco 4700) either in transmission mode or by using an attenuated total reflection (ATR) accessory equipped with a diamond crystal.

5.5.2 MIR femtosecond NTA imaging system

The imaging system is schematically depicted in Fig. 1(a). A 1 kHz amplified femtosecond laser system (Spitfire Ace, Spectra Physics) is used to seed two optical parametric amplifiers (OPA, Topas Prime, Light Conversion). One OPA is used as a source of NIR gate radiation at 1200 nm. The signal and idler pulses from the second OPA system are used to generate MIR pulses ($< 3000 \text{ cm}^{-1}$) through the process of difference frequency generation in a nonlinear medium. Both MIR and NIR pulses are recombined on a 1 mm ZnSe window, which serves as dichroic mirror, after which the pulses are overlapped on a CCD camera

(DR-328G-CO2-SIL Clara, Andor). Temporal overlap is controlled through a mechanical delay stage (GTS150, Newport). The MIR imaging system consists of two 100 mm CaF_2 lenses, resulting in a 1:1 imaging system with $\text{NA} = 0.015$. The incident angle of the MIR beam on the sample is less than 5° , resulting in an error for z-height determination of less than a percent. All experiments are performed with fixed MIR and NIR irradiances of 3.5 GW/cm^2 and 2.7 GW/cm^2 , respectively, on the camera chip. Further details can be found in Supplement 1, Table 1. For the given pulse spectral bandwidth and camera parameters, the NTA efficiency curve is flat for MIR tuning in the $2600 - 3000 \text{ cm}^{-1}$ spectral range and decreases for lower energies beyond $\sim 2500 \text{ cm}^{-1}$ because of MIR absorption by the camera's protective window. On the higher energy side, the accessible spectral range is limited by the light source and the available photon energies through difference frequency mixing.

5.5.3 Polymer structure fabrication

The computer-aided design models of the structures (SolidWorks) are virtually sliced into 2D layers with a slice thickness of $20 \mu\text{m}$. Mask projection images are generated for each layer [39]. The exposure time of each layer is adjusted based on the light intensity and the photosensitivity of the printing material (ranging from 5 to 8 s) to improve the fabrication accuracy. The UV-curing photopolymer resin from Elegoo Inc. is used for structure fabrication due to its desired IR property. The resin is used directly without modification. In the projection-based stereolithography process, the photocurable resin is deposited on the surface of a transparent resin tank. To generate the 2D patterned light beam, 405 nm wavelength light is reflected by a digital micromirror device (DMD) comprised of a 1920×1080 array of micromirrors, and the brightness of each pixel in the projected light beam is controlled by adjusting the angle of the corresponding micromirror in the DMD.

5.5.4 Confocal imaging of coin structure

The 3D images are acquired with a Leica SP8 DIVE microscope operated in the reflectance confocal imaging mode using a 532 nm light source and a 10 \times , 0.3 NA objective. The images are acquired as z-stacks of mosaics (adjacent fields of view stitched together). The area of each en-face mosaic frame is 13.5 \times 9.3 mm, and the distance between the frames in the z-stack is 5 μ m.

5.5.5 Lysozyme crystals growing and handling

Hen egg white lysozyme is purchased from Fisher Scientific (ICN19530325). The lyophilized powder is dissolved to 20 mg/mL in 100 mM sodium acetate at pH 4.5. Batch crystallization is performed with the lysozyme solution in a 1:1 ratio with 1 M NaCl in 100 mM sodium acetate at pH 4.5.

Chapter 6

Spectral Imaging using Chirped Pulse Nondegenerate Two-Photon Absorption

6.1 Introduction

In spectral imaging, each pixel in a two-dimensional (xy) image is expanded along the optical frequency (ω) axis, yielding an information-rich data cube ($xy\omega$) of both spatial and spectral information. When realized in the mid-infrared (MIR) spectral region, spectral imaging allows direct spatial differentiation of chemical composition, providing an indispensable tool for many applications in chemical, medical, and bio-related fields [137–141]. However, a broader utilization of the technique for applications that require both high-speed and high-definition imaging capabilities has remained challenging. Conventional interferometric Fourier transform infrared (FTIR) methods are generally too slow for rapid analysis or in situ observations of real-time processes [12]. In this context, there is a need for MIR

spectral imaging technologies that combine high-pixel density mapping with high acquisition and image processing speed.

In the previous chapters, using an InGaAs camera for NTA has allowed for dramatic increases in image acquisition rates up to 500 fps. This chapter seeks to capitalize on the increased sensitivity to achieve spectral imaging. We introduce a spectral scanning strategy that takes advantage of the NTA imaging conditions of rapid illumination. Using temporally chirped MIR pulses and a short NIR gate pulse, we show that MIR spectral data cubes ($xy\omega$) over a spectral range of $> 400 \text{ cm}^{-1}$ can be acquired in under 1 s with a >1 -megapixel (Mpx) InGaAs camera. Without the necessity for image processing or reconstruction, this approach has the potential for true video-rate hyperspectral data acquisition of live processes, enabling rapid data acquisition in all four dimensions, i.e., a ($xy\omega t$) hypercube.

6.2 Concept and design

Chirping an ultrafast pulse refers to the dispersion of the frequency content in time. In the context of NTA, this temporal spreading reduces the MIR frequency content the gate can interact with to produce a signal at the detector plane, increasing the spectral resolution substantially from the whole bandwidth of the image carrying beam to some portion of it. Delaying the arrival time of the gate within the dispersed pulse then allows for selection of image forming frequency content over the pulse bandwidth. In previous images using either ps or fs pulses, the contrast derived from the MIR absorption had a spectral resolution of the entirety of the pulse bandwidth. In the picosecond illumination regime, this resolution was 5 cm^{-1} , which is sufficient to resolve most condensed phase MIR absorption features and poses little issue to retrieving sample information. For femtosecond pulses used in later experiments, this resolution is more than 100 cm^{-1} , allowing only the most broad determination of sample chemical composition. The focus here is to predictably arrange the

effective frequency at any time within the pulse to select image forming frequencies in each NTA image. The quantity of interest is given by the first derivative of the time domain phase of the MIR pulse, $\phi(t)$, referred to as the *instantaneous frequency* [142]:

$$\omega_{inst}(t) = \frac{d\phi}{dt} \quad (6.1)$$

While there are numerous methods that have been developed to do this elegantly, including blazed grating pairs [143, 144], engineered optical fibers [145, 146], and pulse shapers [147–149], the method of choice that balances cost over correctly dispersing a very broad MIR range was simply to pick a reasonably long material whose dispersive character predominately imparts a quadratic time domain phase to the MIR pulses. The material of choice for this was found to be undoped silicon, whose dispersion in the spectral region of interest provides a mostly linear instantaneous frequency to the pulse bandwidth used in experiments. To see how the silicon can spread this pulse in time before upconversion at the detector plane, we start by describing the electric field in the frequency domain as a Gaussian:

$$E(\omega) = A_\omega \exp\left(-\frac{(\omega - \omega_0)^2}{4\sigma_g^2} + i\phi(\omega)\right) \quad (6.2)$$

where A_ω is the amplitude, ω_0 is the carrier frequency, σ_g is the Gaussian width of the pulse, and $\phi(\omega)$ is the spectral phase. The spectral phase will dictate changes to the envelope of the time domain field by redistributing the spectral energy of the pulse in time. For perfectly mode locked pulses, there is no relative phase accumulation between the carrier frequency and the rest of its constituents, and its spectral phase is constant or zero. Upon passage through a material of length L , the frequency dependent refractive index $n(\omega)$ imparts some spectral phase onto the pulse. To describe these effects of the medium on a broad bandwidth pulse, the spectral phase is commonly understood by a Taylor expansion of the material dispersion

around the carrier frequency:

$$\phi(\omega) = \phi_0 + \frac{n(\omega)\omega}{c} \cdot L = \phi_0 + k(\omega) \cdot L \quad (6.3)$$

$$k(\omega) = k(\omega_0) + k'(\omega_0)(\omega - \omega_0) + \frac{k''(\omega_0)}{2}(\omega - \omega_0)^2 + \frac{k'''(\omega_0)}{6}(\omega - \omega_0)^3 \quad (6.4)$$

where $k(\omega)$ is the phase acquired per unit distance. For most pulses in the femtosecond range, retaining the first four terms is sufficient. The first two terms correspond to the propagation phase of the carrier frequency $k(\omega_0)$ and the group velocity of the pulse $k'(\omega_0)$, have no material impact on the time domain envelope of the pulse. The third and fourth terms, called group velocity dispersion (GVD) $k''(\omega)$ and third-order dispersion (TOD) $k'''(\omega)$, however, do modify the shape of the pulse in time and will be the focus of choosing the right material. As the group velocity dispersion modifies the influence of the quadratic term in the spectral phase, the derivative of its time domain equivalent will be linear in time, producing the desired linear temporal dispersion. Third-order dispersion produces a quadratic dependence of the instantaneous frequency and will unfavorably distort the distribution in time. An ideal medium would be one that offers very high GVD and no TOD (or higher) to chirp the pulse linearly in time over a short propagation length.

However, in practice, balancing GVD, material length, and unwanted higher order dispersion is achieved by considering two predominant factors. The first is that the bandwidth of the input pulse will decide how many factors of dispersion are to be included. If the bandwidth is sufficiently large, then the primary character will be of higher order as a nonlinear dependence eventually supersedes lower order terms, irrespective of the magnitude of the derivatives in a practical scenario. The second factor is then the material itself, whose dispersive character will vary the magnitude and sign of the participating terms. The length of the material can only scale its dispersive influence on the ultimate width of the pulse. Therefore to obtain a mostly linear instantaneous frequency, the chosen material should have a large second-order term relative to terms of higher order.

A straightforward numerical test of prospective materials is as follows [150]. If the frequency dependent refractive index of a medium is known, then the frequency dependent phase terms can be determined, and the phase changes of the different frequency components of the pulse as they travel a length L can be calculated. The time domain electric field $E(t)$ can then be computed through a Fourier transformation:

$$E(t) = \mathcal{F}^{-1}[E(\omega)] = \int_{-\infty}^{\infty} E(\omega)e^{i\omega t}d\omega \quad (6.5)$$

$$E(t) = A(t)e^{-i\phi(t)} \quad (6.6)$$

where in the last line the field is written in terms of its amplitude $A(t)$ and temporal phase $\phi(t)$. The spectral phase prepared in the frequency domain will produce terms of the same order in the time domain, weighted accordingly by the material parameters, along with the carrier frequency phase to give form to the time domain phase. Considering only terms related to GVD and TOD yields:

$$\phi(t) = \omega_0 t + \beta t^2 + \gamma t^3 \quad (6.7)$$

Where β and γ are factors related to $k''(\omega)$ and $k'''(\omega)$, respectively. Taking the derivative of this phase results in the instantaneous frequency of a pulse modified by propagation through a dispersive medium:

$$\omega_{inst}(t) = \frac{d\phi}{dt} = \omega_0 + 2\beta t + 3\gamma t^2 \quad (6.8)$$

The results of this procedure for the 15 cm Si rod used in the experiments are shown in Figure 6.1. The original pulse is a 40 fs bandwidth limited pulse that is centered at 3000 cm^{-1} , with a flat spectral phase. The pulse is then stretched to approximately a width of 4800 fs, using the material dispersion parameters for Si obtained from literature [151]. This pulse is then compared to the same pulse dispersed using only the GVD term. Upon inspection,

there will be some influence of the TOD term, as the pulse envelope is slightly asymmetric relative to the uniform broadening of the ideal. However, the instantaneous frequency over the temporal width of the pulse shows a nearly straight line, indicating that the spectral phase imparted by the Si is primarily due to GVD, indicating that 15 cm of Si will produce a chirp that is essentially linear.

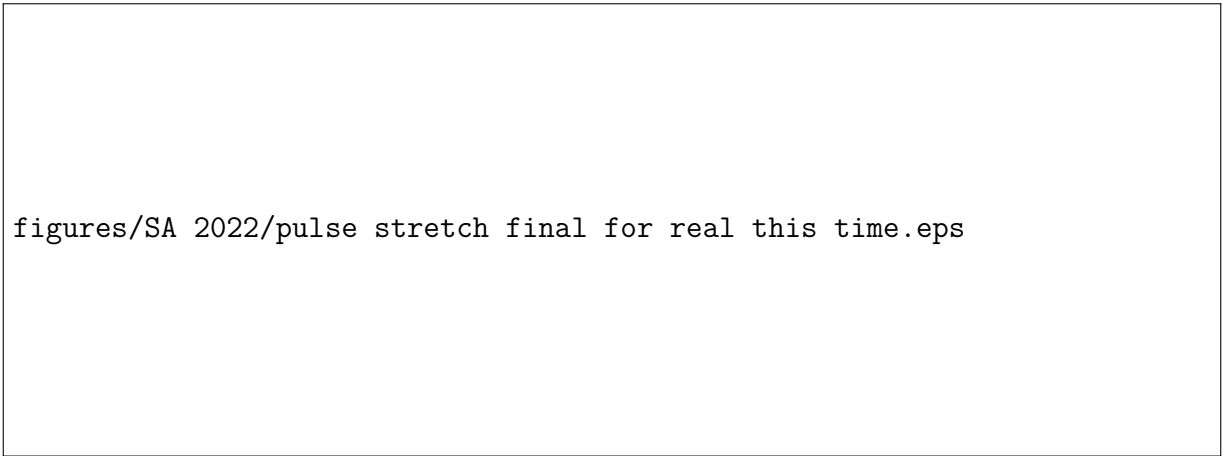


Figure 6.1: Left: 40 fs MIR pulse before and after dispersion by 15 cm of Si. Right: 40 fs MIR pulse broadened using both GVD and TOD and its corresponding instantaneous frequency. Pulse broadened only by GVD is shown as a reference.

To see the influence of the linear chirp on the spectral resolution of NTA imaging, consider again a MIR pulse with a temporal width of 40 fs that is bandwidth limited. In the frequency domain, such a pulse manifests itself with a constant spectral phase. In the time-frequency plot of Fig 6.2a, the constant spectral phase is associated with a narrow temporal distribution of the different frequency components in the pulse. When the bandwidth-limited pulse transmits through a sample, for instance, a thin layer of polystyrene, its spectrum is modified because of the linear absorption of light by the polymer Fig 6.2a. The pulse spectrum now shows narrow spectral features in its otherwise broad spectral profile. In the time domain, the narrow imprints in the MIR pulse spectrum produce almost invisible modification to the temporal profile, most notably a decrease of the overall intensity and the introduction of an extremely shallow pedestal, as shown in Fig 6.2b. The NTA signal is obtained by temporally

overlapping the MIR pulse with a short NIR gate pulse on the detector. If the gate pulse is scanned in time relative to the MIR pulse, the convolution results in a profile that lacks clearly resolved features related to the MIR spectral imprints.



Figure 6.2: Visualized concept of chirped pulse-NTA (CP-NTA). The broad pulse spectrum is modified because of linear absorption of light by the sample (a and c). Inset shows a time-frequency plot of the MIR pulse in the absence or presence of linear chirp. (b and d) The resulting pulse shape in the time domain without (b) and with (d) introduction pulse chirp. Dark blue lines illustrate the convolution between the MIR and gate pulses.

The situation is different if a linear chirp is applied to the MIR pulse. The time-frequency

plot in the inset of Fig. 6.2c shows the original MIR pulse that has been linearly chirped to a temporal width of 4.5 ps, corresponding to a quadratic spectral phase. Different frequency components now have their maximum intensity at different moments in time. Whereas the spectral phase has no direct effect on the absorption imprints in the pulse’s power spectrum that is observed in the frequency domain Fig. 6.2c, it has a profound effect on the MIR pulse in the time domain. As shown in Fig 6.2d, the time-resolved MIR pulse shows variations that mimic the spectral features in the frequency domain. In the case of linear chirp, there is a linear relationship between the time and frequency axis, allowing a direct reading of the spectrally encoded information in the time domain. Using the gated principle of NTA detection, the MIR pulse spectrum can be directly accessed through a rapid scan of the MIR and gate-relative time delay, i.e. a cross-correlation. Note that for sufficiently broadened MIR pulses, the spectral information is largely unaffected by the convolution with the gate pulse. The use of chirped pulses for encoding spectral information in time-domain signals has been demonstrated for various forms of spectroscopy [152] and has recently been an important approach for achieving high spectral resolution in coherent Raman scattering microscopy with broad bandwidth pulses [153, 154]. NIR chirped pulses have also been used to upconvert MIR signals to the visible range with the aid of nonlinear crystals [155, 156]. Here, we show that this principle can be extended to MIR spectral imaging through NTA by chirping the MIR pulse instead.

A schematic of the experimental implementation of the chirped pulse NTA (CP-NTA) imaging technique is shown in Fig. 6.3. We use an ultrashort MIR pulse centered at $3.33 \mu\text{m}$ (3000 cm^{-1}) that is stretched by a 15-cm long Si rod (see Materials and Methods). The stretched pulse is subsequently passed through the sample and imaged with two CaF_2 lenses onto a >1.3 Mpx lattice matched $\text{In}_{0.53}\text{Ga}_{0.47}\text{As}$ camera chip (0.734 eV, 1690 nm bandgap). The NIR gate pulse is centered at 1900 nm (5263 cm^{-1}) with a temporal width of 116 fs. The gate pulse passes through a delay stage before it is coincident with the MIR pulse on the detector chip. Note that the camera chip is covered with a fused silica protective

window, which substantially-attenuates the MIR beam (0.75 optical density at 3000 cm^{-1}). The intensity ratio between the MIR and the gate pulse is chosen such that the linear NTA signals are on par with the degenerate two-photon absorption (DTA) signal induced by the gate pulse. This DTA signal forms a constant background that does not affect the spectral information nor markedly change the detection dynamic range.

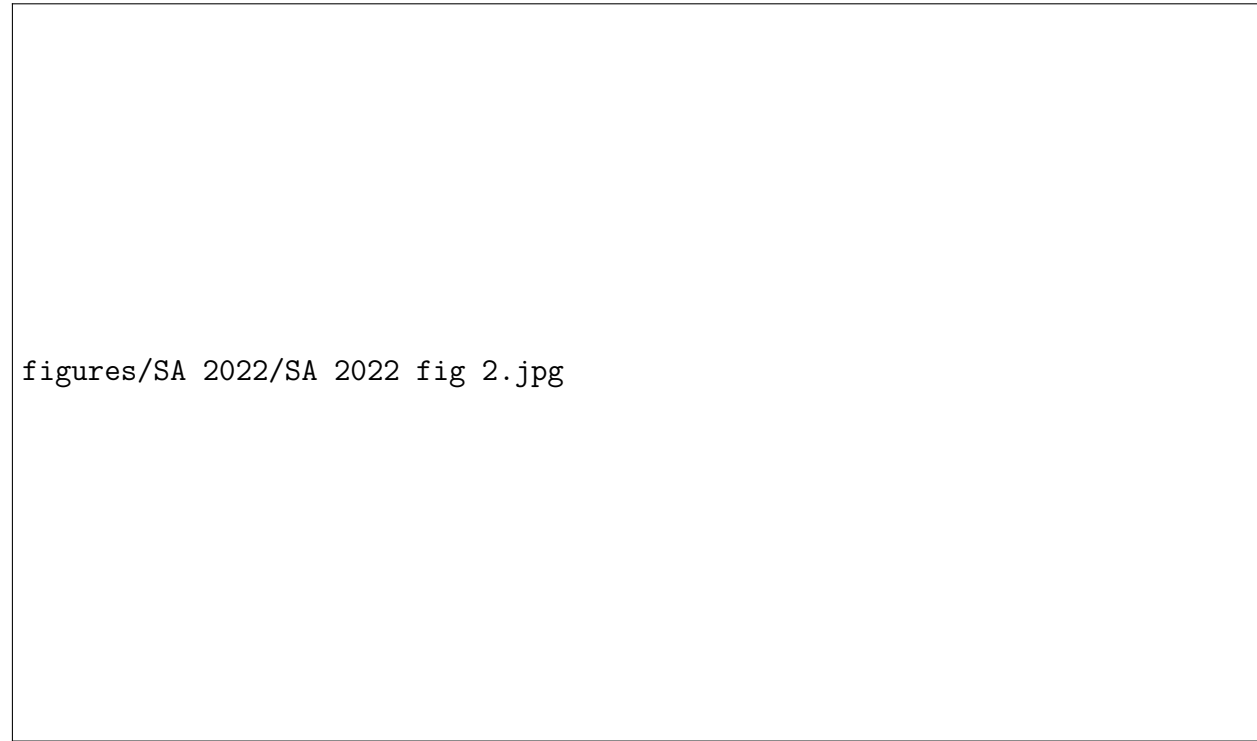


Figure 6.3: Schematic of experimental setup. An ultrashort MIR pulse is chirped by propagation through a 15-cm Si rod and spatially overlapped with a temporally short gate pulse on the camera chip. Control of the MIR-gate pulse time delay permits a rapid spectral scan across the MIR pulse spectrum.

The MIR pulse spectrum is shown in Fig. 6.5a, indicating a full width at half maximum (FWHM) of 360 cm^{-1} , as measured using a grating-based spectrometer equipped with a single-pixel MCT detector ($\sim 20\text{ s}$ per spectral point; see Materials and Methods). This spectrum supports a bandwidth-limited temporal width of 40 fs. Figure 6.5b depicts the NTA signal on the camera as a function of the MIR-gate delay time. We can find the temporal width of the MIR pulse from the NTA cross-correlation of the MIR and gate

pulses. In the absence of the Si rod, the MIR pulse duration is found as 160 fs, which is longer than the minimum width of 40 fs because of residual dispersion by the optical elements in the setup. Upon insertion of the Si material in the MIR beam, the NTA cross-correlation is substantially elongated in time, revealing a MIR pulse with a temporal width of 4.5 ps as shown in Fig. 6.4.

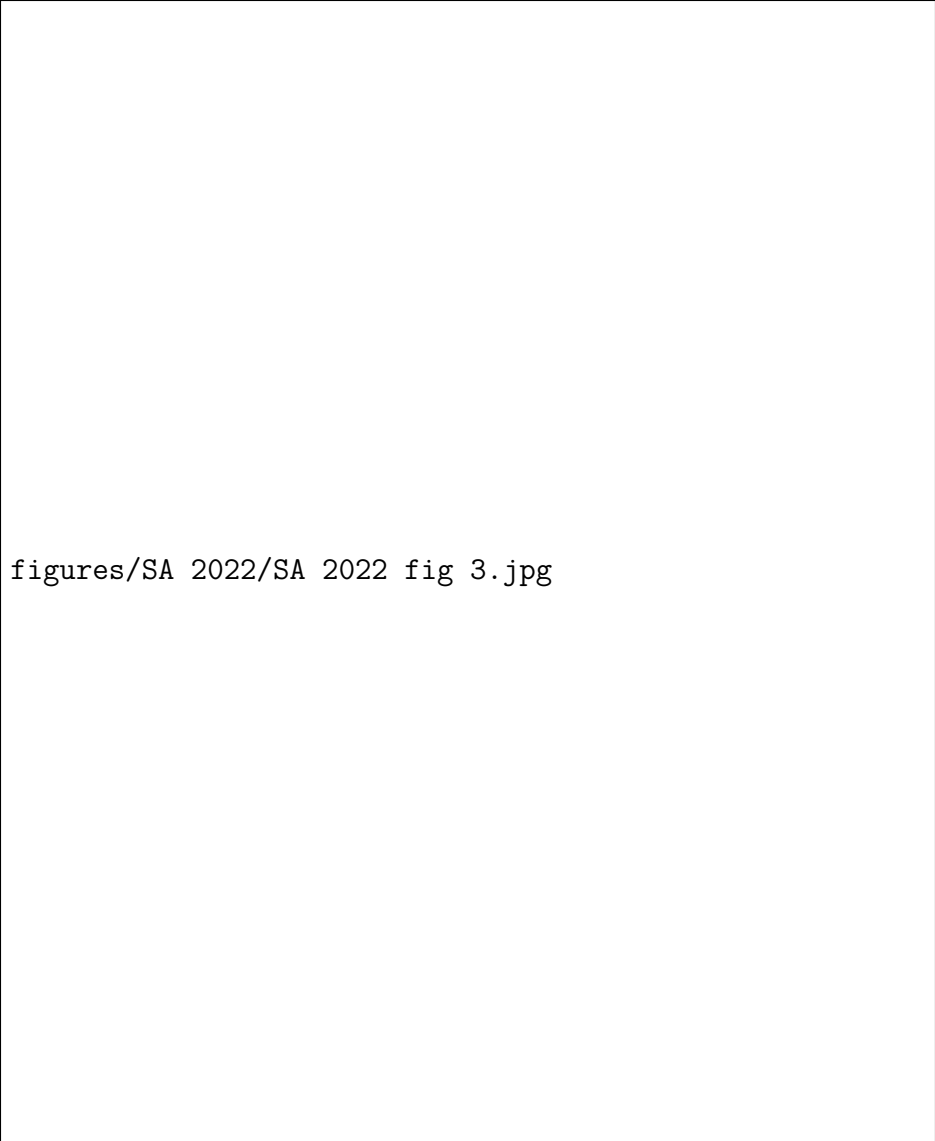


Figure 6.4: Average spectral irradiance and spectral energy per camera pixel of chirped MIR pulse.

6.3 Results

When the MIR pulse passes through a $7 \mu\text{m}$ layer of polystyrene, a frequency-domain measurement reveals a pulse spectrum with narrowband imprints of vibrational absorption lines as is evident from Fig. 6.5c. The absorption features correspond to the symmetric and

asymmetric stretching vibrations of the carbon-hydrogen bonds of polystyrene. Using the chirped pulse this spectral information can also be obtained in the time domain, as shown by the NTA cross-correlation in Fig. 6.5d. The time-domain measurement was collected using a 16 ms dwell time per spectral bin for a total effective acquisition time of 800 ms. In the current configuration, the available spectral range can be extended to $\sim 530 \text{ cm}^{-1}$ for a 1.1 s effective acquisition time per spectral sweep.



figures/SA 2022/SA 2022 fig 3.jpg

Figure 6.5: Demonstration of MIR spectroscopy using CP-NTA. Side-by-side demonstration of spectroscopy on polymer standard (7 μm thick polystyrene) in the frequency domain (spectrometer, left, A and C) and time domain (CP-NTA, right, B and D). (E and F) Retrieved absorption spectra are in good agreement with the polystyrene absorption lines. OD, optical density.

The corresponding MIR absorption spectrum can be derived from the measured pulse spectra, either in the frequency domain Fig. 6.5e or in the time domain Fig. 6.5f. Both datasets show good agreement with the signatures in the FTIR spectrum of polystyrene. Using the positions of the polystyrene absorption lines as calibration standards, we determine a


chirp rate of $\beta \sim 0.072 \text{ cm}^{-1}/\text{fs}$. This corresponds to an instrument response function of $\sim 8.4 \text{ cm}^{-1}$, which spans the frequency window of temporal overlap between the short gate pulse and the chirped MIR pulse. The latter is also confirmed from an analysis of the main polystyrene lines retrieved from CP-NTA. The spectral features at 2923 cm^{-1} (FTIR FWHM = 35 cm^{-1}) and 3025 cm^{-1} (FTIR FWHM = 15 cm^{-1}) yield spectral widths of 38 and 19 cm^{-1} , respectively, after convolution with a Gaussian resolution function of spectral width 8.4 cm^{-1} in Figure 6.6.



Figure 6.6: Gaussian fit of measured CP-NTA spectrum of polystyrene. The absorption lines at 2923 cm^{-1} (original FWHM= 35 cm^{-1}) and at 3025 cm^{-1} (original FWHM= 15 cm^{-1}) convolved with a Gaussian resolution function with width of 8.4 cm^{-1} results in 38 cm^{-1} and 19 cm^{-1} , respectively.

The linearity of the temporal chirp of the MIR pulse is important for direct frequency-to-time conversion. To confirm the linear distribution of frequency components, i.e., the linearity of the instantaneous frequency, we perform CP-NTA spectroscopic imaging with pulses of

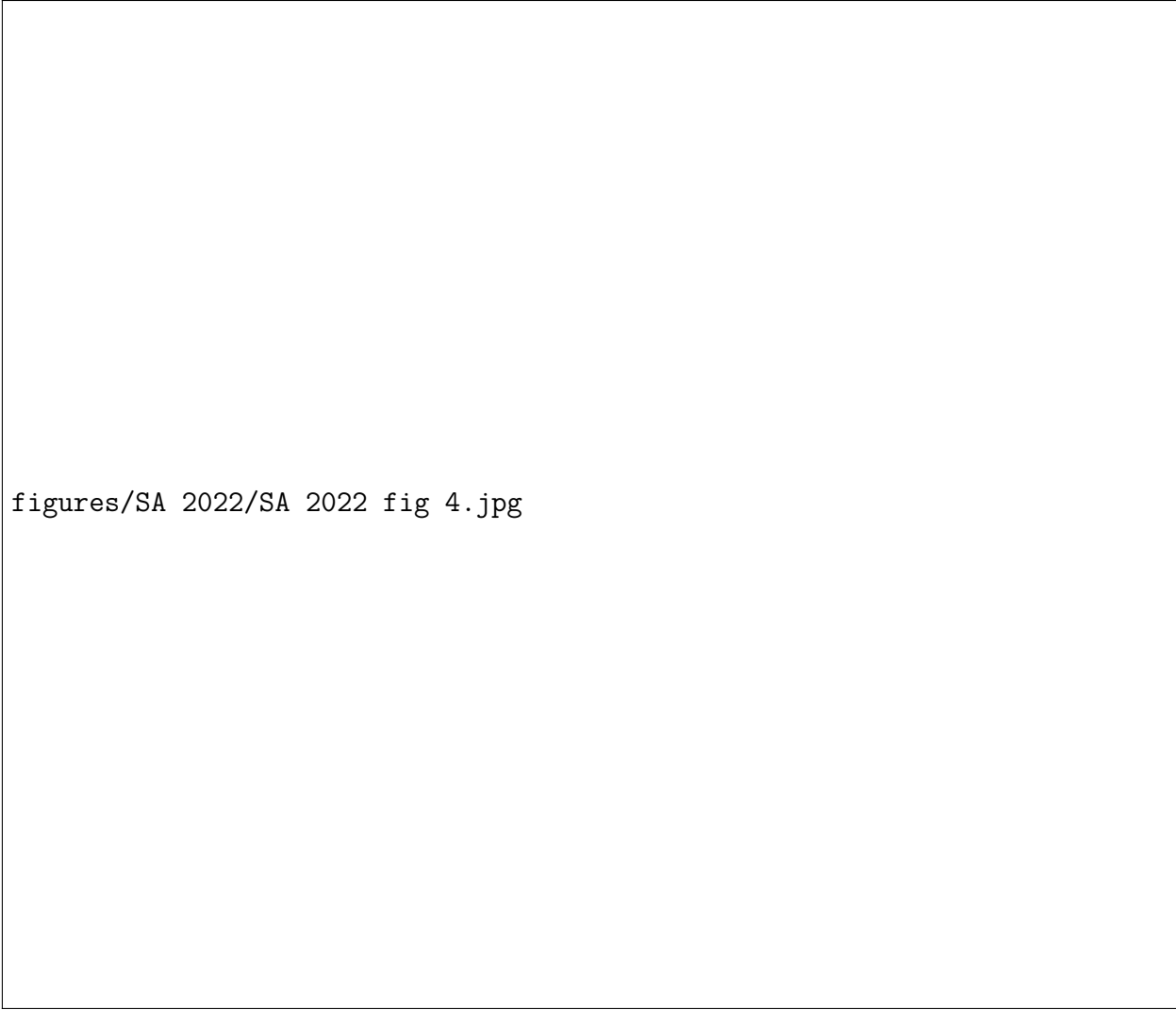
various carrier frequencies ω_0 around the polystyrene absorption bands (fig. 6.7). The data show that the line positions and overall absorption spectra remain identical regardless of carrier frequency of the MIR pulse. This observation indicates a good linearity of the instantaneous frequency distribution across the full width of the MIR pulse.



figures/SA 2022/SA supplemental/sciadvs6.jpg

Figure 6.7: Linear chirp study. Absorption spectrum of polystyrene measured through imaging CP-NTA using pulses of different central frequency. Line positions and separations of absorption features remain identical regardless of the features being at the center or at the wing of the pulse time profile. The resulting distribution indicates a linear distribution of frequency components across the full time profile of the pulse.

Figure 6.8 shows an example of unprocessed hyperspectral imaging data for a sample composed of adjacent polymethyl methacrylate (PMMA) and polystyrene layers. These materials feature several distinct absorption lines near 2900 cm^{-1} . When the sampled MIR frequency is tuned to 2823 cm^{-1} (2900 fs in time domain), which is off-resonance for both compounds, both layers appear transparent (point b on Fig. 6.8, a and b). Upon rapidly scanning the time delay, the polymers appear darker or brighter, following their absorption spectral profile. Figure 6.8 (c to e) shows several unprocessed frames from the hyperspectral data cube, revealing clear transmission differences between the different materials due to their absorption profiles.

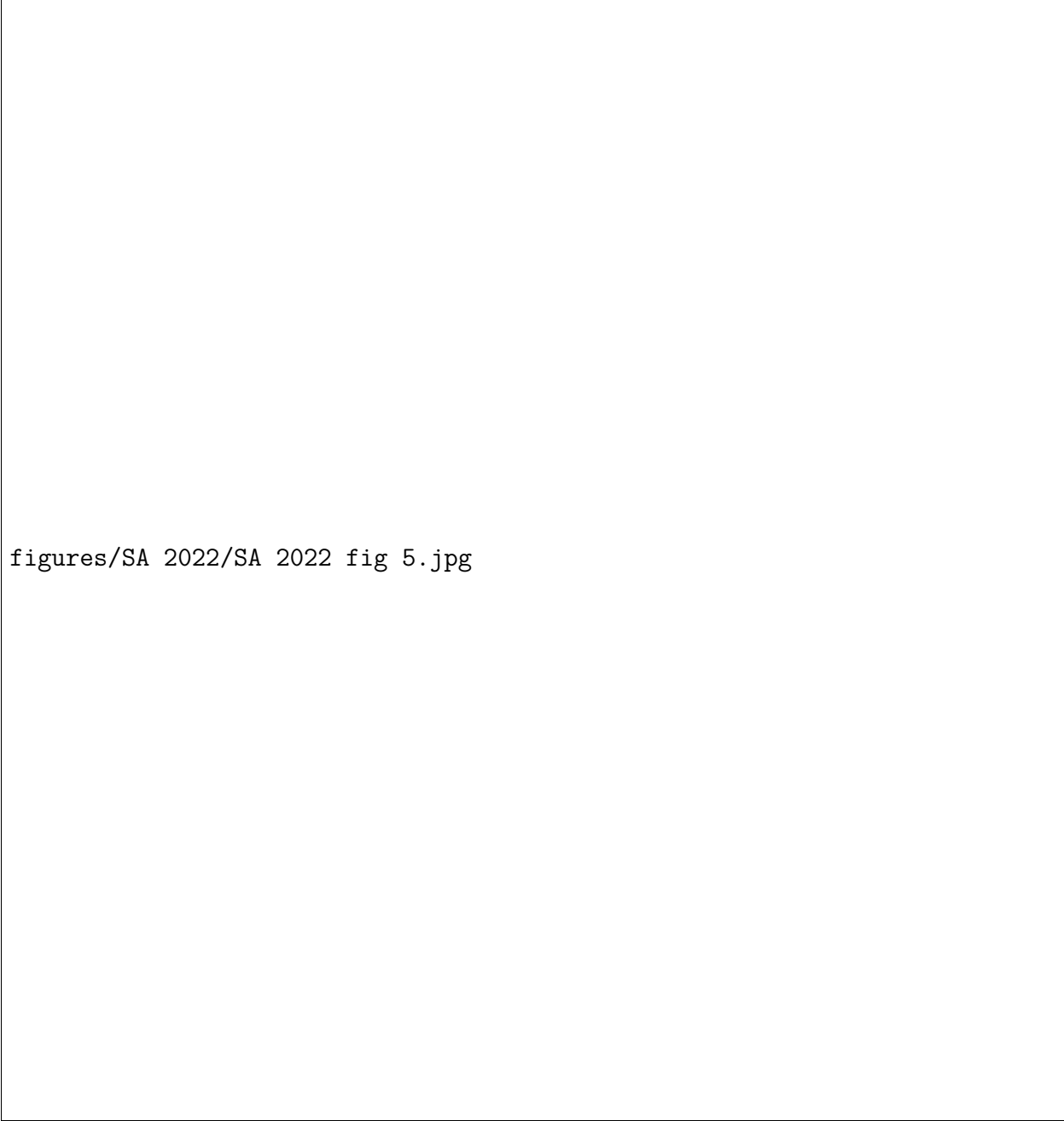


figures/SA 2022/SA 2022 fig 4.jpg

Figure 6.8: unprocessed spectral imaging of polymer samples. (a) Polymer absorption spectrum extracted from the hyperspectral data cube. (b to e) Raw transmission images at different positions in time/spectral domain, directly revealing spatially dependent chemical information in the field of view. Acquisition time is 16 ms per frame/spectral point.

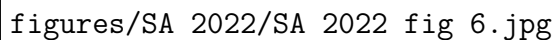
To reduce the dimensionality of the hyperspectral data stack and demonstrate chemical differentiation, we select two images from the data cube where one polymer appears transparent, while another exhibits strong absorption and vice versa (green and red spectral points; Fig. 6.9, a and c). These two frames are represented as the red ($R=100$, $G=0$, and $B=0$) and green ($R=0$, $G=100$, and $B=0$) channels and color-merged to form the single image. The results are shown in Fig. 6.9(b and d), which differentiate the spatial distribution of the two

polymers within the field of view. Similarly, Fig. 6.10 displays reduced dimensionality spectral images of various organic materials and their combinations images through CP-NTA: (a) polystyrene, (b and f) a PMMA/polystyrene structure, (c) ethanol, (d) silicone lubricant (polydimethylsiloxane as main component), and (e) a melted polyethylene flake. The images are composed of two 16-ms frames at two different spectral positions, separated by 72 cm^{-1} in the frequency domain (1 ps separation in time), and represent the on and off resonance positions of a given material. Overlay of the red and green frames then yields an image with chemical contrast.



figures/SA 2022/SA 2022 fig 5.jpg

Figure 6.9: False color visualization of spectral imaging. Spectral imaging of PMMA/polystyrene films. (a and c) Spectra of polystyrene and PMMA components obtained by CP-NTA and FTIR. Red and green lines denote spectral position of color channel image. Dimensionality of the hyperspectral data stack is reduced through overlay of red and green color channels measured on and off the absorption resonance of a given polymer. (b and d) resulting false color spectral image. Effective image acquisition time is 32 ms (16 ms per frame).

The image area is mostly blank, with the text 'figures/SA 2022/SA 2022 fig 6.jpg' centered in the lower-left quadrant. This text likely serves as a placeholder for the spectral images described in the caption.

figures/SA 2022/SA 2022 fig 6.jpg

Figure 6.10: Spectral images of chemical matrices. Spectral imaging of various materials and material combinations: (a) polystyrene, (b and f) PMMA/polystyrene hybrids, (c) ethanol, (d) polyethylene, and (e) silicone lubricant (polydimethylsiloxane). Effective image acquisition time is 32 ms (16 ms per frame).

6.4 Discussion

The technique offered here, CP-NTA, takes advantage of the attractive features of NTA-based MIR detection. Chief among these advantages is the ability to collect MIR images at high definition. Unlike the relatively low pixel density matrix of the fastest focal plane arrays, the > 1 Mpx detector chips used in NTA offer much improved sampling of the projected MIR image. This high-definition imaging capability does not come at the expense of speed, as NTA benefits from the mature readout technology of visible/NIR cameras, permitting MIR imaging at high frame rates. In addition, the NTA technique is interferometry free and does not rely on phase matching of the MIR and gate pulses, enabling a robust and relatively simple optical setup. Furthermore, NTA does not require any image reconstruction

or processing for immediate visualization, allowing direct and on-screen observation of fast processes at particular MIR frequencies.

The key advance in this work is the expansion of NTA-based MIR imaging along the frequency dimension. The CP-NTA method uses the inherent gated detection property of the technique and achieves spectral imaging through time-domain detection by simply adding a dispersive material in the MIR beam. Spectral tuning requires scanning a delay line, which can be performed with ease at high speed, and avoids the need for detuning a light source.

In CP-NTA, each spectral image is acquired in wide-field mode, collecting spectral data at each pixel in a massively parallel fashion. In contrast to laser scanning approaches or wide-field imaging with low-pixel density arrays, which require mosaic stitching to achieve high-definition images, the CP-NTA approach records frames of high pixel number by using 1.3-Mpx camera chips. In this work, we have used a 16-ms image acquisition time for a 500-kilopixel frame and a 700-pixel MIR spot diameter. This camera frame rate (62.5 Hz, 16 ms) has been chosen to eliminate signal fluctuations while allowing full matrix array readout. We note that there is room for considerable improvement of the CP-NTA imaging conditions. First, the current CP-NTA signals have been collected without synchronization of the camera to the 1-kHz radiation source, causing additional noise at frame rates beyond 70 Hz. With appropriate electronic synchronization and a more compact source detection arrangement, the MIR acquisition rate for the used camera can be easily increased to 100 Hz for the full 1280×1024 window. Second, the current experiments result in only 5 fJ per camera pixel at MIR pulse maximum (fig. 6.4). Similar experiments carried out at 100 kHz or higher will significantly improve the detection limits and dynamic range, reaching detection sensitivities of only a few attojoules or tens of photons of MIR radiation on a single camera pixel.

In the spectral domain, the time-frequency sweep can be carried out in a variety of ways. In this work, we have used spectral imaging over the full spectral range of the MIR pulse, but

we have also performed MIR imaging with reduced spectral sampling. For example, the data representation in Fig. 6.9 is based on only two spectral frames with a fixed time-frequency separation. The spectral separation of 72 cm^{-1} between these two images (1 ps in time) can be acquired within a few milliseconds or faster. Rapid modulation of the spectral position can, for instance, be achieved by chopping the gate pulse beam with 0.7-mm glass windows at rates exceeding 100 Hz, producing on and off frames for high-speed chemical imaging.

In the present experiments, we have used a motorized linear stage that allows a fine spectral sweep with scanning speeds up to $12,000\text{ cm}^{-1}/\text{s}$ for the current pulse with precision of 0.72 cm^{-1} ($\sim 170,000\text{ fs/s}$, 10 fs). Other inexpensive approaches exist for rapidly controlling the time-delay setting and performing rapid delay modulation over $\sim 1.5\text{-mm}$ (10-ps) distances. For example, commercially available travel delay stages allow $> 20\text{-Hz}$ delay modulation over an extended 15-ps range with 10-fs time delay precision. Some of the concepts used for the recent development of rapid delay lines in coherent Raman scattering can also be translated for use in CP-NTA [157–159]. We are confident that further development of rapid scanning of the time-frequency axis will render CP-NTA suitable for video-rate hyperspectral data acquisition, in which full $(xy\omega)$ data cubes can be collected in real time.

6.5 Materials and methods

Sample preparation

The polymer samples (polystyrene and PMMA) are placed between two coverslips ($170\text{ }\mu\text{m}$) and melted using a hot plate. During the melting process, the polymer sample is pressed flat by a weight until the desired thickness is reached. The methanol sample is prepared by applying $10\text{ }\mu\text{L}$ of the liquid between two coverslips. The sample is subsequently agitated until bubbles appear. Polyethylene samples are cut and placed between two coverslips.

Vacuum grease samples are prepared by smearing a small amount of the substance onto a coverslip.

FTIR experiments

Conventional infrared absorption spectra are measured using a Jasco 4700 FTIR spectrometer in attenuated total reflection (ATR) geometries. For the ATR experiments, the Jasco ATR Pro One accessory equipped with a diamond crystal is used. The spectra are averaged over 40 scans and are acquired with a resolution of 2 cm^{-1} .

Frequency-domain experiments with pulsed radiation

Frequency-domain experiments for pulse characterization and spectroscopy are performed using a grating-based spectrometer (CM110, Spectral Products, 150 grooves/mm) equipped with single-pixel-amplified MCT detector (PDAVJ10, Thorlabs). All spectra have been measured with 10-nm spectral resolution ($\sim 11\text{ cm}^{-1}$).

CP-NTA detection

A 1-kHz amplified femtosecond laser system (Spitfire Ace, Spectra Physics) is used to seed two optical parametric amplifiers (OPA, TOPAS-Prime, Light Conversion). One OPA is used as a source of NIR gate radiation at 1900 nm (0.65 eV). The signal and idler pulses from the second OPA system are used to generate MIR pulses through the process of difference frequency generation in a nonlinear medium. Both MIR and NIR pulses are recombined on a 1-mm-thick ZnSe window, which serves as dichroic mirror, after which the pulses are overlapped on an InGaAs camera chip (1280MVCam, Princeton Infrared Technologies Inc.). Temporal overlap is controlled through an automated delay stage (GTS150, Newport). The

MIR imaging system consists of two 100 mm CaF₂ lenses, resulting in a 1:1 imaging system with a numerical aperture of 0.015. All experiments are performed with a fixed NIR irradiance of 240 MW/cm² and MIR irradiance 0.25 MW/cm² on the camera chip.

BIBLIOGRAPHY

1. Knez, D., Hanninen, A. M., Prince, R. C., Potma, E. O. & Fishman, D. A. Infrared chemical imaging through non-degenerate two-photon absorption in silicon-based cameras. en. *Light: Science & Applications* **9**, 125. ISSN: 2047-7538. (2020) (Dec. 2020).
2. Potma, E. O. *et al.* High-speed 2D and 3D mid-IR imaging with an InGaAs camera. en. *APL Photonics* **6**, 096108. ISSN: 2378-0967. (2021) (Sept. 2021).
3. Potma, E. O. *et al.* Rapid chemically selective 3D imaging in the mid-infrared. en. *Optica* **8**, 995. ISSN: 2334-2536. (2021) (July 2021).
4. Knez, D. *et al.* Spectral imaging at high definition and high speed in the mid-infrared. en. *Science Advances* **8**, eade4247. ISSN: 2375-2548. (2023) (Nov. 2022).
5. Kröger, N. *et al.* Quantum cascade laser-based hyperspectral imaging of biological tissue. *Journal of Biomedical Optics* **19**, 111607. ISSN: 1083-3668, 1560-2281. (2022) (June 2014).
6. Rosi, F. *et al.* Noninvasive Analysis of Paintings by Mid-infrared Hyperspectral Imaging. *Angewandte Chemie* **52**, 5258–5261 (May 2013).
7. Ruxton, K. *et al.* Mid-infrared hyperspectral imaging for the detection of explosive compounds. *Optics/Photonics in Security and Defence* **8546**, 274–282 (Oct. 2012).

8. Sugawara, S., Nakayama, Y., Taniguchi, H. & Ishimaru, I. Wide-field mid-infrared hyperspectral imaging of adhesives using a bolometer camera. *Scientific Reports* **7**, 12395–12395 (Sept. 2017).
9. Ostendorf, R. *et al.* Recent Advances and Applications of External Cavity-QCLs towards Hyperspectral Imaging for Standoff Detection and Real-Time Spectroscopic Sensing of Chemicals. en. *Photonics* **3**, 28. ISSN: 2304-6732. (2022) (June 2016).
10. Meléndez, J. & Guarnizo, G. Fast Quantification of Air Pollutants by Mid-Infrared Hyperspectral Imaging and Principal Component Analysis. en. *Sensors* **21**, 2092. ISSN: 1424-8220. (2022) (Mar. 2021).
11. Honniball, C. I. *et al.* Mid-Wave Infrared Hyperspectral Imaging of Kilauea’s Halema’uma’u lava lake. **2018** (Dec. 2018).
12. Bhargava, R. Infrared Spectroscopic Imaging: The Next Generation. en. *Applied Spectroscopy* **66**, 1091–1120. ISSN: 0003-7028, 1943-3530. <http://journals.sagepub.com/doi/10.1366/12-06801> (2019) (Oct. 2012).
13. Isensee, K., Kröger-Lui, N. & Petrich, W. Biomedical applications of mid-infrared quantum cascade lasers – a review. en. *The Analyst* **143**, 5888–5911. ISSN: 0003-2654, 1364-5528. (2024) (2018).
14. Yeh, K., Kenkel, S., Liu, J.-N. & Bhargava, R. Fast Infrared Chemical Imaging with a Quantum Cascade Laser. en. *Analytical Chemistry* **87**. ZSCC: 0000110, 485–493. ISSN: 0003-2700, 1520-6882. (2020) (Jan. 2015).
15. Zorin, I., Gattinger, P., Ebner, A. & Brandstetter, M. Advances in mid-infrared spectroscopy enabled by supercontinuum laser sources. en. *Optics Express* **30**, 5222. ISSN: 1094-4087. (2024) (Feb. 2022).
16. Yu, Y. *et al.* 18-10 μm mid-infrared supercontinuum generated in a step-index chalcogenide fiber using low peak pump power. en. *Optics Letters* **40**, 1081. ISSN: 0146-9592, 1539-4794. (2024) (Mar. 2015).

17. Hudson, D. D. *et al.* Toward all-fiber supercontinuum spanning the mid-infrared. en. *Optica* **4**, 1163. ISSN: 2334-2536. (2024) (Oct. 2017).
18. Montesinos-Ballester, M. *et al.* On-Chip Mid-Infrared Supercontinuum Generation from 3 to 13 μ m Wavelength. en. *ACS Photonics* **7**, 3423–3429. ISSN: 2330-4022, 2330-4022. (2024) (Dec. 2020).
19. Granger, G. *et al.* GaAs-chip-based mid-infrared supercontinuum generation. en. *Light: Science & Applications* **12**, 252. ISSN: 2047-7538. (2024) (Oct. 2023).
20. Swiderski, J. High-power mid-infrared supercontinuum sources: Current status and future perspectives. en. *Progress in Quantum Electronics* **38**, 189–235. ISSN: 00796727. (2024) (Sept. 2014).
21. Krebbers, R. *et al.* Mid-infrared supercontinuum-based Fourier transform spectroscopy for plasma analysis. en. *Scientific Reports* **12**, 9642. ISSN: 2045-2322. (2024) (June 2022).
22. Kleinman, D. A. & Boyd, G. D. Infrared Detection by Optical Mixing. en. *Journal of Applied Physics* **40**, 546–566. ISSN: 0021-8979, 1089-7550. (2019) (Feb. 1969).
23. Tidemand-Lichtenberg, P., Dam, J. S., Andersen, H. V., Høgstedt, L. & Pedersen, C. Mid-infrared upconversion spectroscopy. en. *Journal of the Optical Society of America B* **33**, D28. ISSN: 0740-3224, 1520-8540. (2020) (Nov. 2016).
24. Zheng, T. *et al.* High-Speed Mid-Infrared Single-Photon Upconversion Spectrometer. en. *Laser & Photonics Reviews* **17**, 2300149. ISSN: 1863-8880, 1863-8899. (2024) (Sept. 2023).
25. Huang, K., Fang, J., Yan, M., Wu, E. & Zeng, H. Wide-field mid-infrared single-photon upconversion imaging. en. *Nature Communications* **13**. ZSCC: 0000000, 1077. ISSN: 2041-1723. (2022) (Dec. 2022).

26. Fang, J., Huang, K., Wu, E., Yan, M. & Zeng, H. Mid-infrared single-photon 3D imaging. en. *Light: Science & Applications* **12**, 144. ISSN: 2047-7538. (2024) (June 2023).
27. Zhao, Y. *et al.* High-speed scanless entire bandwidth mid-infrared chemical imaging. en. *Nature Communications* **14**, 3929. ISSN: 2041-1723. (2024) (July 2023).
28. Barh, A., Pedersen, C. & Tidemand-Lichtenberg, P. Ultra-broadband mid-wave-IR upconversion detection. en. *Optics Letters* **42**, 1504. ISSN: 0146-9592, 1539-4794. (2024) (Apr. 2017).
29. Junaid, S. *et al.* Video-rate, mid-infrared hyperspectral upconversion imaging. en. *Optica* **6**, 7 (June 2019).
30. Kalashnikov, D. A., Paterova, A. V., Kulik, S. P. & Krivitsky, L. A. Infrared spectroscopy with visible light. en. *Nature Photonics* **10**, 98–101. ISSN: 1749-4885, 1749-4893. (2024) (Feb. 2016).
31. Kaufmann, P., Chrzanowski, H. M., Vanselow, A. & Ramelow, S. Mid-IR spectroscopy with NIR grating spectrometers. en. *Optics Express* **30**, 5926. ISSN: 1094-4087. (2024) (Feb. 2022).
32. Chekhova, M. V. & Ou, Z. Y. Nonlinear interferometers in quantum optics. en. *Advances in Optics and Photonics* **8**, 104. ISSN: 1943-8206. (2024) (Mar. 2016).
33. Barreto Lemos, G., Lahiri, M., Ramelow, S., Lapkiewicz, R. & Plick, W. N. Quantum imaging and metrology with undetected photons: tutorial. en. *Journal of the Optical Society of America B* **39**, 2200. ISSN: 0740-3224, 1520-8540. (2022) (Aug. 2022).
34. Kviatkovsky, I., Chrzanowski, H. M., Avery, E. G., Bartolomaeus, H. & Ramelow, S. Microscopy with undetected photons in the mid-infrared. *arXiv:2002.05960 [physics, physics:quant-ph]*. (2020) (May 2020).

35. Paterova, A. V., Maniam, S. M., Yang, H., Grenzi, G. & Krivitsky, L. A. Hyperspectral infrared microscopy with visible light. en. *Science Advances* **6**, eabd0460. ISSN: 2375-2548. (2024) (Oct. 2020).
36. Paterova, A. V., Toa, Z. S. D., Yang, H. & Krivitsky, L. A. Broadband Quantum Spectroscopy at the Fingerprint Mid-Infrared Region. en. *ACS Photonics* **9**, 2151–2159. ISSN: 2330-4022, 2330-4022. (2024) (June 2022).
37. Lee, E. S. & Lee, J. Y. Nonlinear optical infrared microscopy with chemical specificity. en. *Applied Physics Letters* **94**, 261101. ISSN: 0003-6951, 1077-3118. (2024) (June 2009).
38. Lee, E. S. & Lee, J. Y. High resolution cellular imaging with nonlinear optical infrared microscopy. en. *Optics Express* **19**, 1378. ISSN: 1094-4087. (2024) (Jan. 2011).
39. Adhikari, S. *et al.* Photothermal Microscopy: Imaging the Optical Absorption of Single Nanoparticles and Single Molecules. en. *ACS Nano* **14**, 16414–16445. ISSN: 1936-0851, 1936-086X. (2024) (Dec. 2020).
40. Zhang, D. *et al.* Bond-selective transient phase imaging via sensing of the infrared photothermal effect. en. *Light: Science & Applications* **8**, 116. ISSN: 2047-7538. (2022) (Dec. 2019).
41. Bai, Y., Yin, J. & Cheng, J.-X. Bond-selective imaging by optically sensing the mid-infrared photothermal effect. en. *Science Advances* **7**, eabg1559. ISSN: 2375-2548. (2022) (May 2021).
42. Zhang, Y. *et al.* Vibrational Spectroscopic Detection of a Single Virus by Mid-Infrared Photothermal Microscopy. en. *Analytical Chemistry* **93**, 4100–4107. ISSN: 0003-2700, 1520-6882. (2022) (Mar. 2021).
43. Kniazev, K. *et al.* Hyperspectral and Nanosecond Temporal Resolution Widefield Infrared Photothermal Heterodyne Imaging. en. *ACS Photonics* **10**, 2854–2860. ISSN: 2330-4022, 2330-4022. (2024) (Aug. 2023).

44. Guyot-Sionnest, P., Dumas, P., Chabal, Y. J. & Higashi, G. S. Lifetime of an adsorbate-substrate vibration: H on Si(111). en. *Physical Review Letters* **64**, 2156–2159. ISSN: 0031-9007. (2024) (Apr. 1990).
45. Wang, J. *et al.* Femtosecond Time-Resolved Infrared-Resonant Third-Order Sum-Frequency Spectroscopy. en. *ACS Photonics* **8**, 1137–1142. ISSN: 2330-4022, 2330-4022. (2024) (Apr. 2021).
46. Lambert, A. G., Davies, P. B. & Neivandt, D. J. Implementing the Theory of Sum Frequency Generation Vibrational Spectroscopy: A Tutorial Review. en. *Applied Spectroscopy Reviews* **40**, 103–145. ISSN: 0570-4928, 1520-569X. (2020) (May 2005).
47. Raghunathan, V., Han, Y., Korth, O., Ge, N.-H. & Potma, E. O. Rapid vibrational imaging with sum frequency generation microscopy. en. *Optics Letters* **36**, 3891. ISSN: 0146-9592, 1539-4794. (2024) (Oct. 2011).
48. Shah, S. A. & Baldelli, S. Chemical Imaging of Surfaces with Sum Frequency Generation Vibrational Spectroscopy. en. *Accounts of Chemical Research* **53**, 1139–1150. ISSN: 0001-4842, 1520-4898. (2024) (June 2020).
49. Maekawa, H., Kumar, S. K. K., Mukherjee, S. S. & Ge, N.-H. Phase-Sensitive Vibrationally Resonant Sum-Frequency Generation Microscopy in Multiplex Configuration at 80 MHz Repetition Rate. en. *The Journal of Physical Chemistry B* **125**, 9507–9516. ISSN: 1520-6106, 1520-5207. (2024) (Aug. 2021).
50. Hanninen, A. M., Prince, R. C., Ramos, R., Plikus, M. V. & Potma, E. O. High-resolution infrared imaging of biological samples with third-order sum-frequency generation microscopy. en. *Biomedical Optics Express* **9**, 4807. ISSN: 2156-7085, 2156-7085. (2024) (Oct. 2018).
51. Manattayil, J. K., A. S., L. K., Biswas, R., Kim, H. & Raghunathan, V. Focus-engineered sub-diffraction imaging in infrared-sensitive third-order sum frequency generation microscope. en. *Optics Express* **30**, 25612. ISSN: 1094-4087. (2024) (July 2022).

52. Loudon, R. *The quantum theory of light* 3rd ed. en. ISBN: 978-0-19-850177-0 (Oxford University Press, Oxford ; New York, 2000).
53. Andrews, S. S. Using Rotational Averaging To Calculate the Bulk Response of Isotropic and Anisotropic Samples from Molecular Parameters. en. *Journal of Chemical Education* **81**, 877. ISSN: 0021-9584, 1938-1328. (2024) (June 2004).
54. Yu, P. Y. & Cardona, M. *Fundamentals of Semiconductors* en. ISBN: 978-3-642-00709-5. (2023) (Springer Berlin Heidelberg, Berlin, Heidelberg, 2010).
55. Rosencher, E., Vinter, B., Piva, P. G. & Rosencher, E. *Optoelectronics* eng. ISBN: 978-0-521-77813-8 (Cambridge University Press, Cambridge New York, 2002).
56. Cirloganu, C. M. *et al.* Extremely nondegenerate two-photon absorption in direct-gap semiconductors [Invited]. en. *Optics Express* **19**, 22951. ISSN: 1094-4087. (2019) (Nov. 2011).
57. Kane, E. en. in *Semiconductors and Semimetals* 75–100 (Elsevier, 1966). ISBN: 978-0-12-752101-5. (2022).
58. Lee, C. C. & Fan, H. Y. Two-photon absorption with exciton effect for degenerate valence bands. en. *Physical Review B* **9**, 3502–3516. ISSN: 0556-2805. (2023) (Apr. 1974).
59. Hutchings, D. C. & Van Stryland, E. W. Nondegenerate two-photon absorption in zinc blende semiconductors. en. *Journal of the Optical Society of America B* **9**, 2065. ISSN: 0740-3224, 1520-8540. (2020) (Nov. 1992).
60. Wherrett, B. S. Scaling rules for multiphoton interband absorption in semiconductors. en. *Journal of the Optical Society of America B* **1**, 67. ISSN: 0740-3224, 1520-8540. (2020) (Mar. 1984).
61. Kane, E. Band Structure of Indium Antimonide. *Journal Of Physical Chemistry Solids* **1**, 249–261 (1957).

62. Stryland, E. W. V., Woodall, M. A., Vanherzeele, H. & Soileau, M. J. Energy band-gap dependence of two-photon absorption. EN. *Optics Letters* **10**. Publisher: Optica Publishing Group, 490–492. ISSN: 1539-4794. (2023) (Oct. 1985).
63. Dinu, M. Dispersion of phonon-assisted nonresonant third-order nonlinearities. *IEEE Journal of Quantum Electronics* **39**, 1498–1503. ISSN: 1558-1713 (Nov. 2003).
64. Dinu, M., Quochi, F. & Garcia, H. Third-order nonlinearities in silicon at telecom wavelengths. en. *Applied Physics Letters* **82**, 2954–2956. ISSN: 0003-6951, 1077-3118. (2023) (May 2003).
65. Hayat, A., Ginzburg, P. & Orenstein, M. Infrared single-photon detection by two-photon absorption in silicon. en. *Physical Review B* **77**, 125219. ISSN: 1098-0121, 1550-235X. (2019) (Mar. 2008).
66. Hutchings, D. C. & Wherrett, B. S. Theory of anisotropy of two-photon absorption in zinc-blende semiconductors. en. *Physical Review B* **49**. ZSCC: 0000102, 2418–2426. ISSN: 0163-1829, 1095-3795. <https://link.aps.org/doi/10.1103/PhysRevB.49.2418> (2020) (Jan. 1994).
67. Faryadras, S., Cox, N., Hagan, D. J. & Van Stryland, E. W. *Non-degenerate two-photon absorption spectroscopy of bulk silicon* in *2021 IEEE Research and Applications of Photonics in Defense Conference (RAPID)* (Aug. 2021), 1–2.
68. Zielińska-Raczyńska, S., Czajkowski, G., Karpiński, K. & Ziemkiewicz, D. Nonlinear optical properties and self-Kerr effect of Rydberg excitons. en. *Physical Review B* **99**, 245206. ISSN: 2469-9950, 2469-9969. (2024) (June 2019).
69. Morin, C. *et al.* Self-Kerr Effect across the Yellow Rydberg Series of Excitons in $\{\mathrm{Cu}\}_2\mathrm{O}$. *Physical Review Letters* **129**, 137401. (2023) (Sept. 2022).
70. Green, M. A. Improved value for the silicon free exciton binding energy. en. *AIP Advances* **3**, 112104. ISSN: 2158-3226. (2024) (Nov. 2013).

71. Valentin, A., Sée, J., Galdin-Retailleau, S. & Dollfus, P. Study of phonon modes in silicon nanocrystals using the adiabatic bond charge model. *Journal of Physics: Condensed Matter* **20**, 145213. ISSN: 0953-8984, 1361-648X. (2024) (Apr. 2008).
72. Kim, D. S. *et al.* Phonon anharmonicity in silicon from 100 to 1500 K. en. *Physical Review B* **91**, 014307. ISSN: 1098-0121, 1550-235X. (2024) (Jan. 2015).
73. Bassani, G. F. & Pastori Parravicini, G. *Electronic states and optical transitions in solids* 1st ed. ISBN: 978-0-08-016846-3 (Pergamon Press, Oxford, New York, 1975).
74. Negres, R. A., Hales, J. M., Kobayakov, A., Hagan, D. J. & Stryland, E. W. V. Experiment and analysis of two-photon absorption spectroscopy using a white-light continuum probe. *IEEE Journal of Quantum Electronics* **38**, 1205–1216. ISSN: 1558-1713 (Sept. 2002).
75. Schinke, C. *et al.* Uncertainty analysis for the coefficient of band-to-band absorption of crystalline silicon. en. *AIP Advances* **5**, 067168. ISSN: 2158-3226. (2024) (June 2015).
76. Shkondin, E. *et al.* Large-scale high aspect ratio Al-doped ZnO nanopillars arrays as anisotropic metamaterials. en. *Optical Materials Express* **7**, 1606. ISSN: 2159-3930. (2024) (May 2017).
77. Bristow, A. D., Rotenberg, N. & van Driel, H. M. Two-photon absorption and Kerr coefficients of silicon for 850–2200nm. en. *Applied Physics Letters* **90**, 191104. ISSN: 0003-6951, 1077-3118. (2020) (May 2007).
78. Garcia, H. & Kalyanaraman, R. Phonon-assisted two-photon absorption in the presence of a dc-field: the nonlinear Franz–Keldysh effect in indirect gap semiconductors. *Journal of Physics B: Atomic, Molecular and Optical Physics* **39**, 2737–2746. ISSN: 0953-4075, 1361-6455. (2024) (June 2006).
79. Strehlow, W. H. & Cook, E. L. Compilation of Energy Band Gaps in Elemental and Binary Compound Semiconductors and Insulators. en. *Journal of Physical and Chemical Reference Data* **2**, 163–200. ISSN: 0047-2689, 1529-7845. (2024) (Jan. 1973).

80. Czajkowski, G., Bassani, F. & Tredicucci, A. Polaritonic effects in superlattices. en. *Physical Review B* **54**, 2035–2043. ISSN: 0163-1829, 1095-3795. (2024) (July 1996).
81. Singh, J. *Physics of semiconductors and their heterostructures* ISBN: 978-0-07-057607-0 (McGraw-Hill, New York, 1993).
82. Fishman, D. A. *et al.* Sensitive mid-infrared detection in wide-bandgap semiconductors using extreme non-degenerate two-photon absorption. *Nature Photonics* **5**, 561–565. ISSN: 17494885 (2011).
83. Tauc, J. Optical properties and electronic structure of amorphous Ge and Si. en. *Materials Research Bulletin* **3**, 37–46. ISSN: 00255408. (2024) (Jan. 1968).
84. *Handbook of optical constants of solids II* (ed Palik, E. D.) ISBN: 978-0-12-544422-4 (Academic Press, Boston, 1991).
85. Wallace, V. M., Dhumal, N. R., Zehentbauer, F. M., Kim, H. J. & Kiefer, J. Revisiting the Aqueous Solutions of Dimethyl Sulfoxide by Spectroscopy in the Mid- and Near-Infrared: Experiments and Car–Parrinello Simulations. en. *The Journal of Physical Chemistry B* **119**, 14780–14789. ISSN: 1520-6106, 1520-5207. (2024) (Nov. 2015).
86. Cirloganu, C. *Experimental And Theoretical Approaches To Characterization Of Electronic Nonlinearities In Direct-gap Semiconductors* PhD thesis (University of Central Florida, 2010).
87. Van Stryland, E. W., Wu, Y. Y., Hagan, D. J., Soileau, M. J. & Mansour, K. Optical limiting with semiconductors. en. *Journal of the Optical Society of America B* **5**, 1980. ISSN: 0740-3224, 1520-8540. (2024) (Sept. 1988).
88. Boyne, J. A. & Williamson, A. G. Enthalpies of mixture of ethanol and water at 25.degree.C. en. *Journal of Chemical & Engineering Data* **12**, 318–318. ISSN: 0021-9568, 1520-5134. (2024) (July 1967).

89. Peeters, D. & Huyskens, P. Endothermicity or exothermicity of water/alcohol mixtures. en. *Journal of Molecular Structure* **300**, 539–550. ISSN: 00222860. (2024) (Dec. 1993).
90. Junaid, S. *et al.* Mid-infrared upconversion based hyperspectral imaging. en. *Optics Express* **26**, 2203. ISSN: 1094-4087. (2020) (Feb. 2018).
91. Millare, J. C. & Basilia, B. A. Nanobubbles from Ethanol-Water Mixtures: Generation and Solute Effects via Solvent Replacement Method. en. *ChemistrySelect* **3**, 9268–9275. ISSN: 2365-6549, 2365-6549. (2024) (Aug. 2018).
92. Cox, N., Hagan, D. J. & Stryland, E. W. V. *Extremely nondegenerate two-photon absorption in silicon (Conference Presentation)* in *Ultrafast Phenomena and Nanophotonics XXIII* **10916** (International Society for Optics and Photonics, Mar. 2019), 1091613. (2020).
93. Hanninen, A. M. & Potma, E. O. Nonlinear optical microscopy with achromatic lenses extending from the visible to the mid-infrared. en. *APL Photonics* **4**, 080801. ISSN: 2378-0967. (2024) (Aug. 2019).
94. Cheung, C. S., Daniel, J. M. O., Tokurakawa, M., Clarkson, W. A. & Liang, H. High resolution Fourier domain optical coherence tomography in the 2 μ m wavelength range using a broadband supercontinuum source. en. *Optics Express* **23**, 1992. ISSN: 1094-4087. (2023) (Feb. 2015).
95. Colley, C. S. *et al.* Mid-infrared optical coherence tomography. en. *Review of Scientific Instruments* **78**, 123108. ISSN: 0034-6748, 1089-7623. (2023) (Dec. 2007).
96. Guilhaumou, N., Dumas, P., Carr, G. L. & Williams, G. P. Synchrotron Infrared Microspectrometry Applied to Petrography in Micrometer-Scale Range: Fluid Chemical Analysis and Mapping. en. *Applied Spectroscopy* **52**, 1029–1034. ISSN: 0003-7028, 1943-3530. (2023) (Aug. 1998).

97. Ishida, S. & Nishizawa, N. Quantitative comparison of contrast and imaging depth of ultrahigh-resolution optical coherence tomography images in 800–1700 nm wavelength region. en. *Biomedical Optics Express* **3**, 282. ISSN: 2156-7085, 2156-7085. (2023) (Feb. 2012).
98. Jamme, F., Lagarde, B., Giuliani, A., Garcia, G. A. & Mercury, L. Synchrotron infrared confocal microscope: Application to infrared 3D spectral imaging. *Journal of Physics: Conference Series* **425**, 142002. ISSN: 1742-6588, 1742-6596. (2023) (Mar. 2013).
99. Martin, M. C. *et al.* 3D spectral imaging with synchrotron Fourier transform infrared spectro-microtomography. en. *Nature Methods* **10**, 861–864. ISSN: 1548-7091, 1548-7105. (2023) (Sept. 2013).
100. Sharma, U., Chang, E. W. & Yun, S. H. Long-wavelength optical coherence tomography at 17 μm for enhanced imaging depth. en. *Optics Express* **16**, 19712. ISSN: 1094-4087. (2023) (Nov. 2008).
101. Zorin, I. *et al.* Mid-infrared Fourier-domain optical coherence tomography with a pyroelectric linear array. EN. *Optics Express* **26**, 33428–33439. ISSN: 1094-4087. (2021) (Dec. 2018).
102. Zorin, I., Gattinger, P., Brandstetter, M. & Heise, B. Dual-band infrared optical coherence tomography using a single supercontinuum source. en. *Optics Express* **28**, 7858. ISSN: 1094-4087. (2023) (Mar. 2020).
103. Israelsen, N. M. *et al.* Real-time high-resolution mid-infrared optical coherence tomography. en. *Light: Science & Applications* **8**, 11. ISSN: 2047-7538. (2020) (Jan. 2019).
104. Paterova, A. V., Yang, H., An, C., Kalashnikov, D. A. & Krivitsky, L. A. Tunable optical coherence tomography in the infrared range using visible photons. *Quantum Science and Technology* **3**, 025008. ISSN: 2058-9565. (2023) (Apr. 2018).

105. Vallés, A., Jiménez, G., Salazar-Serrano, L. J. & Torres, J. P. Optical sectioning in induced coherence tomography with frequency-entangled photons. en. *Physical Review A* **97**, 023824. ISSN: 2469-9926, 2469-9934. (2023) (Feb. 2018).
106. Vanselow, A. *et al.* Frequency-domain optical coherence tomography with undetected mid-infrared photons. en. *Optica* **7**, 1729. ISSN: 2334-2536. (2023) (Dec. 2020).
107. Rojas-Santana, A., Machado, G. J., Lopez-Mago, D. & Torres, J. P. Frequency-correlation requirements on the biphoton wave function in an induced-coherence experiment between separate sources. en. *Physical Review A* **102**, 053711. ISSN: 2469-9926, 2469-9934. (2023) (Nov. 2020).
108. Machado, G. J., Frascella, G., Torres, J. P. & Chekhova, M. V. Optical coherence tomography with a nonlinear interferometer in the high parametric gain regime. en. *Applied Physics Letters* **117**, 094002. ISSN: 0003-6951, 1077-3118. (2023) (Aug. 2020).
109. Pattanaik, H. S., Reichert, M., Hagan, D. J. & Van Stryland, E. W. Three-dimensional IR imaging with uncooled GaN photodiodes using nondegenerate two-photon absorption. en. *Optics Express* **24**, 1196. ISSN: 1094-4087. (2023) (Jan. 2016).
110. Li, L. *Time-of-Flight Camera – An Introduction* tech. rep. (Texas Instruments, May 2014). (2024).
111. Hussein, H. M., Terra, O., Hussein, H. & Medhat, M. Collinear versus non-collinear autocorrelation between femtosecond pulses for absolute distance measurement. en. *Measurement* **152**, 107319. ISSN: 02632241. (2024) (Feb. 2020).
112. Li, Z. & Ram, R. J. Nanosecond pulsed CMOS LED for all-silicon time-of-flight ranging. en. *Optics Express* **31**, 24307. ISSN: 1094-4087. (2024) (July 2023).
113. Coddington, I., Swann, W. C., Nenadovic, L. & Newbury, N. R. Rapid and precise absolute distance measurements at long range. en. *Nature Photonics* **3**, 351–356. ISSN: 1749-4885, 1749-4893. (2024) (June 2009).

114. Suh, M.-G. & Vahala, K. J. Soliton microcomb range measurement. en. *Science* **359**, 884–887. ISSN: 0036-8075, 1095-9203. (2024) (Feb. 2018).
115. Lee, J., Kim, Y.-J., Lee, K., Lee, S. & Kim, S.-W. Time-of-flight measurement with femtosecond light pulses. en. *Nature Photonics* **4**, 716–720. ISSN: 1749-4885, 1749-4893. (2024) (Oct. 2010).
116. Na, Y. *et al.* Ultrafast, sub-nanometre-precision and multifunctional time-of-flight detection. en. *Nature Photonics* **14**, 355–360. ISSN: 1749-4885, 1749-4893. (2024) (June 2020).
117. Yamakoshi, H. *et al.* Imaging of EdU, an Alkyne-Tagged Cell Proliferation Probe, by Raman Microscopy. en. *Journal of the American Chemical Society* **133**, 6102–6105. ISSN: 0002-7863, 1520-5126. (2024) (Apr. 2011).
118. Li, Y., Townsend, K. M., Dorn, R. S., Prescher, J. A. & Potma, E. O. Enhancing Alkyne-Based Raman Tags with a Sulfur Linker. en. *The Journal of Physical Chemistry B* **127**, 1976–1982. ISSN: 1520-6106, 1520-5207. (2024) (Mar. 2023).
119. Peelen, J. G. J. & Metselaar, R. Light scattering by pores in polycrystalline materials: Transmission properties of alumina. en. *Journal of Applied Physics* **45**, 216–220. ISSN: 0021-8979, 1089-7550. (2023) (Jan. 1974).
120. Su, R. *et al.* Perspectives of mid-infrared optical coherence tomography for inspection and micrometrology of industrial ceramics. EN. *Optics Express* **22**, 15804–15819. ISSN: 1094-4087. (2020) (June 2014).
121. Born, M., Wolf, E. & Bhatia, A. B. *Principles of optics: electromagnetic theory of propagation, interference, and diffraction of light* Seventh (expanded) anniversary edition, 60th anniversary edition. ISBN: 978-1-108-47743-7 (Cambridge University Press, Cambridge, 2019).
122. Morgner, U. *et al.* Spectroscopic optical coherence tomography. en. *Optics Letters* **25**, 111. ISSN: 0146-9592, 1539-4794. (2024) (Jan. 2000).

123. Xu, C., Carney, P. S. & Boppart, S. A. Wavelength-dependent scattering in spectroscopic optical coherence tomography. en. *Optics Express* **13**, 5450. ISSN: 1094-4087. (2024) (2005).
124. Bosschaart, N., Van Leeuwen, T. G., Aalders, M. C. G. & Faber, D. J. Quantitative comparison of analysis methods for spectroscopic optical coherence tomography. en. *Biomedical Optics Express* **4**, 2570. ISSN: 2156-7085, 2156-7085. (2024) (Nov. 2013).
125. Nam, H. S. & Yoo, H. Spectroscopic optical coherence tomography: A review of concepts and biomedical applications. en. *Applied Spectroscopy Reviews* **53**, 91–111. ISSN: 0570-4928, 1520-569X. (2024) (Apr. 2018).
126. Guo, B. *et al.* Laser-based mid-infrared reflectance imaging of biological tissues. en. *Optics Express* **12**, 208. ISSN: 1094-4087. (2024) (2004).
127. Davis, B. J., Carney, P. S. & Bhargava, R. Theory of Midinfrared Absorption Microspectroscopy: I. Homogeneous Samples. en. *Analytical Chemistry* **82**, 3474–3486. ISSN: 0003-2700, 1520-6882. (2024) (May 2010).
128. Dluhy, R. A. Quantitative external reflection infrared spectroscopic analysis of insoluble monolayers spread at the air-water interface. en. *The Journal of Physical Chemistry* **90**, 1373–1379. ISSN: 0022-3654, 1541-5740. (2023) (Mar. 1986).
129. Yamamoto, K. & Ishida, H. Interpretation of Reflection and Transmission Spectra for Thin Films: Reflection. en. *Applied Spectroscopy* **48**, 775–787. ISSN: 0003-7028, 1943-3530. (2024) (July 1994).
130. Yamamoto, K. & Ishida, H. Kramers-Kronig analysis applied to reflection-absorption spectroscopy. en. *Vibrational Spectroscopy* **15**, 27–36. ISSN: 09242031. (2024) (Aug. 1997).
131. Blaudez, D., Castano, S. & Desbat, B. en. in *Biointerface Characterization by Advanced IR Spectroscopy* 27–55 (Elsevier, 2011). ISBN: 978-0-444-53558-0. (2024).

132. Zangwill, A. *Modern Electrodynamics*: 1st ed. en. ISBN: 978-1-139-03477-7. (2021) (Cambridge University Press, Dec. 2012).
133. Drexler, W. *et al.* Optical coherence tomography today: speed, contrast, and multi-modality. en. *Journal of Biomedical Optics* **19**, 071412. ISSN: 1083-3668. (2020) (July 2014).
134. Agrawal, A., Pfefer, T. J., Woolliams, P. D., Tomlins, P. H. & Nehmetallah, G. Methods to assess sensitivity of optical coherence tomography systems. en. *Biomedical Optics Express* **8**, 902. ISSN: 2156-7085, 2156-7085. (2024) (Feb. 2017).
135. Klein, T. & Huber, R. High-speed OCT light sources and systems [Invited]. en. *Biomedical Optics Express* **8**, 828. ISSN: 2156-7085, 2156-7085. (2024) (Feb. 2017).
136. Choma, M., Sarunic, M., Yang, C. & Izatt, J. Sensitivity advantage of swept source and Fourier domain optical coherence tomography. en. *Optics Express* **11**, 2183. ISSN: 1094-4087. (2024) (Sept. 2003).
137. Kise, D. P., Magana, D., Reddish, M. J. & Dyer, R. B. Submillisecond mixing in a continuous-flow, microfluidic mixer utilizing mid-infrared hyperspectral imaging detection. en. *Lab Chip* **14**, 584–591. ISSN: 1473-0197, 1473-0189. (2024) (2014).
138. Haase, K., Kröger-Lui, N., Pucci, A., Schönhals, A. & Petrich, W. Real-time mid-infrared imaging of living microorganisms. en. *Journal of Biophotonics* **9**, 61–66. ISSN: 1864-063X, 1864-0648. (2024) (Jan. 2016).
139. Pereira, J. F. Q. *et al.* Projection pursuit and PCA associated with near and middle infrared hyperspectral images to investigate forensic cases of fraudulent documents. en. *Microchemical Journal* **130**, 412–419. ISSN: 0026265X. (2024) (Jan. 2017).
140. Kontsek, E. *et al.* Mid-Infrared Imaging Is Able to Characterize and Separate Cancer Cell Lines. en. *Pathology & Oncology Research* **26**, 2401–2407. ISSN: 1219-4956, 1532-2807. (2024) (Oct. 2020).

141. Yeh, K. *et al.* Infrared spectroscopic laser scanning confocal microscopy for whole-slide chemical imaging. en. *Nature Communications* **14**, 5215. ISSN: 2041-1723. (2024) (Aug. 2023).
142. Potma, E. O. *Foundations of Nonlinear Optical Microscopy* 1st ed. ISBN: 978-1-119-81488-7 (John Wiley & Sons, 2024).
143. Martinez, O. 3000 times grating compressor with positive group velocity dispersion: Application to fiber compensation in 1.3-1.6 μm region. en. *IEEE Journal of Quantum Electronics* **23**, 59–64. ISSN: 0018-9197. (2024) (Jan. 1987).
144. Ivanov, V. Compact optical grating compressor. en. *Optics Express* **30**, 35338. ISSN: 1094-4087. (2024) (Sept. 2022).
145. Grüner-Nielsen, L., Jakobsen, D., Jespersen, K. G. & Pálsdóttir, B. A stretcher fiber for use in fs chirped pulse Yb amplifiers. en. *Optics Express* **18**, 3768. ISSN: 1094-4087. (2024) (Feb. 2010).
146. Sivabalan, S. & Raina, J. P. High Normal Dispersion and Large Mode Area Photonic Quasi-Crystal Fiber Stretcher. *IEEE Photonics Technology Letters* **23**, 1139–1141. ISSN: 1041-1135, 1941-0174. (2024) (Aug. 2011).
147. Cheriaux, G. *et al.* Aberration-free stretcher design for ultrashort-pulse amplification. en. *Optics Letters* **21**, 414. ISSN: 0146-9592, 1539-4794. (2024) (Mar. 1996).
148. Cialdi, S., Vicario, C., Petrarca, M. & Musumeci, P. Simple scheme for ultraviolet time-pulse shaping. en. *Applied Optics* **46**, 4959. ISSN: 0003-6935, 1539-4522. (2024) (Aug. 2007).
149. Weiner, A. M. Femtosecond pulse shaping using spatial light modulators. en. *Review of Scientific Instruments* **71**, 1929–1960. ISSN: 0034-6748, 1089-7623. (2024) (May 2000).
150. Weiner, A. M. *Ultrafast optics* ISBN: 978-0-471-41539-8 (Wiley, Hoboken, N.J, 2009).

151. Chandler-Horowitz, D. & Amirtharaj, P. M. High-accuracy, midinfrared (450cm⁻¹–4000cm⁻¹) refractive index values of silicon. en. *Journal of Applied Physics* **97**, 123526. ISSN: 0021-8979, 1089-7550. (2024) (June 2005).
152. Nibbering, E. T. J., Wiersma, D. A. & Duppen, K. Ultrafast nonlinear spectroscopy with chirped optical pulses. en. *Physical Review Letters* **68**, 514–517. ISSN: 0031-9007. (2024) (Jan. 1992).
153. Hellerer, T., Enejder, A. M. & Zumbusch, A. Spectral focusing: High spectral resolution spectroscopy with broad-bandwidth laser pulses. en. *Applied Physics Letters* **85**, 25–27. ISSN: 0003-6951, 1077-3118. (2024) (July 2004).
154. Mohseni, M., Polzer, C. & Hellerer, T. Resolution of spectral focusing in coherent Raman imaging. en. *Optics Express* **26**, 10230. ISSN: 1094-4087. (2024) (Apr. 2018).
155. Kubarych, K. J., Joffre, M., Moore, A., Belabas, N. & Jonas, D. M. Mid-infrared electric field characterization using a visible charge-coupled-device-based spectrometer. en. *Optics Letters* **30**, 1228. ISSN: 0146-9592, 1539-4794. (2024) (May 2005).
156. Zhu, J., Mathes, T., Stahl, A. D., Kennis, J. T. & Groot, M. L. Ultrafast mid-infrared spectroscopy by chirped pulse upconversion in 1800-1000cm⁻¹ region. en. *Optics Express* **20**, 10562. ISSN: 1094-4087. (2024) (May 2012).
157. Liao, C.-S. *et al.* Stimulated Raman spectroscopic imaging by microsecond delay-line tuning. en. *Optica* **3**, 1377. ISSN: 2334-2536. (2024) (Dec. 2016).
158. Alshaykh, M. S. *et al.* High-speed stimulated hyperspectral Raman imaging using rapid acousto-optic delay lines. en. *Optics Letters* **42**, 1548. ISSN: 0146-9592, 1539-4794. (2024) (Apr. 2017).
159. He, R. *et al.* Stimulated Raman scattering microscopy and spectroscopy with a rapid scanning optical delay line. en. *Optics Letters* **42**, 659. ISSN: 0146-9592, 1539-4794. (2024) (Feb. 2017).